Study of inclusive breakup reactions induced by weakly bound nuclei

a dissertation presented
by
Jin Lei
to
The Department of Physics

in partial fulfillment of the requirements
for the degree of
Doctor of Science
in the subject of
Nuclear Physics

Universidad de Sevilla
Sevilla, Spain
July 2016

Thesis advisor: Professor Antonio M. Moro Jin Lei

Study of inclusive breakup reactions induced by weakly bound nuclei

Abstract

An important mechanism that takes place in the nuclear collisions is the dissociation of the projectile into two or more fragments. In many experiments, with both stable and radioactive nuclei, only one of the fragments is detected giving rise to the so-called inclusive breakup. For the two-body dissociation, this corresponds to reactions of the form $a(b+x)+A \rightarrow b+$ anything. The theoretical interpretation of these reactions is complicated due to the fact that many processes (compound nucleus, transfer, direct breakup ...) can contribute to the production of the b fragment. The inclusive breakup is usually separated into two contributions, namely, the elastic breakup (EBU) and the nonelastic breakup (NEB). The former corresponds to processes in which the fragment b and x survive after the collisions and the target remains in its ground state. By contrast, nonelastic breakup corresponds to those breakup processes accompanied by the absorption of the unobserved fragment or by target excitation.

The problem was addressed in the 1980s by several groups, who proposed closed-form formulae for the calculation of these observables. In this dissertation, we revisit the theory proposed by these groups, in particular, the theory of Ichimura, Austern, and Vincent (IAV) [Phys. Rev. C 32, 431 (1985)] and show applications to several reactions induced by weakly-bound projectiles, such as deuterons, ^{6,7}Li, ^{7}Be, ^{8}B and ^{11}Be, comparing with available data.

In addition, we study the dependence of the EBU and NEB contributions with the incident energy and the separation energy of the projectile. We also investigate the reaction modes and reaction cross section of the ^{6}Li + ^{209}Bi reaction.

We address the problem of the post-prior equivalence in inclusive breakup reactions. The problem is studied within the distorted-wave Born approximation (DWBA) version of IAV model. The post and prior formulas obtained in this model are briefly recalled and applied to several breakup reactions induced by deuterons and ^{6}Li projectiles, to test their actual numerical equivalence. The different contributions of the prior-form formula are also discussed. A critical comparison with the prior-form DWBA model of Udagawa and Tamura [Phys. Rev. C 24, 1348 (1981)] is also provided.

We also discuss the possibility of applying the IAV theory to the evaluation of incomplete fusion (ICF). For that, we propose a simple model and apply it to the ^{6}Li+^{209}Bi reaction. We also investigate the application of this model to the study of surrogate reactions, and illustrate it for the ^{238}U(d,pf) reaction, comparing with recently measured data.

Contents

Listing of figures

This thesis is dedicated to my parents and my wife.
For their endless love, support and encouragement.

Acknowledgments

First and foremost, I have to thank my parents for their love and support throughout my life. Thank you both for giving me strength to reach for the stars and chase my dreams.

This thesis could not be written to its fullest without Prof. A. M. Moro, who served as my supervisor, as well as one who challenged and encouraged me throughout my time spent studying under him. His guidance helped me in all the time of research and writing of this thesis. I could not have imagined having a better advisor and mentor for my Ph.D study.

I would like to thank Prof. B.V. Carlson, for his valuable and insightful comments and suggestions during my stay in São José dos Campos, Brazil.

I must also acknowledge Prof. B. Jurado and Dr. Q. Ducasse for their collaboration on surrogate reactions and for allowing me to use their unpublished data for ^{238}U(d,pf) reaction.

I would also like to thank Prof. A. Di Pietro for useful discussions on the ^{11}Be+^{64}Zn reaction and permitting me to use unpublished results for this reaction.

I am grateful for the help of Prof. I.J. Thompson and Dr. G. Potel for their feedback on the formal aspects of the inclusive breakup models.

I would also like to thank and acknowledge M. Gómez-Ramos for our exchanges of knowledge, skills, and venting of frustration during my graduate program, which helped enrich the experience.

To all my friends, thank you for your understanding and encouragement in my many, many moments of crisis. Your friendship makes my life a wonderful experience. I cannot list all the names here, but you are always on my mind.

Thank you, Ofelia Liu, for always being there for me.

In the beginning there was nothing, which exploded.

Terry Pratchett

1 Introduction

1.1 Background

The breakup of a nucleus into two or more fragments is an important mechanism occurring in nuclear collisions, particularly when one of the colliding nuclei is weakly bound. The analysis of this kind of processes has provided useful information on the structure of the broken nucleus, such as binding energies, spectroscopic factors and angular momentum (e.g. [103,104]), and has contributed to the understanding of the dynamics of the reactions among composite systems.

In the simplest scenario, in which the projectile is broken up into two fragments, these processes can be schematically represented as $a+A \rightarrow b+x+A$, where $a = b+x$. From the theoretical point of view, this problem is difficult to treat because one has to deal with three-body final states. When the state of the three outgoing fragments (b, x and A) is fully determined, the reaction is said to be *exclusive*. If, in addition, the three particles are emitted in their ground state, the corresponding cross section is referred to as *elastic breakup* (EBU). In this case, the reaction can be treated as an effective three-body problem interacting via some effective two-body interactions. Although the rigorous formal solution of this problem is given by the Faddeev formalism[48,53], the difficulty of solving these equations has led to the development of sim-

pler approaches, such as the distorted-wave Born approximation (DWBA)[10], the continuum-discretized coupled-channels (CDCC) method[4] and a variety of semiclassical approaches[132,45,85,25].

A more complicated situation occurs when the final state of one or more fragments is not specified. In this case, the reaction is said to be *inclusive* with respect to this unobserved particle(s). This is the case of reactions of the form $a + A \to b + B^*$, where B^* is any possible configuration of the $x + A$ system. The inclusive cross section for the detection of b particles will be therefore the sum of the cross sections for all processes leading to "b" particles. In general, the main contributions will be the following:

(i) The elastic breakup process (EBU), in which the three outgoing particles are emitted in their ground state, i.e., $a + A \to b + x + A_{\rm gs}$.

(ii) Inelastic breakup (INBU), in which the breakup is accompanied by the excitation of some of the fragments. For example, if the target is excited, $a + A \to b + x + A^*$, whereas if the core particle is excited, $a + A \to b^* + x + A_{\rm gs}$.

(iii) Particle transfer, leading to bound states of the $A + x$ system, i.e. $a + A \to b + B$ ($B \equiv A + x$).

(iv) Incomplete fusion (ICF), in which the fragment x is absorbed by the target, forming a compound nucleus C, which will eventually decay by particle or gamma-ray emission: $a + A \to b + C$.

(v) Complete fusion (CF) followed by evaporation. If b is among the evaporation products, it will contribute also to the inclusive b yield. We include also in this category the preequilibrium (PE) processes.

In Fig. 1.1 these processes are schematically depicted for a $d + A$ reaction.

The EBU cross sections [process (i)], can be accurately obtained with the three-body models cited above, either quantum-mechanical (DWBA, CDCC, AGS/Faddeev) or semiclassical.

The calculation of INBU, process (ii), has been less explored in the literature. In the case of target excitation, this was done by the Kyushu group in the early days of the CDCC method[143] for the case of deuteron scattering, with the aim of comparing the relative importance and mutual influence of target-excitation and deuteron breakup in elastic and inelastic scattering of deuterons. Since then, this problem has receive little attention in the literature. In addition, if b is a composite nucleus, it can be excited too. This problem has been recently addressed by several groups using an extended version of the CDCC method[126,33].

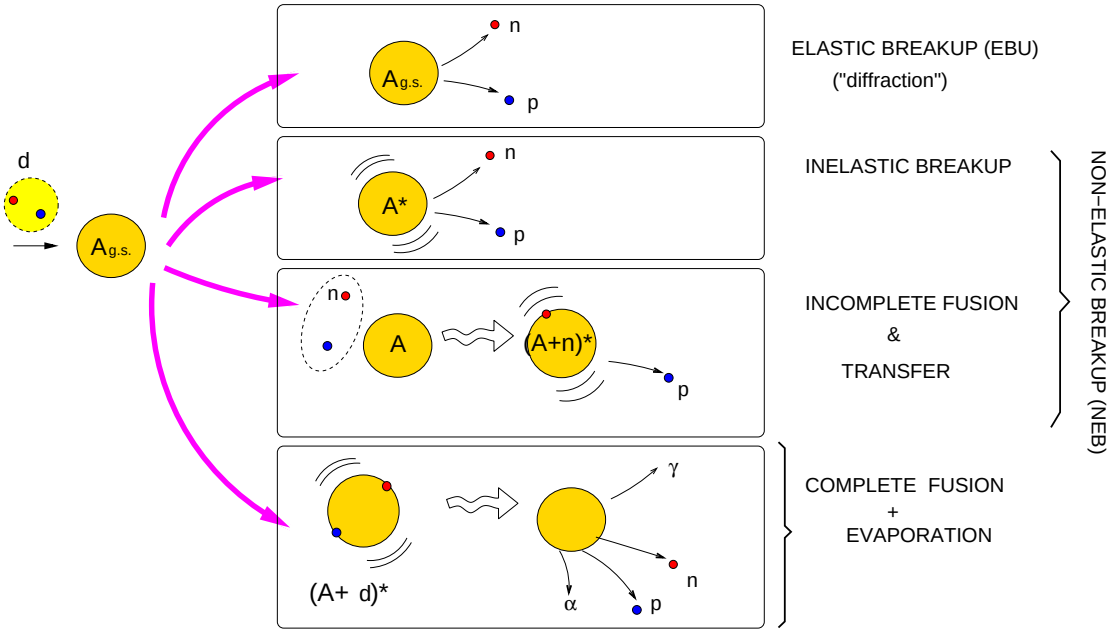

Figure 1.1: Reaction modes for the $d + A$ reaction.

Process (iii), i.e., transfer of x to bound states of A, has been traditionally treated within the DWBA method [119]. For weakly-bound projectiles, the coupling to the breakup channels becomes important, and this effect is known to affect the transfer cross sections. This effect can be incorporated using the adiabatic distorted wave approximation (ADWA) of Johnson and Soper [77] and more elaborate versions of it (e.g., Ref. [76]). A recent review of these theories can be found in Ref. [20].

The process (iv), ICF, is very challenging from the theoretical point of view to the extent that, at present, no fully-quantum mechanical theory exists to calculate ICF cross sections. For this reason, alternative methods, based on semiclassical ideas, have been proposed in the literature [96,39,37]. Moreover, from the experimental point of view, the identification of this process is not without its difficulties since, many times, the products coincide with those produced in the transfer reactions.

Processes (ii)-(iv) will be henceforth referred to as non-elastic breakup (NEB). The theoretical evaluation of NEB cross sections is the main topic of this work.

Process (v) is qualitatively different from the previous ones, because it takes place via the formation of a compound nucleus, rather than via a direct process. The calculation of detailed cross sections, as a function of the angle/energy of the outgoing particles, requires the use of statistical models, first proposed by Bohr [12], and whose modern formulation can be found in many textbooks [129].

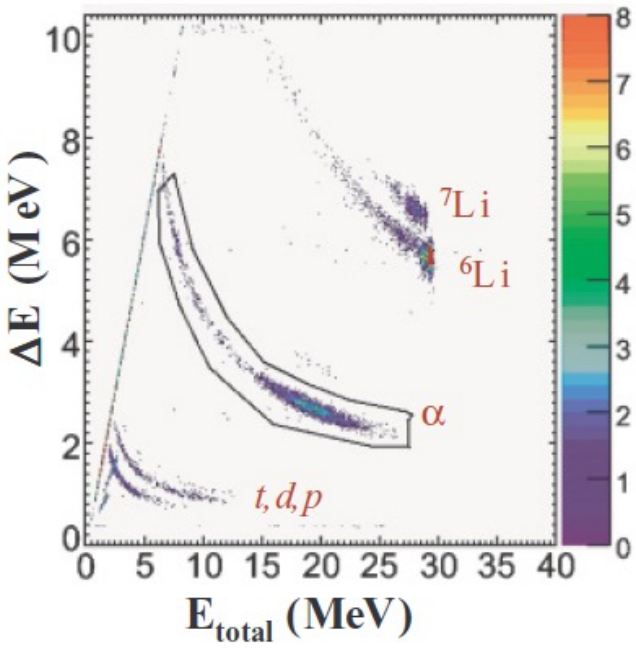

Figure 1.2: A typical two dimensional spectrum of ΔE versus E_{total} for ^{6}Li+^{209}Bi measured by a telescope at $\theta_{\text{lab}} = 118^{o}$ and $E_{\text{beam}} = 32$ MeV, which taken from Ref. [118].

The estimation of inclusive breakup cross sections is required in many situations. For example, Fig. 1.2 shows a typical bidimensional spectrum measured by a detector system at $\theta_{\text{lab}} = 118^{o}$ and $E_{\text{beam}} = 32$ MeV for ^{6}Li+^{209}Bi [118]. It can be seen that the inclusive α yield is much larger than that corresponding to other reaction products. It is a challenging task to understand the reaction mechanisms responsible for such a large cross section of inclusive α. The calculation of inclusive breakup observables is more involved than that for the exclusive ones because they require the inclusion of all the possible processes through which the unobserved particle(s) x can interact with the target A. Given the large number of accessible states, this procedure is unpractical in most cases. As an alternative to this approach, one may try to replace the physical final states by a set of representative states (also named *doorway* states). These can be taken, for example, as the eigenstates of the $x + A$ Hamiltonian in a mean-field potential. As long as the basis used to describe these final states is complete, one may argue that the sum over these representative states should provide results close to those obtained if the sum were done over the true physical states. This procedure, referred to in some works as *transfer to the continuum* method, has been used recently with rather success to describe some inclusive breakup reactions of weakly-bound

projectiles at Coulomb barrier energies, such as ^{208}Pb(^{8}Li,^{7}Li)[100], ^{208}Pb(^{6}He,α)[47], and ^{120}Sn(^{6}He,α)[34]. However, despite this relative success, this method is based on a heuristic approach rather than on a rigorous formal theory. Lacking this formal justification, it is not clear how these *doorway* states should be chosen and how the final calculated cross sections depend on this choice. Another drawback of this approach is that it does not allow to separate the contributions coming from EBU and NEB.

At intermediate energies (above $\sim$100 MeV/u), the problem can be greatly simplified using the *adiabatic* (fast collision) and *eikonal* (forward scattering) approximations, which allows to obtain closed formulas of calculating the inclusive cross sections in terms of the absorption and survival probabilities of the unobserved particle as a function of the impact parameter. This approach has been used extensively in the analysis of nucleon removal (knockout) experiments at intermediate energies, in which typically the removed particle is not observed and only the momentum distributions of the residual core is measured (see, e.g. Refs.[130,59] and references therein). These models, however, cannot be applied to low incident energies (a few MeV/u) and when the energy/momentum transfer is large.

The evaluation of NEB cross sections are needed, for example, in the calculation of total fusion cross sections in reactions induced by weakly-bound projectiles (e.g. ^{6}Li, ^{7}Li, ^{9}Be). A significant fraction of the total fusion cross section comes from incomplete fusion (ICF), in which only part of the projectile fuses with the target, the other fragment surviving after the collision[31]. Although many theoretical efforts have been made to develop suitable models to calculated ICF cross sections[23,68,60], the unambiguous calculation of CF and ICF within a fully quantum mechanical model remains a challenging problem[13,127]. Because the ICF is part of the inclusive breakup, the study of inclusive breakup reactions may lead in turn to a better understanding of ICF.

A related problem is that of the indirect determination of neutron-induced cross sections on short-lived nuclei, from a surrogate reaction which gives rise to the same compound nucleus[46]. This is the case, for example, of the process $A(n,f)$ (where f is a fission fragment) for which the surrogate reaction $A(d,pf)$ may be used. To extract the cross section for the former, one needs to know the fraction of protons produced in the surrogate reaction which are accompanied by the formation of a $n+A$ compound nucleus. Therefore, the applicability of the method requires the separation of the EBU component (which does not lead to compound-nucleus formation) from the NEB (which contains the absorption cross section).

The problem of calculating inclusive breakup cross sections is nevertheless not new. In the late 1970s, the calculations of inclusive breakup had been addressed by several groups. The aim of these theories

was to derive closed-form formulas, in which the sum over all the possible final states of the $x - A$ system was done in a formal way. Baur and his collaborators were the first to propose such closed form formulas. In fact they studied a variety of inclusive-type process [108,17,7]. Their formula was obtained by first writing the elastic breakup DWBA amplitude in the post form, and then by using the unitary of S-matrix and a surface approximation of the form factors of excited states of the residual nucleus. These two approximations were avoided in later works by Udagawa and Tamura [137,136], who used a prior-form DWBA formalism, and by Austern and Vincent [5], who used a post-form DWBA. The later was refined by Kasano and Ichimura [79], who found a formal seperation between elastic breakup and nonelastic breakup. These results were carefully reviewed by Ichimura, Austern, and Vincent [71] and the model was subsequently referred to as the IAV formalism. Later on, Austern et al. reformulated this theory within a more complete three-body model [4].

It is worth noting that the prior-form model of Udagawa and Tamura (UT), on one side, and the post-form DWBA model of Austern and Vincent (AV), on the other side, although formally similar, give different predictions for the NEB part. This led to a long-standing dispute between these two groups, which was finally settled in the referred IAV work [71], where it was demonstrated that a proper derivation of the prior-form formula gives rises to additional terms not considered by UT. The relation between these two models will be discussed in the following section and in Chapter 4.

Although the comparison of these theories with experimental data showed very encouraging results, they have apparently fallen into disuse. Moreover, some of these theories, such as the three-body model of Austern, has never been tested to our knowledge, probably due to the computational limitations at that time. This is in contrast to the experimental situation, in which inclusive breakup measurements are used for many applications, with both stable and unstable beams. Therefore, it seems timely to reexamine these theories and study their applicability to problems of current interest.

The revival and increasing interest on this problem is evidenced by some recent theoretical works on this subject [27,112,92]. These recent applications make use of the IAV model, in DWBA. In Ref. [27], the authors use the zero-range post-form of this model, whereas in Ref. [112] the finite-range prior-form version of the model was used instead. Both of them applied the method to deuteron induced reactions, with encouraging results.

In this work, we revisit also the IAV model, with special emphasis on the calculation of the NEB part, for which we provide a new derivation. We have implemented the DWBA version of this model both in

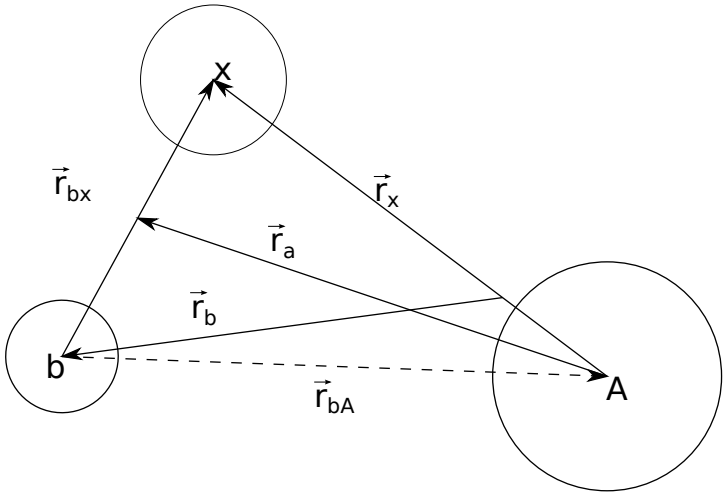

Figure 1.3: Coordinates used in the breakup reaction.

zero-range and in exact finite-range. To assess the validity of this theory, we have performed calculations for several reactions induced by weakly bound nuclei and have compared them with available data.

1.2 Models for inclusive breakup

In this section, the early models for inclusive breakup are reviewed. In all cases, the inclusive breakup is considered as a three body model and the relevant coordinates are depicted in Fig. 1.3.

1.2.1 Baur model

Baur and his collaborators considered the reaction

$$A + a \rightarrow b + B, \tag{1.1}$$

where the projectile a decomposes into the constituents b and x ($a = b + x$) in the Coulomb and nuclear fields of the target nucleus A. B is any possible state between x and A system. Only one part of the fragment, b, is supposed to be detected. They assumed that the system is described by the Hamiltonian

$$H = K + V_{bx} + U_{Ab} + U_{Ax}, \tag{1.2}$$

where K denotes the kinetic energy, and V_{bx}, U_{Ab} and U_{Ax} are the interactions between the 3 particles of the system. The interactions U_{Ab} and U_{Ax} are supposed to be given by phenomenological (complex) optical potentials. The (real) potential V_{bx} gives the bound state of the projectile $a = b + x$.

The $T-$matrix for a given final state of this process in the post form DWBA can be written as*

$$T_{\vec{k}_a \to \vec{k}_b \vec{k}_x} = \int\int \mathrm{d}^3 r_{bx} \mathrm{d}^3 r_a \chi_b^{(-)}(\vec{r}_{bA})^* \chi_x^{(-)}(\vec{r}_x)^* V_{bx}(\vec{r}_{bx}) \varphi_{bx}(\vec{r}_{bx}) \chi_a^{(+)}(\vec{r}_a), \tag{1.3}$$

where $\vec{k}_a$, $\vec{k}_b$, and $\vec{k}_x$ denote the momenta of a, b, and x in the initial and final state. The internal ground state wave function of the projectile a is denoted by $\varphi_{bx}(\vec{r}_{bx})$ and the χ's denote the scattering wave functions of a, b, and x generated by the appropriate optical potentials.

For light particle induced reactions, expression (1.3) can be evaluated in the zero range approximation, introducing the usual zero range constant D_0 (see Sec. 2.3 for details).

The contribution of the elastic breakup to the inclusive (a,b) cross section can be obtained by an integration over the angle of the unobserved particle x. The matrix element expression (1.3) can be expanded in partial waves as

$$T_{\vec{k}_a \to \vec{k}_b \vec{k}_x} = \sum_{l_x m_x} T_{l_x m_x}(\hat{k}_x, \hat{k}_b), \tag{1.4}$$

where

$$\begin{aligned} T_{l_x m_x}(\hat{k}_x, \hat{k}_b) = & \frac{(4\pi)^2 D_0}{k_a k_b k_x} \sum_{l_a l_b} i^{l_a + l_b + l_x} (-)^{l_a - l_b} e^{i(\sigma_{l_a} + \sigma_{l_b} + \sigma_{l_x})} \hat{l}_a \hat{l}_b \langle l_b l_x - m_x m_x | l_a 0 \rangle \\ & \times \langle l_a l_b 00 | l_x 0 \rangle Y_{l_b}^{-m_x}(\hat{k}_b) Y_{l_x}^{m_x}(\hat{k}_x) \int_0^\infty \frac{\mathrm{d}r}{r} \chi_{l_a}(k_a, r) \chi_{l_b}(k_b, r) \chi_{l_x}(k_x, r), \end{aligned} \tag{1.5}$$

where σ_l denote the Coulomb phases. By using the orthogonality of the spherical harmonics the integration over the angle of the unobserved particle x leads to the following expression for the elastic breakup (EBU) double differential cross section

$$\left. \frac{\mathrm{d}^2 \sigma}{\mathrm{d}\Omega_b \mathrm{d}E_b} \right|_{\mathrm{EBU}} = \frac{2\pi}{\hbar v_a} \rho_b(E_b) \rho_x(E_x) \sum_{l_x m_x} \left| T_{l_x m_x}(\hat{k}_b) \right|^2, \tag{1.6}$$

where v_a is the projectile-target relative velocity and $\rho(E) = k\mu/[(2\pi)^3 \hbar^2]$ is the density of states. † Note

*Note that they ignored the remnant term interaction $(U_{bA} - U_{bB})$.

†Note that the parameter $\mu_a \mu_b \mu_x k_b k_x / 4(\pi\hbar^2)^3 k_a$ of Ref[108,17,7] is replaced by $\rho_b(E_b)\rho_x(E_x)2\pi/\hbar v_a$, consistent with our definition of the amplitude for the plane waves as $e^{i\vec{k}\vec{r}}$.

that the sum over the partial waves l_x becomes incoherent.

The processes in which the interaction of the particle x with the target is nonelastic will also contribute to the inclusive spectrum. This is the nonelastic breakup (NEB) defined in the previous section. Within certain approximations the nonelastic breakup cross section can be calculated with the matrix element already needed for elastic breakup.

The starting point of Baur's formula for the NEB is the DWBA expression for the breakup reaction $a + A \to b + c$, where c is one specific two-body final state of the system $B = A + x$:

$$T_{a,bc} = \langle \Phi_{Bc}^{(-)} \chi_b^{(-)} | V_{bx} | \phi_A^0 \varphi_a \chi_a^{(+)} \rangle, \tag{1.7}$$

where ϕ_A^0 is the ground state wave function of nucleus A and Φ_{Bc} is a scattering state of system B with the boundary condition appropriate for channel c. In order to evaluate the transition amplitude (1.7), they first integrate the internal coordinates ξ_A of ψ_A which leads to a generalization of the radial form factor "wave function of the transferred particle") to nonelastic processes:

$$\int \mathrm{d}\xi_A \Phi_{Bc}^{(-)*}(\vec{r}, \xi) \phi_A^0(\xi) = 4\pi \sum_{l_x m_x} i^{l_x} \chi_{l_x}^c(r) Y_{l_x}^{m_x}(\hat{r}) Y_{l_x}^{m_x *}(\hat{k}_c). \tag{1.8}$$

In principle, it would be possible to calculate this form factor with the help a model wave function for $\Phi_{Bc}^{(-)}$. However, this would be very difficult and impracticable if there are too many open channels. To avoid the sum over Φ_{Bc} states, Baur and his collaborators make use of the unitary of the S-matrix for the system $B = A + x$. In addition they assume that the main contribution to the DWBA integral comes from the region outside the nuclear interaction $r > R_0$ [8]. Then the radial form factor $\chi_{l_x}^c$ can be entirely expressed in terms of the scattering matrix element $S_{l_x,c}$, which connects the elastic channel l_x and the nonelastic channel c:

$$\chi_{l_x}^c(r) = \delta_{l_x,c} j_{l_x}(k_x r) + \sqrt{\frac{\mu_x k_x}{\mu_c k_c}} \frac{1}{2} (S_{l_x,c} - \delta_{l_x,c}) h_{l_x}^{(+)}(k_x r), \tag{1.9}$$

where j_l and h_l are, respectively, the spherical Bessel- and Hankel-functions. With the help of the radial form factor, Eq. (1.9), Baur introduced a "reduced" T-matrix for the process $a + A \to b + c$

$$T_{a,bc}^{\mathrm{red}} = \sqrt{\frac{\mu_x k_x}{\mu_c k_c}} \frac{S_{l_x,c}}{S_{l_x,l_x} - 1} D_0 \int \mathrm{d}^3 r \chi_{k_b}^{(-)*}(\vec{r}) [\chi_{l_x}(k_x, r) - j_{l_x}(k_x r)] Y_{l_x}^{m_x}(\hat{r}) \chi_{k_a}^{(+)}(\vec{r}). \tag{1.10}$$

Now the entire dependence on the channel index c appears only in the S-matrix element $S_{l_x,c}$. This allows to sum over all $c \neq l_x$, using the unitarity of the S-matrix,

$$\sum_{c \neq l_x} \left|S_{l_x,c}\right|^2 = 1 - \left|S_{l_x,l_x}\right|^2. \tag{1.11}$$

Using the usual definitions of the elastic and reaction cross section $\sigma_{l_x}^{el}$ and $\sigma_{l_x}^{R}$ the nonelastic breakup cross section can be expressed as [108,17,7]

$$\frac{\mathrm{d}^2\sigma}{\mathrm{d}\Omega_b \mathrm{d}E_b}\Big|_{\mathrm{NEB}} = \frac{2\pi}{\hbar v_a}\rho_b(E_b)\rho_x(E_x)\sum_{l_x m_x}\frac{\sigma_{l_x}^{R}}{\sigma_{l_x}^{el}}\left|T_{l_x m_x} - T_{l_x m_x}^{0}\right|^2, \tag{1.12}$$

where the $T-$matrix has been split into two parts according to equation (1.10). For the inclusive (a,b) double differential cross section, the elastic and nonelastic contributions, Eqs. (1.6) and (1.12) have to be added up.

1.2.2 Udagawa-Tamura model

Udagawa and Tamura (UT) considered the inclusive breakup as a two-step mechanism [137,93], i.e., the process in which breakup of the projectile takes place first, and is followed by an interaction of one member of the broken-up pair with the target nucleus. Such a process can be written as

$$a + A \rightarrow b + x + A \rightarrow b + B^*. \tag{1.13}$$

A feature of this process is that, after the first breakup, the fragment b behaves as a spectator, and thus the remaning process can be viewed as essentially a two-body interaction. This inclusdes the elastic scattering of x on A (*elastic breakup*), and the absorption of x with A (*breakup fusion*[‡]).

The starting point of UT is the relation [30]

$$\sigma_a^R = -\frac{2}{\hbar v_a}\langle \chi_a^{(+)}\left|W_a\right|\chi_a^{(+)}\rangle, \tag{1.14}$$

where σ_a^R is the reaction cross section, while $\chi_a^{(+)}$ and W_a are, respectively, the distorted wave function in the incident channel, and the imaginary part of the optical potential used in generating $\chi_a^{(+)}$.

[‡]Note that the *breakup fusion* of UT corresponds to the NEB according to the terminology adopted throughout this work.

In order to calculate the elastic breakup and breakup fusion cross sections, UT first single out σ_d and W_d, i.e., the cross section and the imaginary part of the optical potential, from the first step of Eq. (1.13) which is called channel $d(= b + x + A)$. Using the Feshbach formalism [80,49,138]

$$W_d = \mathrm{Im}\langle \phi_A^0 | V_{\mathrm{prior}} G_d^{(+)} V_{\mathrm{prior}} | \phi_A^0 \rangle, \tag{1.15}$$

and

$$\sigma_d = -\frac{2}{\hbar v_a} \langle \chi_a^{(+)} | W_d | \chi_a^{(+)} \rangle, \tag{1.16}$$

where ϕ_A^0 is the target ground state wave function, $V_{\mathrm{prior}} = V_{xA} + U_{bA} - U_{aA}$ is the prior form interaction and $G_d^{(+)}$ is the Green's function for the propagation in the d channel. In addition, UT assume $V_{xA} \to U_{xA}$ and then the optical model Green's function can be written as

$$G_d^{(+)} = \frac{1}{E - H_0 - K_{xA} - K_{bB} - U_{xA} - U_{bB} + i\varepsilon}, \tag{1.17}$$

where H_0 denotes the intrinsic Hamiltonian, and K_i and U_i are the kinetic energies and optical potentials. The absorption of x by A is thus described by the imaginary part of U_{xA}. In order to isolate the absorption due to this imaginary potential, UT used the following identity for $G_d^{(+)}$:

$$G_d^{(+)} = \Omega_{bB}^{(-)} [\omega_{xA}^{(-)} g^{(+)} \omega_{xA}^{(-)\dagger} - G_{xA}^{(+)\dagger} U_{xA}^{\dagger} G_{xA}^{(+)}] \Omega_{bB}^{(-)\dagger} - \Omega_{xA}^{(-)} G_{bB}^{(+)\dagger} U_{bB}^{\dagger} G_{bB}^{(+)} \Omega_{xA}^{(-)\dagger}, \tag{1.18}$$

where

$$\begin{aligned} \omega_i^{(-)} &= 1 + G_i^{(+)\dagger} U_i^{\dagger}, \\ G_i^{(+)} &= 1/(E - H_0 - K_{xA} - K_{bB} - U_i + i\varepsilon), \\ \Omega_i^{(-)} &= 1 + G_d^{(+)\dagger} U_i^{\dagger}, \\ g^{(+)} &= 1/(E - H_0 - K_{xA} - K_{bB} + i\varepsilon). \end{aligned} \tag{1.19}$$

Note that $\omega_i^{(-)}$ is nothing but the wave operator that, acting on a plane wave, generates a distorted wave. Also $g^{(+)}$ is the free Green's function, while $G_i^{(+)}$ is the optical model Green's function. Based on the fundamental assumption mentioned above that after the breakup b can be treated as a spectator, UT neglect

the last term in Eq. (1.18), and approximate $\Omega_b^{(-)}$ by $\omega_b^{(-)}$, i.e.,

$$\Omega_{xA}^{(-)} G_{bB}^{(+)\dagger} U_{bB}^{\dagger} G_{bB}^{(+)} \Omega_{xA}^{(-)\dagger} \simeq 0 \quad \text{and} \quad \Omega_b^{(-)} \simeq \omega_b^{(-)}. \tag{1.20}$$

Using Eq. (1.18) and Eq. (1.20) in Eq. (1.16), it is obtained

$$\sigma_d = \int \mathrm{d}E_b \mathrm{d}\Omega_b \frac{2\pi}{\hbar v_a} \rho_b(E_b) \Big(\sum_{\vec{k}_x} \left| \langle \chi_b^{(-)} \chi_x^{(-)}(\vec{k}_x) \right| V_{\text{prior}} \left| \chi_a^{(+)} \varphi_a \right\rangle \right|^2 - \langle \psi_x \left| W_x \right| \psi_x \rangle / \pi \Big). \tag{1.21}$$

Here $\chi_x^{(-)}$ and $\chi_b^{(-)}$ denote the distorted waves for the relative motion between $x-A$ and $b-B$ respectively, φ_a is the bound state wave function of the projectile a, while ψ_x is the wave function in the channel x which is given by

$$\psi_x^{\text{UT}}(\vec{r}_x) = G_{xA}^{(+)} (\chi_b^{(-)} \left| V_{\text{prior}} \right| \chi_a^{(+)} \varphi_a \rangle, \tag{1.22}$$

where the round bracket $(|\rangle$ indicates integration over $b-$coordinates only. The physical meaning of Eq. (1.21) is clear. This first term is the elastic breakup cross section in the DWBA form, while the second term describes the breakup-fusion process. This second term is given, in differential form, by

$$\left. \frac{\mathrm{d}^2\sigma}{\mathrm{d}\Omega_b \mathrm{d}E_b} \right|_{\text{BF}}^{\text{UT}} = -\frac{2}{\hbar v_a} \rho_b(E_b) \langle \psi_x^{\text{UT}} \left| W_x \right| \psi_x^{\text{UT}} \rangle. \tag{1.23}$$

This result was also derived by Kerman and McVoy (see Eq. (33) of Ref.[84]).

1.2.3 Ichimura-Austern-Vincent model

In the work of Ichimura, Austern and Vincent[71], they consider the reaction of the form

$$a + A \to b + \text{anything}, \tag{1.24}$$

where b is a definite fragment of the incident projectile and the energy of b is low enough so the remaining system $x + A$ is unbound.

The model Hamiltonian for this process can be written as

$$H = H_A(\xi) + K_{bB} + K_{xA} + V_{xA} + U_{bA} + V_{bx}, \tag{1.25}$$

in which the interaction V_{bA} of the spectator particle with the target nucleus has been replaced by the optical potential U_{bA}. Thus it is assumed that possible excitations of the target nucleus due to its interaction with b are embedded in the imaginary part of U_{bA}. Since explicit wave functions and Hamiltonians for the internal states of b and x are not needed, for simplicity they are not included in our notation. The target nucleus ground state wave function is written as ϕ^0_A, with energy E_A, so

$$H_A\phi^0_A = E_A\phi^0_A. \tag{1.26}$$

The eigenstates of the system $x + A$ are written Ψ^c_{xA}, and they satisfy

$$H_{xA}\Psi^c_{xA} = E^c\Psi^c_{xA}, \tag{1.27}$$

with

$$H_{xA} \equiv H_A + K_{xA} + V_{xA}. \tag{1.28}$$

In general, the post-form DWBA expression for inclusive breakup of outgoing b particles is

$$\left.\frac{\mathrm{d}^2\sigma}{\mathrm{d}\Omega_b \mathrm{d}E_b}\right|_{\text{post}} = \frac{2\pi}{\hbar v_a}\rho(E_b)\sum_c |\langle\chi^{(-)}_b\Psi^c_{xA}|V_{\text{post}}|\chi^{(+)}_a\varphi_a\phi^0_A\rangle|^2\delta(E - E_b - E^c), \tag{1.29}$$

where $\rho(E_b) = \mu_b k_b/(8\pi^3\hbar^2)$ is the density of states and $V_{\text{post}} = V_{bx} + U_{bA} - U_{bB}$ is the post form interaction. Here we use distorted wave functions defined by

$$[K_a + U_a(r_a)]\chi^{(+)}_a(\vec{r}_a) = (E - E_A - E_a)\chi^{(+)}_a(\vec{r}_a), \tag{1.30}$$

and

$$[K_b + U^\dagger_{bB}(r_b)]\chi^{(-)}_b(\vec{r}_b) = E_b\chi^{(-)}_b(\vec{r}_b), \tag{1.31}$$

where a denotes the incoming channel $a + A$ and b denotes the outgoing channel $b + B^*$, where B^* is any possible state of the $(x + A)$ system. To evaluate Eq. (1.29) first the delta function is written as the imaginary part of an energy denominator (the Sokhotski–Plemelj theorem[123])

$$\delta(E - E_b - E^c) = -\frac{1}{\pi}\mathrm{Im}\frac{1}{E^+ - E_b - E^c}. \tag{1.32}$$

Then, one gets

$$\left.\frac{\mathrm{d}^2\sigma}{\mathrm{d}\Omega_b \mathrm{d}E_b}\right|_{\text{post}} = -\frac{2}{\hbar v_a}\rho(E_b)\mathrm{Im}\sum_c \langle \chi_a^{(+)}\varphi_a\phi_A^0|V_{\text{post}}|\chi_b^{(-)}\Psi_{xA}^c\rangle(E^+ - E_b - E^c)^{-1} \times \langle \Psi_{xA}^c\chi_b^{(-)}|V_{\text{post}}|\chi_a^{(+)}\varphi_a\phi_A^0\rangle. \tag{1.33}$$

The energy denominator is taken inside of the matrix elements and replaced by the Green's function of the many body system

$$\langle\phi_A^0|(E^+ - E_b - E^c)^{-1}|\phi_A^0\rangle = \langle\phi_A^0|(E^+ - E_b - H_{xA})^{-1}|\phi_A^0\rangle. \tag{1.34}$$

Next, one applies the closure over the states of Ψ_{xA}^c

$$\sum_c |\Psi_{xA}^c\rangle\langle\Psi_{xA}^c| = 1. \tag{1.35}$$

The sum on c is performed as

$$\left.\frac{\mathrm{d}^2\sigma}{\mathrm{d}\Omega_b \mathrm{d}E_b}\right|_{\text{post}} = -\frac{2}{\hbar v_a}\rho(E_b)\mathrm{Im}\langle\phi_A^0\chi_a^{(+)}\varphi_a|V_{\text{post}}|\chi_b^{(-)}\rangle(E^+ - E_b - H_{xA})^{-1} \times \langle \chi_b^{(-)}|V_{\text{post}}|\chi_a^{(+)}\varphi_a\phi_A^0\rangle. \tag{1.36}$$

Because V_{post} and the optical wave function do not depend on the internal coordinates of the target nucleus, the ϕ_A^0 expectation allows the optical reduction

$$(\phi_A^0|(E^+ - E_b - H_{xA})^{-1}|\phi_A^0) = (E_x^+ - K_{xA} - U_{xA})^{-1} \equiv G_x \tag{1.37}$$

where $E_x \equiv E - E_b - E_A$ and U_x is the Feshbach formal optical potential for particle x. Then

$$\left.\frac{\mathrm{d}^2\sigma}{\mathrm{d}\Omega_b \mathrm{d}E_b}\right|_{\text{post}} = -\frac{2}{\hbar v_a}\rho(E_b)\mathrm{Im}\langle\rho_b(\vec{r}_x)|G_x|\rho_b(\vec{r}_x)\rangle \tag{1.38}$$

with the source function

$$\rho_b(\vec{r}_x) \equiv (\chi_b^{(-)}|V_{\text{post}}|\chi_a^{(+)}\varphi_a\rangle \tag{1.39}$$

A helpful transformation [71,79] of the Green's function is obtained from the adjoint pair of equations

$$G_x = G_0(1 + U_x G_x) = (1 + G_x^\dagger U_x^\dagger) G_0 (1 + U_x G_x) - G_x^\dagger U_x^\dagger G_x \tag{1.40}$$

$$G_x^\dagger = (1 + G_x^\dagger U_x^\dagger) G_0^\dagger = (1 + G_x^\dagger U_x^\dagger) G_0^\dagger (1 + U_x G_x) - G_x^\dagger U_x G_x \tag{1.41}$$

in which G_0 is the free Green's function for channel x at relative energy E_x. By subtraction of these equations,

$$\mathrm{Im}G_x \equiv \frac{1}{2i}(G_x - G_x^\dagger) = (1 + G_x^\dagger U_x^\dagger)\mathrm{Im}G_0(1 + U_x G_x) - G_x^\dagger W_x G_x \tag{1.42}$$

in which W_x is the imaginary part of U_x, and

$$\mathrm{Im}G_0 = -\pi\delta(E_x - K_x). \tag{1.43}$$

Then

$$\begin{aligned}\left.\frac{\mathrm{d}^2\sigma}{\mathrm{d}\Omega_b \mathrm{d}E_b}\right|_{\mathrm{post}} &= \frac{2\pi}{\hbar v_a}\rho(E_b)\langle\rho_b(\vec{r}_x)|(1 + G_x^\dagger U_x^\dagger)\delta(E_x - K_x)(1 + U_x G_x)|\rho_b(\vec{r}_x)\rangle \\ &\quad - \frac{2}{\hbar v_a}\rho(E_b)\langle\rho_b(\vec{r}_x)|G_x^\dagger W_x G_x|\rho_b(\vec{r}_x)\rangle.\end{aligned} \tag{1.44}$$

The distorted wave for particle x is introduced as

$$|\chi_x^{(-)}\rangle = (1 + G_x^\dagger U_x^\dagger)|\vec{k}_x\rangle, \tag{1.45}$$

where $K_x|\vec{k}_x\rangle = (\hbar^2 k_x^2/2\mu_x)|\vec{k}_x\rangle$. Then the first term of Eq. (1.44) is rewritten as

$$\begin{aligned}&\frac{2\pi}{\hbar v_a}\rho(E_b)\int \mathrm{d}^3k_x|\langle\rho_b(\vec{r}_x)|\chi_x^{(-)}\rangle|^2\delta(E_x - \hbar^2 k_x/2\mu_x) \\ &= \frac{2\pi}{\hbar v_a}\rho(E_b)\int \mathrm{d}^3k_x|\langle\chi_b^{(-)}\chi_x^{(-)}|V_{\mathrm{post}}|\chi_a^{(+)}\varphi_a\rangle|^2\delta(E_x - \frac{\hbar^2 k_x^2}{2\mu_x}).\end{aligned} \tag{1.46}$$

This is nothing but the energy-averaged elastic breakup cross section. The second term of Eq. (1.44) can be written as

$$\left.\frac{\mathrm{d}^2\sigma}{\mathrm{d}\Omega_b \mathrm{d}E_b}\right|_{\mathrm{NEB}}^{\mathrm{IAV}} = -\frac{2}{\hbar v_a}\rho(E_b)\langle\psi_x^{\mathrm{IAV}}(\vec{r}_x)|W_x|\psi_x^{\mathrm{IAV}}(\vec{r}_x)\rangle \tag{1.47}$$

with

$$\psi_x^{\mathrm{IAV}}(\vec{r}_x) = G_x \rho_b(\vec{r}_x) \tag{1.48}$$

Note that the Baur model, Eq. (1.12), is an approximation of the second term of Eq. (1.47).

1.2.4 Hussein and McVoy model

Hussein and McVoy considered the multi-channel problem in which the channels are defined by the states $|n\rangle$ of the target, and choose the projection operators

$$\mathcal{P} = |0\rangle\langle 0|, \quad \mathcal{Q} = 1 - \mathcal{P}. \tag{1.49}$$

Considering the interaction in the form $U^{\mathcal{P}} + V_{\mathcal{Q}\mathcal{P}}$ for this purpose, where $U^{\mathcal{P}}$ is the optical potential in channel $\mathcal{P}$, its eigenfunction $\mathcal{P}\Psi^{(+)}$ contains none of the reaction channels produced by $V_{\mathcal{Q}\mathcal{P}}$, so it can be written as $\chi_a^{(+)}|\varphi_a\phi_A^0\rangle$; this includes the full elastic optical distortion in the definition of the incident wave. Then Ψ^f is any exact final state in the $\mathcal{Q}$-space. For the same reaction type as discussed before[67,69],i.e., Eq. (1.1), (1.13) and (1.24). Hussein and McVoy write the matrix elements in the "prior" form[67], which considers the interaction causing the fragmentation to be the entrance-channel potential,

$$V_{\mathcal{Q}\mathcal{P}} = V_{xA}^{\mathcal{Q}\mathcal{P}} + V_{bA}^{\mathcal{Q}\mathcal{P}}, \tag{1.50}$$

and choosing b as the spectator means that $\mathcal{Q}V_{bA}\mathcal{P}$ can be neglected as far as the reaction is concerned. Thus the spectator model matrix element can be written as

$$T_{\mathrm{HM}}^c = \langle \chi_b^{(-)}\Psi_{xA}^c \big| V_{xA}^{\mathcal{Q}\mathcal{P}} \big| \varphi_a \chi_a^{(+)}\phi_A^0 \rangle, \tag{1.51}$$

where Ψ^c_{xA} is the exact wave function for any possible state of $x-A$ system including the internal state of A. Then the nonelastic breakup cross section can be written as

$$\begin{aligned}\left.\frac{\mathrm{d}^2\sigma}{\mathrm{d}E_b\mathrm{d}\Omega_b}\right|^{\mathrm{HM}} &= \frac{2\pi}{\hbar v_a}\rho_b(E_b)\sum_c \left|T^c_{\mathrm{HM}}\right|^2\delta(E_a+B_a-E_b-E^c)\\ &= \frac{2\pi}{\hbar v_a}\rho_b(E_b)\langle\chi^{(+)}_a\chi^{(-)\dagger}_b\varphi_a|\phi^0_A|V^{\mathcal{PQ}}_{xA}\delta(E_a+B_a-E_b-H^{\mathcal{QQ}}_{xA})V^{\mathcal{PQ}}_{xA}|\phi^0_A\rangle\chi^{(+)}_a\chi^{(-)\dagger}_b\varphi_a\rangle\\ &= -\frac{2}{\hbar v_a}\rho_b(E_b)\langle\chi^{(+)}_a\chi^{(-)\dagger}_b\varphi_a|W_x|\chi^{(+)}_a\chi^{(-)\dagger}_b\varphi_a\rangle, \end{aligned} \tag{1.52}$$

where $B_a>0$ is the binding energy of the projectile a and note that the closure sum was done within the $\mathcal{Q}-$space. Now the Hussein-McVoy's $x-A$ channel wave function is defined as

$$\psi^{\mathrm{HM}}_x(\vec{r}_x) = \left(\chi^{(-)}_b(\vec{r}_b)\middle|\varphi_a(r_{bx})\chi^{(+)}_a(\vec{r}_a)\right\rangle, \tag{1.53}$$

Finally, the NEB cross section can be written as

$$\left.\frac{\mathrm{d}^2\sigma}{\mathrm{d}E_b\mathrm{d}\Omega_b}\right|^{\mathrm{HM}} = -\frac{2}{\hbar v_a}\rho_b(E_b)\langle\psi^{\mathrm{HM}}_x|W_x|\psi^{\mathrm{HM}}_x\rangle. \tag{1.54}$$

Note that, in the original paper of Hussein and McVoy[67], they interpreted Eq. (1.54) as the total inclusive breakup cross section, but latter it turned out that Eq. (1.54) only represents the nonelastic breakup part[69]

.

1.2.5 Relation between *post* and *prior* forms

This section will focus on the relation between the model of Udagawa and Tamura (UT), and that by Ichimura, Austern and Vincent (IAV). The main difference between these models is that, whereas UT use the prior-form DWBA, IAV employ the post-form representation. Although the final expressions for these models have the same formal structure ,i.e., Eq. (1.23) and Eq. (1.47), they lead to different predictions for the NEB cross sections. To show the relation between the *post* and *prior* DWBA expressions, we follow Li, Udagawa and Tamura[93]. They start from the relation between the *post-prior* interactions, i.e.,

$$V_{\mathrm{prior}} = H_a + V_{\mathrm{prior}} - E_a = H_b + H_x + V_{\mathrm{post}} - E_a = H_x - E_x + V_{\mathrm{post}}, \tag{1.55}$$

where H_a, H_b, and H_x are defined as

$$\begin{aligned} H_a &= h_a + K_{aA} + U_{aA}, \\ H_b &= K_{bB} + U_{bB}, \\ H_x &= K_{xA} + U_{xA}, \end{aligned} \tag{1.56}$$

where h_a is the intrinsic Hamiltonian of the projectile a, while

$$\begin{aligned} V_{\text{prior}} &= V_{aA} - U_{aA} = U_{xA} + U_{bA} - U_{aA}, \\ V_{\text{post}} &= V_{bx} + V_{aA} - U_{bB} - U_{xA} = V_{bx} + U_{bA} - U_{bB}. \end{aligned} \tag{1.57}$$

Inserting Eq. (1.55) into Eq. (1.22) one gets

$$\psi_x^{\text{IAV}}(\vec{r}_x) = \psi_x^{\text{UT}}(\vec{r}_x) + \psi_x^{\text{HM}}(\vec{r}_x), \tag{1.58}$$

where $\psi_x^{\text{HM}}(\vec{r}_x)$ is also called nonorthogonality term. Replacing Eq. (1.58) into Eq. (1.47) results

$$\left.\frac{\mathrm{d}^2\sigma}{\mathrm{d}E_b\mathrm{d}\Omega_b}\right|_{\text{NEB}}^{\text{IAV}} = \left.\frac{\mathrm{d}^2\sigma}{\mathrm{d}E_b\mathrm{d}\Omega_b}\right|_{\text{NEB}}^{\text{UT}} + \left.\frac{\mathrm{d}^2\sigma}{\mathrm{d}E_b\mathrm{d}\Omega_b}\right|_{\text{NEB}}^{\text{HM}} + \left.\frac{\mathrm{d}^2\sigma}{\mathrm{d}E_b\mathrm{d}\Omega_b}\right|_{\text{NEB}}^{\text{IN}}, \tag{1.59}$$

where the interference (IN) term *cross section* is defined as

$$\left.\frac{\mathrm{d}^2\sigma}{\mathrm{d}E_b\mathrm{d}\Omega_b}\right|_{\text{NEB}}^{\text{IN}} = -\frac{4}{\hbar v_a}\rho_b(E_b)\mathrm{Re}\langle\psi_x^{\text{UT}}|W_{xA}|\psi_x^{\text{HM}}\rangle. \tag{1.60}$$

Equation (1.59) represents the post-prior equivalence of the NEB cross sections in the IAV model, with the RHS corresponding to the prior-form expression of this model. The first term is just the UT formula, Eq. (1.23), which is formally analogous to the IAV post-form formula Eq. (1.47), but with the x-channel wave function given by $\psi_x^{\text{UT}}(\vec{r}_x)$. The two additional terms, which are responsible for the discrepancy of the IAV and UT results, arise from the nonorthogonality overlap (HM term). These terms ensure the post-prior equivalence of the NEB cross sections. However, UT considered that these two additional terms are unphysical and hence that the post-prior equivalence does not hold for the NEB. We note here that this problem does not arise for the EBU part, for which the post and prior formulas are well known to give identical results[71].

The rest of this dissertation is organized as follows. In Chapter 2 we revisit the formal aspects of the model developed by Ichimura, Austern and Vincent, for which we have presented an alternative derivation of the NEB formula. In Chapter 3, the formalism is applied to several inclusive reactions induced by d, ^{6}Li, ^{11}Be, ^{7}Li, ^{7}Be and ^{8}B. In Chapter 4, we discuss the numerical assessment of post-prior equivalence. In Chapter 5, we present possible extensions of IAV model to *incomplete fusion* (ICF) calculations. Finally, we summarize the main results of this work and outline some future developments in Chapter 6.

If people do not believe that mathematics is simple, it is only because they do not realize how complicated life is.

John von Neumann

2

IAV and UT Models

In this chapter, we revisit the formal aspects of the Ichimura, Austern, Vincent model[71]. We provide an alternative derivation of the NEB formula, based on a direct application of the coupled-channels optical theorem. As we will see, this provides a transparent interpretation of the NEB as the part of the flux that leaves the EBU channels to more complicated configurations of the $x+A$ system. Afterwards, we discuss some technical and formal aspects related to the practical implementation of the model, such as its partial wave expansion and the treatment of the slow-converging integrals appearing in the post-form breakup matrix elements. Finally, we also discuss the possibility of using IAV model to include final bound states of the $x+A$ system.

2.1 The Ichimura, Austern, Vincent (IAV) model

In this section we briefly review the model of Ichimura, Austern and Vincent[71,4]. The final formula obtained in this model has been derived in different ways. Here, we closely follow the early derivation done by Austern and Vincent[5] because, as we will show, it provides an interesting physical insight.

We write the process under study as

$$a(=b+x)+A \rightarrow b+B^{*}. \tag{2.1}$$

This process will be described with the Hamiltonian

$$H = K + V_{bx} + U_{bA}(\vec{r}_{bA}) + H_A(\xi) + V_{xA}(\xi, \vec{r}_x), \tag{2.2}$$

where K is the total kinetic energy operator, V_{bx} is the interaction binding the two clusters b and x in the projectile a, $H_A(\xi)$ is the Hamiltonian of the target nucleus (with ξ denoting its internal coordinates) and V_{xA} and U_{bA} are the fragment–target interactions. The relevant coordinates are depicted in Fig. 1.3. Note that the coordinate $\vec{r}_b$ connects the particle b with the center of mass (c.m.) of the $x+A$ system.

In writing the Hamiltonian of the system in the form (2.2) we make a clear distinction between the two cluster constituents; the interaction of the fragment b, the one that is assumed to be detected in the experiment, is described with an optical potential. Non-elastic processes arising from this interaction (e.g. target excitation), are included only effectively through U_{bA}. The particle b is said to act as *spectator*. On the other hand, the interaction of the particle x with the target retains the dependence of the target degrees of freedom (ξ).

Within the assumed three-body model, and using the post-form representation, the total wave function of the system can be written in integral form as

$$\Psi(\xi, \vec{r}_x, \vec{r}_b) = \left[E^{+} - K_b - U_{bB} - H_B\right]^{-1} V_{\text{post}} \Psi(\xi, \vec{r}_x, \vec{r}_b), \tag{2.3}$$

where $E^{+} = E + i\varepsilon$, $\varepsilon \rightarrow 0$, U_{bB} is an auxiliary (and, in principle, arbitrary) potential between b and the composite B, $V_{\text{post}} \equiv V_{bx} + U_{bA} - U_{bB}$ and H_B is the Hamiltonian of the x+A pair, given by

$$H_B(\xi, \vec{r}_x) = H_A(\xi) + K_x + V_{xA}(\xi, \vec{r}_x). \tag{2.4}$$

The eigenstates of the target Hamiltonian will be denoted as $\varphi_A^c(\xi)$, i.e., $[H_A(\xi_A) - E_A^c]\varphi_A^c(\xi) = 0$, with $c = 0$ corresponding to the target ground state, for which we assume $E_A^0 = 0$.

We consider now a specific final state of the detected particle b, characterized by a given final momentum of this fragment ($\vec{k}_b$). The motion of b will be described by a distorted wave with momentum $\vec{k}_b$,

obtained as a solution of the single-channel equation

$$\left[K_b + U^{\dagger}_{bB} - E_b\right] \chi_b^{(-)}(\vec{k}_b, \vec{r}_b) = 0. \tag{2.5}$$

The wave function describing the motion of x after the breakup, that will be denoted as $Z_x(\xi, \vec{r}_x)$, can be obtained projecting the total wave function [Eq. (2.3)] onto this particular state of the b particle, i.e., [*]

$$Z_x(\vec{k}_b, \xi, \vec{r}_x) \equiv (\chi_b^{(-)}|\Psi\rangle = \left[E^+ - E_b - H_B\right]^{-1} (\chi_b^{(-)}|V_{\rm post}|\Psi\rangle, \tag{2.6}$$

where the round bracket denotes integration over $\vec{r}_b$ only. The last equation can be also written in differential form as

$$\left[E^+ - E_b - H_B\right] Z_x(\vec{k}_b, \xi, \vec{r}_x) = (\chi_b^{(-)}|V_{\rm post}|\Psi\rangle. \tag{2.7}$$

The source term of this equation involves the exact and hence unknown wave function Ψ which, in actual calculations, must be approximated by some calculable form. For example, in DWBA, one assumes the factorized form

$$\Psi(\xi, \vec{r}_x, \vec{r}_b) \approx \varphi_A^0(\xi)\varphi_a(\vec{r}_{bx})\chi_a^{(+)}(\vec{k}_a, \vec{r}_a), \tag{2.8}$$

where $\varphi_a(\vec{r}_{bx})$ is the projectile ground-state wave function and $\chi_a^{(+)}(\vec{k}_a, \vec{r}_a)$ is a distorted wave describing the $a + A$ motion in the incident channel. In practice, the latter is commonly replaced by the solution of some optical potential describing $a + A$ elastic scattering. Austern *et al.* [4] proposed also the three-body approximation

$$\Psi(\xi, \vec{r}_x, \vec{r}_b) \approx \varphi_A^0(\xi)\Psi^{\rm 3b}(\vec{r}_x, \vec{r}_b), \tag{2.9}$$

where $\Psi^{\rm 3b}$ is a three-body wave function for the three fragments (x+b+A) and contains, in addition to the $b + x$ ground state, contributions from $b + x$ inelastic scattering and breakup.

It is worth noting that, either in the approximation (2.8) or in (2.9), the three-body wave function does not contain explicitly excited states of A. Thus, in the IAV model, the NEB can be viewed as a two-step process in which the first step is the dissociation of the projectile, leaving the target in its ground state, while the second step is the absorption of x or the excitation of A.

A possible procedure to solve Eq. (2.7) is to expand the function Z_x in a complete set of $x + A$ states,

[*] Note that this function will also depend on $\vec{k}_a$, which indicates the direction of the incident beam. Because this direction is fixed, this dependence will be omitted for simplicity of the notation.

i.e.,

$$Z_x(\vec{k}_b,\xi,\vec{r}_x) = \sum_c \psi_x^c(\vec{k}_b,\vec{r}_x)\varphi_A^c(\xi), \tag{2.10}$$

where $\psi_x^c(\vec{k}_b,\vec{r}_x)$ describes the $x-A$ relative motion when the target is in the state c. The expansion (2.10) can be inserted into Eq. (2.7), giving rise to a set of coupled equations for the unknown functions $\psi_x^c(\vec{k}_b,\vec{r}_x)$.

This approach will be in general unpractical because the expansion (2.10) involves a very large number of final states. If one is not interested in the description of the transition to specific $x+A$ states, but rather in their summed contribution, one can proceed as follows. Following Feshbach, the $Z_x(\vec{k}_b,\xi,\vec{r}_x)$ function is decomposed as

$$Z_x(\vec{k}_b,\xi,\vec{r}_x) = \mathcal{P}Z_x + \mathcal{Q}Z_x, \tag{2.11}$$

where $\mathcal{P}$ is the projector operator onto the target ground state and $\mathcal{Q} = 1-\mathcal{P}$. From Eq. (2.10) we see that $\mathcal{P}Z_x = \psi_x^0(\vec{k}_b,\vec{r}_x)\varphi_A^0(\xi)$. The function $\psi_x^0(\vec{k}_b,\vec{r}_x)$, which describes the $x+A$ relative motion when the target is in the ground state, verifies the equation

$$(E_x^+ - K_x - \mathcal{U}_x)\psi_x^0(\vec{k}_b,\vec{r}_x) = \rho(\vec{k}_b,\vec{r}_x), \tag{2.12}$$

with $E_x = E - E_b$, $\rho(\vec{k}_b,\vec{r}_x) \equiv (\chi_b^{(-)}|V_{bx}|\Psi\rangle$ is the so-called source term, and $\mathcal{U}_x$ the formal optical model potential describing $x+A$ elastic scattering. Explicitly,

$$\mathcal{U}_x = \langle\varphi_A^0|V_{xA} + V_{xA}Q[E^+ - E_b - H_{QQ}]^{-1}V_{xA}|\varphi_A^0\rangle, \tag{2.13}$$

where $H_{QQ} \equiv \mathcal{Q}H_B\mathcal{Q}$. The formal potential $\mathcal{U}_x$ is a complicated non-local, angular- and energy-dependent object. However, as done in two-body scattering problems, it can be approximated by some energy-averaged (possibly local) potential or by some phenomenological representation (denoted U_x hereafter) with parameters adjusted to describe $x+A$ elastic scattering.

Note that Eq. (2.12) is formally analogous to the inhomogeneous equation appearing in DWBA and CCBA calculations between bound states, as formulated in the *source term method* of Ascuitto and Glendenning[3], and used by several coupled-channels codes[128].

2.1.1 Separation of elastic and nonelastic breakup

In their original paper, Austern and Vincent provide only the total inclusive cross section. Later on, Kasano and Ichimura [79] showed that this expression can be formally decomposed into two pieces, corresponding to the elastic breakup (EBU) and non-elastic breakup (NEB) contributions.

Here, we present an alternative derivation of these formulas, which exploits the aforementioned analogy of Eq. (2.12) with that found in the DWBA/CCBA formalisms. This equation is to be solved with purely outgoing boundary conditions (since there are no incoming waves in the $x-A$ channel), that is,

$$\psi_x^0(\vec{k}_b,\vec{r}_x) \to f(\vec{k}_b,\hat{r}_x)\frac{e^{ik_x r_x}}{r_x}. \tag{2.14}$$

The function $f(\vec{k}_b,\hat{r}_x)$ depends, in addition to the direction of $\vec{k}_b$, on the angular part of $\vec{r}_x$. Asymptotically, when r_x is large, the position vector $\vec{r}_x$ becomes parallel to the momentum $\vec{k}_x$ and we may write $f(\vec{k}_b,\hat{r}_x) \to f(\vec{k}_b,\vec{k}_x)$. We therefore recognize $f(\vec{k}_b,\vec{k}_x)$ as the scattering amplitude for the elastic breakup process, and its square is proportional to the differential cross section for the detection of the x particle in the direction of $\vec{k}_x$, and the b particle in the direction $\vec{k}_b$. To obtain this amplitude, one can proceed in two different ways. One possibility is to integrate the differential equation (2.12) and, at a sufficiently large distance (beyond the range of the short-range potentials), equate the solution to the asymptotic form (2.14), from which the scattering amplitude can be obtained. A second approach to solve Eq. (2.12) is to use integral methods (e.g., Green's function) techniques. This latter procedure gives the following closed-form expression for the scattering amplitude,

$$f(\vec{k}_b,\vec{k}_x) = -\frac{\mu_x}{2\pi\hbar^2}\langle\chi_x^{(-)}\chi_b^{(-)}|V_{\rm post}|\Psi^{3b}\rangle, \tag{2.15}$$

where μ_x is the reduced mass of the $x+A$ system and the distorted wave $\chi_x^{(-)}(\vec{k}_x,\vec{r}_x)$ is a solution of the homogeneous part of equation Eq. (2.12), i.e.,

$$\left[K_x + U_x^{\dagger} - E_x\right]\chi_x^{(-)}(\vec{k}_x,\vec{r}_x) = 0, \tag{2.16}$$

whose solution consists of a plane wave of momentum $\vec{k}_x$ plus an ingoing spherical wave.

The corresponding differential cross section, for a final differential volume in momentum space, is

given by[†] (c.f., for instance, Eq. (5.36) of Ref.[54])

$$d\sigma = \frac{(2\pi)^{-5}}{\hbar v_a} \int d\vec{k}_x d\vec{k}_b d\vec{k}_A \, \delta(E_f - E_i)\delta(\vec{P}_f - \vec{P}_i)|T_{fi}|^2, \tag{2.17}$$

where T_{fi} is the usual transition amplitude (or T-matrix), which is related to the scattering amplitude by $f = -(\mu_x/2\pi\hbar^2)T_{fi}$. In the c.m. frame, $\vec{P}_i = 0$. Also, the target momentum ($\vec{k}_A$) is not measured, so we can integrate over it, making use of the momentum-conserving delta function,

$$d\sigma = \frac{(2\pi)^{-5}}{\hbar v_a} \int d\vec{k}_x d\vec{k}_b \delta(E_f - E_i)|T_{fi}|^2. \tag{2.18}$$

The element $d\vec{k}_b$ is conveniently expressed in terms of energy and solid angle elements using $d\vec{k}_b = (2\pi)^3 \rho_b(E_b) d\Omega_b dE_b$, where $\rho_b(E_b) = k_b \mu_b/((2\pi)^3\hbar^2)$ is the density of states.[‡] Using this in Eq. (2.18),

$$d\sigma = \frac{(2\pi)^{-2}}{\hbar v_a} \int \delta(E_f - E_i)|T_{fi}|^2 \rho_b(E_b) d\Omega_b dE_b d\vec{k}_x. \tag{2.19}$$

The double differential cross section with respect to the energy and the scattering angle of b is therefore given by

$$\left.\frac{d^2\sigma}{d\Omega_b dE_b}\right|_{\text{EBU}} = \frac{(2\pi)^{-2}}{\hbar v_a} \rho_b(E_b) \int \delta(E_f - E_i)|T_{fi}|^2 d\vec{k}_x, \tag{2.20}$$

which coincides with the result of Austern *et al.* (Eq. (8.15) of Ref.[4]) noting that $\int d\vec{k}_x \to (2\pi)^3 \sum_{\vec{k}_x}$.

We note also that the previous expression can be used to compute the EBU cross section, with respect to the angles and energies of b and x. For that, we use again $d\vec{k}_x = (2\pi)^3 \rho_x(E_x) d\Omega_x dE_x$ and use the energy-conserving delta function, resulting[§]

$$\left.\frac{d^2\sigma}{d\Omega_b dE_b d\Omega_x}\right|_{\text{EBU}} = \frac{2\pi}{\hbar v_a} \rho_b(E_b)\rho_x(E_x)|T_{fi}|^2. \tag{2.21}$$

To obtain the expression for the NEB component we make use of the *coupled-channels optical theorem* recently formulated by Cotanch[30]. This work generalizes the well-known optical theorem to the

[†]Note that the factor $(2\pi)^4$ of Ref.[54] is replaced here by a $(2\pi)^{-5}$ factor, consistent with our definition of the amplitude for the plane waves as $e^{i\vec{k}\vec{r}}$.

[‡]These expressions result from $N(k)d\vec{k}_b = \rho_b(E_b)d\Omega_b dE_b$, where $N(k)$ is the number of states in the differential volume $d\vec{k}_b$, which is determined from $\langle\vec{k}|\vec{k}'\rangle = \delta(\vec{k} - \vec{k}')/N(k)$. In our case, $\langle\vec{k}|\vec{k}\rangle = (2\pi)^3\delta(\vec{k} - \vec{k}')$, and hence $N(k) = (2\pi)^{-3}$.

[§]the partial wave expansion can be found in Appendix B

multichannel case. If χ_i is the channel wave function and W_i the diagonal imaginary part for this channel, the contribution to the absorption in this particular channel is given by[30]

$$\sigma^i_{\rm abs} = -\frac{2}{\hbar v_{el}} \langle \chi_i | W_i | \chi_i \rangle, \tag{2.22}$$

where v_{el} is the projectile–target relative velocity in the incident (elastic) channel.

We may use this result to calculate the NEB contribution by noting that the latter is nothing but the absorption occurring in the $x + A$ channel. The channel wave function is given by $\psi^0_x(\vec{k}_b, \vec{r}_x)$, which is a solution of Eq. (2.12). Since Eq. (2.12) corresponds to a definite energy and direction of the b particle, we consider Eq. (2.22) for a differential cross section corresponding to a range of the outgoing momenta of b,

$$d^2\sigma = -\frac{2}{\hbar v_a} \langle \psi^0_x | W_x | \psi^0_x \rangle \, N(k_b) \, d\vec{k}_b, \tag{2.23}$$

with $W_x \equiv {\rm Im}[U_x]$. Transforming the element of momentum into energy and solid angle elements, we get the double differential cross section

$$\left. \frac{d^2\sigma}{dE_b d\Omega_b} \right|_{\rm NEB} = -\frac{2}{\hbar v_a} \rho_b(E_b) \langle \psi^0_x | W_x | \psi^0_x \rangle. \tag{2.24}$$

This equation is the key result of the IAV model. The same formula was obtained, by different arguments, by Kasano and Ichimura[79]. A similar result was also obtained by Hussein and McVoy[67]. The alternative derivation presented here, based upon the generalized optical theorem, provides a clear interpretation of this formula, as the flux leaving the $x + A$ channel following the breakup of the projectile into b+x.

To recapitulate, in the IAV model, the breakup can be viewed as a two-step process. The first step corresponds to the dissociation of the projectile (a) into the fragments b and x, leaving the target in the ground state. The subsequent motion of the participant particle (x) is described by the function $\psi^0_x(\vec{k}_b, \vec{r}_x)$, which is the solution of the inhomogeneous equation (2.12). This particle can then be scattered elastically by the target or can interact non-elastically (for example, excite the target or fuse with it). The former corresponds to the EBU part of the inclusive breakup cross section whereas these non-elastic processes, corresponding to the second step in this two-step picture, yield the NEB contribution. Quantitatively, this contribution is obtained as the expectation value of ${\rm Im}[U_x]$ in the state $\psi^0_x(\vec{k}_b, \vec{r}_x)$ [Eq.(2.24)]. Note that, since this function depends on the final state of the *spectator* particle (b), the NEB expression (2.24)

yields the absorption for each final state of b.

2.1.2 Practical implementation of the IAV model

The IAV formula for NEB breakup, Eq. (2.24), has a deceptively simple form. The function ψ_x^0 must be first calculated from the inhomogeneous Eq. (2.12), whose source term contains the three-body wave function Ψ^{3b}, which is a complicated object by itself. Furthermore, this equation must be solved for each outgoing energy and angle of b covering the range of interest.

For these reasons, practical implementations of this theory have resorted to additional approximations. Standardly, all these applications rely on the DWBA approximation of the incident channel [that is, Eq. (2.8)], rather than on a three-body model [Eq. (2.9)]. Even at the DWBA level, Eq. (2.12) is not trivial. Usually, a partial wave decomposition of the scattering waves appearing in Eq. (2.12) will be used and this means that a large number of angular momenta for the $a+A$, $x+A$, and $b+B$ distorted waves will be required for convergence of the calculated cross sections. In addition, the right-hand-side of this equation contains non-local kernels, similar to those appearing in DWBA calculations between bound states, but involving a larger number of angular momenta. Consequently, in addition to the DWBA approximation, most of the existing calculations of this kind have been done in the zero-range (ZR) approximation.

One of the goals of our work, will be to assess the validity of these approximations by comparing ZR with finite-range (FR) calculations. These numerical results will be presented in subsequent chapters. In the remainder of this chapter, we will present more detailed formulas for the different approximations and discuss several issues related to their numerical implementation. The detailed formulas for the NEB cross sections in these two approximations are given in the following sections.

2.2 Partial wave expansion of the NEB formula in exact finite range

In this section, we discuss details on how to carry out the numerical calculations. Throughout this work we ignore the spin-orbit interactions by assuming that these interactions are insignificant for the continuum cross section. We introduce the $x-$channel wave function of Eq. (2.12), and its partial expansion as

$$\psi^0_{x;m_{bx}} = \frac{1}{r_x}\sum_{l_x m_x} \psi^0_{l_x m_x;m_{bx}}(r_x,\vec{k}_a,\vec{k}_b)\, Y^{m_x}_{l_x}(\hat{r}_x). \tag{2.25}$$

The radial part $\psi^0_{l_x m_x;m_{bx}}(r_x,\vec{k}_a,\vec{k}_b)$ satisfies the inhomogeneous differential equation given by

$$\left\{\frac{\hbar^2}{2\mu_x}\Big[\frac{\mathrm{d}^2}{\mathrm{d}r_x^2}-\frac{l_x(l_x+1)}{r_x^2}\Big]-U_x+E_x\right\}\psi^0_{l_x m_x;m_{bx}}(r_x,\vec{k}_a,\vec{k}_b)=\rho_{l_x m_x;m_{bx}}(r_x,\vec{k}_a,\vec{k}_b). \tag{2.26}$$

Here $\rho_{l_x m_x;m_{bx}}(r_x,\vec{k}_a,\vec{k}_b)$ is the source term function given as

$$\rho_{l_x m_x;m_{bx}}(r_x,\vec{k}_a,\vec{k}_b)\equiv r_x\Big\langle Y^{m_x}_{l_x}(\hat{r}_x)\chi^{(-)}_b(\vec{r}_b,\vec{k}_b)|V_{\rm post}|\chi^{(+)}_a(\vec{r}_a,\vec{k}_a)\varphi_a(r_{bx})\Big\rangle, \tag{2.27}$$

where $V_{post}=V_{bx}+U_{bA}-U_{bB}$[¶]. In the finite-range approximation, the source term (2.27) is evaluated exactly. Because all the relevant coordinates lie on the same plane (see Fig. 1.3), one can express any coordinate in terms of two independent vectors. So, for example, choosing $\vec{r}_x$ as $\vec{r}_b$ independent vectors, one may write

$$\vec{r}_{bx}=q\vec{r}_x-\vec{r}_b \quad\text{and}\quad \vec{r}_a=(1-pq)\vec{r}_x+p\vec{r}_b, \tag{2.28}$$

where $p=m_b/(m_b+m_x)$ and $q=m_A/(m_A+m_x)$. The projectile wave function, neglecting again its internal spin, can be expressed as $\varphi_a(\vec{r}_{bx})=(R_{l_{bx}}(r_{bx})/r_{bx})Y^{m_{bx}}_{l_{bx}}(\hat{r}_{bx})$. Ignoring the internal spins of the colliding particles, the distorted waves can be expanded as

$$\chi^{(+)}(\vec{k},\vec{r})=\frac{4\pi}{kr}\sum_{lm}i^l R_l(r)Y^m_l(\hat{r})Y^{m*}_l(\hat{k}). \tag{2.29}$$

For charged particles, the radial part is here assumed to include the Coulomb phase, $e^{i\sigma_l}$, where σ_l are the Coulomb phase shifts. Using this, and the partial wave decomposition of the distorted waves, the source term is written as

$$\begin{aligned}\rho_{l_x m_x;m_{bx}}(r_x,\vec{k}_a,\vec{k}_b)=&\frac{16\pi^2}{k_a k_b}r_x\sum_{l_a m_a}\sum_{l_b m_b}i^{l_a+l_b}(-1)^{l_b}Y^{m_b*}_{l_b}(\hat{k}_b)Y^{m_a*}_{l_a}(\hat{k}_a)\int\mathrm{d}\hat{r}_x Y^{m_x*}_{l_x}(\hat{r}_x)\int\mathrm{d}\vec{r}_b V_{\rm post}\\&\times\frac{R_{l_b}(r_b)}{r_b}Y^{m_b}_{l_b}(\hat{r}_b)\frac{R_{l_a}(r_a)}{r_a}Y^{m_a}_{l_a}(\hat{r}_a)\frac{R_{l_{bx}}(r_{bx})}{r_{bx}}Y^{m_{bx}}_{l_{bx}}(\hat{r}_{bx}).\end{aligned} \tag{2.30}$$

To calculate this, we transform the spherical harmonics $Y^{m_a}_{l_a}(\hat{r}_a)$ and $Y^{m_{bx}}_{l_{bx}}(\hat{r}_{bx})$ into linear combinations of the spherical harmonics $Y^{m_b}_{l_b}(\hat{r}_b)$ and $Y^{m_x}_{l_x}(\hat{r}_x)$. This is done by means of Moshinsky solid-harmonic

[¶]Note that in Udagawa and Tamura's formula, $V_{\rm post}\to V_{\rm prior}=U_{xA}+U_{bA}-U_{aA}$

expansion[102]

$$Y_{l_{bx}}^{m_{bx}}(\hat{r}_{bx}) = \sqrt{4\pi}\sum_{n=0}^{l_{bx}}\sum_{\lambda=-n}^{n} c(l_{bx},n)\frac{(qr_x)^{l_{bx}-n}(-r_b)^n}{r_{bx}^{l_{bx}}} Y_{l_{bx}-n}^{m_{bx}-\lambda}(\hat{r}_x) Y_n^{\lambda}(\hat{r}_b)\langle l_{bx}-n, n, m_{bx}-\lambda, \lambda | l_{bx}, m_{bx}\rangle, \tag{2.31}$$

$$Y_{l_a}^{m_a}(\hat{r}_a) = \sqrt{4\pi}\sum_{u=0}^{l_a}\sum_{v=-u}^{u} c(l_a,u)\frac{(pr_b)^{l_a-u}(1-pq)^u(r_x)^u}{r_a^{l_a}} Y_{l_a-u}^{m_a-v}(\hat{r}_b) Y_u^{v}(\hat{r}_x)\langle l_a-u, u, m_a-v, v | l_a, m_a\rangle, \tag{2.32}$$

where

$$c(x,y) = \left(\frac{(2x+1)!}{(2y+1)!(2(x-y)+1)!}\right)^{1/2}. \tag{2.33}$$

Because the interaction $V_{\rm post}$ is an scalar, we can perform the Legendre expansion

$$V_{\rm post}\frac{R_{l_a}(r_a)}{(r_a)^{l_a+1}}\frac{R_{l_{bx}}(r_{bx})}{(r_{bx})^{l_{bx}+1}} = \sum_{T=0}^{T_{max}}(2T+1)\mathbf{q}^T_{l_a,l_{bx}}(r_b,r_x)P_T(z). \tag{2.34}$$

We note that, even if a finite-range treatment is made, in reactions of light projectiles on heavy targets (e.g., deuteron scattering on heavy targets), the difference $U_{bA}-U_{bB}$, known as *remnant term*, can be neglected, and thus $V_{\rm post}\simeq V_{bx}$. The limit T_{max} is chosen large enough to generate all the couplings for partial waves to be used. Here, the argument z in the Legendre polynomials $P_T(z)$ is the cosine of the angle between $\vec{r}_b$ and $\vec{r}_x$. The radial kernels are explicitly given by

$$\mathbf{q}^T_{l_a,l_{bx}}(r_b,r_x) = \frac{1}{2}\int_{-1}^{1} V_{\rm post}\frac{R_{l_a}(r_a)}{(r_a)^{l_a+1}}\frac{R_{l_{bx}}(r_{bx})}{(r_{bx})^{l_{bx}+1}}P_T(z)\mathrm{d}z. \tag{2.35}$$

Finally, the source term results

$$\rho_{l_xm_x;m_{bx}}(r_x,\vec{k}_a,\vec{k}_b) = \frac{16\pi^2}{k_ak_b}\sum_{l_al_b}\sum_{l}\mathfrak{Y}_{l_al_b}^{ll_xm_xm_{bx}}(\hat{k}_a,\hat{k}_b)\rho_{ll_x}^{l_al_b}(r_x), \tag{2.36}$$

with

$$\mathfrak{Y}_{l_al_b}^{ll_xm_xm_{bx}}(\hat{k}_a,\hat{k}_b) = \sum_{m_am_b} Y_{l_a}^{m_a*}(\hat{k}_a)Y_{l_b}^{m_b*}(\hat{k}_b)\langle l_al_{bx}m_am_{bx}|lm_l\rangle\langle ll_bm_lm_b|l_xm_x\rangle, \tag{2.37}$$

and

$$\rho^{l_a l_b}_{l l_x}(r_x) = r_x \sum_{nu} \sum_{\Lambda_a \Lambda_b} \sum_{T} i^{l_a+l_b}(-1)^{l_b+l+n+\Lambda_b-\Lambda_a} p^{l_a-u}(qr_x)^{l_{bx}-n}(r_x)^u (1-pq)^u \widehat{l_a-u}\widehat{l_{bx}-n}\hat{n}\hat{u}$$
$$\times \hat{l}_{bx}\hat{\Lambda}_a\hat{\Lambda}_b\hat{l}_a\hat{l}_b\hat{T}/\hat{l}/\hat{l}_x c(l_{bx},n)c(l_a,u)\langle u, l_{bx}-n, 00|\Lambda_b 0\rangle\langle l_a-u, n, 0, 0|\Lambda_a, 0\rangle$$
$$\times \langle \Lambda_b, T, 0, 0|l_x, 0\rangle\langle \Lambda_a, l_b, 0, 0|T, 0\rangle(2l+1)\begin{Bmatrix} l_{bx} & l & l_a \\ n & \Lambda_a & l_a-u \\ l_{bx}-n & \Lambda_b & u \end{Bmatrix}$$
$$\times W(l_x, \Lambda_b, l_b, \Lambda_a; T, l)\int \mathrm{d}r_b R_{l_b}(r_b)(r_b)^{l_a-u+n+1}\mathbf{q}^T_{l_a,l_{bx}}(r_b, r_x). \tag{2.38}$$

The wave function $\psi^0_{l_x m_x; m_{bx}}(r_x, \vec{k}_a, \vec{k}_b)$ of the inhomogeneous equation (2.26) can be expanded as

$$\psi^0_{l_x m_x; m_{bx}}(r_x, \vec{k}_a, \vec{k}_b) = \frac{16\pi^2}{k_a k_b}\sum_{l_a l_b}\sum_{l} \mathfrak{R}^{l_a l_b}_{l l_x}(r_x)\mathfrak{Y}^{l l_x m_x m_{bx}}_{l_a l_b}(\hat{k}_a, \hat{k}_b), \tag{2.39}$$

where the radial coefficients, $\mathfrak{R}^{l_a l_b}_{l l_x}(r_x)$, are solutions of the inhomogeneous equation

$$\left\{\frac{\hbar^2}{2\mu_x}\Big[\frac{\mathrm{d}^2}{\mathrm{d}r_x^2} - \frac{l_x(l_x+1)}{r_x^2}\Big] - U_x + E_x\right\}\mathfrak{R}^{l_a l_b}_{l l_x}(r_x) = \rho^{l_a l_b}_{l l_x}(r_x). \tag{2.40}$$

For $E_x > 0$ (unbound *x*-*A* states), this equation is to be solved with outgoing boundary conditions

$$\mathfrak{R}^{l_a l_b}_{l_x}(r_x) \to -S^{l_a,l_b}_{l_x} H^{(+)}_{l_x}(k_x r_x), \tag{2.41}$$

where $H^{(+)}_{l_x}(k_x r_x)$ is a Coulomb outgoing wave and the coefficients $S^{l_a,l_b}_{l_x}$ are the S-matrix elements.

Finally, the double differential cross section with finite range within the post-form DWBA can be written as

$$\Big[\frac{\mathrm{d}^2\sigma}{\mathrm{d}\Omega_b \mathrm{d}E_b}\Big]^{\mathrm{NEB}}_{\mathrm{post}} = \frac{64\pi\mu_a\mu_b}{\hbar^4 k_a^3 k_b}\frac{1}{2l_{bx}+1}\sum_{l_x m_x}\sum_{m_{bx}} \mathfrak{I}^{m_{bx}}_{l_x m_x}(\vec{k}_a, \vec{k}_b), \tag{2.42}$$

with

$$\mathfrak{I}^{m_{bx}}_{l_x m_x}(\vec{k}_a, \vec{k}_b) = -\int \mathrm{d}r_x W_x(r_x)\left|\sum_{l_a l_b l}\mathfrak{R}^{l_a l_b}_{l l_x}(r_x)\mathfrak{Y}^{l l_x m_x m_{bx}}_{l_a l_b}(\hat{k}_a, \hat{k}_b)\right|^2. \tag{2.43}$$

The double differential cross calculated in Eq. (2.42) is in c.m. frame. In order to compare the calculated results with the experimental observables, the calculated results need to transform from c.m. frame to lab

frame. The detailed formulas are given in Appendix A.

2.2.1 Special case $l_{bx} = 0$

When the projectile ground state is in a dominant s-wave ($l_{bx} = 0$), such as in the deuteron and ^{6}Li cases, the expressions above are greatly simplified. In this case, the projectile wave function can be expressed as $\varphi_a(\vec{r}_{bx}) = R_{l_{bx}}(r_{bx})/\sqrt{4\pi}/r_{bx}$. Then the source term, Eq. (2.36), can be rewritten as

$$\rho_{l_x m_x;0}(r_x, \vec{k}_a, \vec{k}_b) = \frac{16\pi^2}{k_a k_b} \sum_{l_a l_b} \mathcal{Y}^{l_x m_x}_{l_a l_b}(\hat{k}_a, \hat{k}_b) \rho^{l_a l_b}_{l_x}(r_x), \tag{2.44}$$

with

$$\mathcal{Y}^{l_x m_x}_{l_a l_b}(\hat{k}_a, \hat{k}_b) = \sum_{m_a m_b} Y^{m_a *}_{l_a}(\hat{k}_a) Y^{m_b *}_{l_b}(\hat{k}_b) \langle l_b l_a m_b m_a | l_x m_x \rangle, \tag{2.45}$$

and

$$\begin{aligned} \rho^{l_a l_b}_{l_x}(r_x) =& r_x i^{l_a + l_b} \sum_{uT} (-)^{l_b} c(l_a, u)(1 - pq)^u (r_x)^u \hat{l}_b \widehat{l_a - u} \hat{T} \hat{u} \hat{l}_a / \hat{l}_x \langle l_b, l_a - u, 0, 0 | T, 0 \rangle \\ & \times \langle T, u, 0, 0 | l_x, 0 \rangle W(l_b, l_a - u, l_x, u | T, l_a) \int \mathrm{d}r_b r_b (p r_b)^{l_a - u} R_{l_b}(r_b) q^T_{l_a,0}(r_b, r_x). \end{aligned} \tag{2.46}$$

Similar to Eq. (2.39), the channel wave function $\psi^0_{l_x m_x;0}(r_x, \vec{k}_a, \vec{k}_b)$ in Eq. (2.26) is also expanded in

$$\psi^0_{l_x m_x;0}(r_x, \vec{k}_a, \vec{k}_b) = \frac{16\pi^2}{k_a k_b} \sum_{l_a} \sum_{l_b} \mathfrak{R}^{l_a l_b}_{l_x}(r_x) \mathcal{Y}^{l_a l_b}_{l_x m_x}(\hat{k}_a, \hat{k}_b). \tag{2.47}$$

The radial function $\mathfrak{R}^{l_a l_b}_{l_x}(r_x)$ verifies the inhomogeneous equation

$$\left\{ \frac{\hbar^2}{2\mu_x} \Big[\frac{\mathrm{d}^2}{\mathrm{d}r_x^2} - \frac{l_x(l_x+1)}{r_x^2} \Big] - U_x + E_x \right\} \mathfrak{R}^{l_a l_b}_{l_x}(r_x) = \rho^{l_a l_b}_{l_x}(r_x), \tag{2.48}$$

to be solved with the same boundary condition of Eq. (2.41). Analogous to Eq. (2.42), we obtain the double differential cross section of nonelastic breakup

$$\Big[\frac{\mathrm{d}^2\sigma}{\mathrm{d}\Omega_b \mathrm{d}E_b} \Big]^{\mathrm{NEB}}_{\mathrm{post}} = \frac{64\pi\mu_a\mu_b}{\hbar^4 k_a^3 k_b} \sum_{l_x m_x} \mathfrak{I}_{l_x m_x}(\vec{k}_a, \vec{k}_b), \tag{2.49}$$

where

$$\mathfrak{I}_{l_x m_x}(\vec{k}_a,\vec{k}_b) = -\int \mathrm{d}r_x W_x(r_x)\left|\sum_{l_a}\sum_{l_b}\mathfrak{R}_{l_x}^{l_a l_b}(r_x)\mathfrak{Y}_{l_x m_x}^{l_a l_b}(\hat{k}_a,\hat{k}_b)\right|^2. \tag{2.50}$$

2.3 Partial wave expansion of the NEB formula in zero range

If the remnant term $U_{bA} - U_{bB}$ of the post form interaction in Eq. (2.27) is small, $\varphi_a(\vec{r}_{bx})$ corresponds to an s-wave and V_{bx} is short-ranged, the integral is dominated by the values $r_{bx} \approx 0$ and can be evaluated in the zero-range approximation[119], i.e.,

$$V_{\mathrm{post}}\varphi_a(\vec{r}_{bx}) \simeq V_{bx}(r_{bx})\varphi_a(\vec{r}_{bx}) \simeq D_0\delta(\vec{r}_{bx}), \tag{2.51}$$

where D_0 is the *zero-range constant*. Using this approximation in (2.27), the source term results

$$\rho_{l_x m_x;0}(r_x,\vec{k}_a,\vec{k}_b) = \frac{16\pi^2}{k_a k_b}\sum_{l_a}\sum_{l_b}\rho_{l_x}^{l_a l_b}(r_x)\mathfrak{Y}_{l_x m_x}^{l_a l_b}(\hat{k}_a,\hat{k}_b) \tag{2.52}$$

with

$$\rho_{l_x}^{l_a l_b}(r_x) = \frac{D_0}{c r_x} i^{l_a+l_b}(-1)^{l_b}\Big[\frac{(2l_a+1)(2l_b+1)}{4\pi(2l_x+1)}\Big]^{1/2}\langle l_a l_b 00|l_x 0\rangle R_{l_a}(r_x)R_{l_b}(c r_x)\Lambda(r_x) \tag{2.53}$$

and

$$\mathfrak{Y}_{l_x m_x}^{l_a l_b}(\hat{k}_a,\hat{k}_b) = \sum_{m_a m_b}\langle l_a l_b m_a m_b|l_x m_x\rangle Y_{l_b}^{m_b *}(\hat{k}_b)Y_{l_a}^{m_a *}(\hat{k}_a), \tag{2.54}$$

where $c = m_A/(m_A+m_x)$ and $\Lambda(r_x)$ is the *finite-range correction factor* (see details in the Appendix C).

Following the partial wave expansion of Eq. (2.47), the double differential cross section of nonelastic breakup with zero-range approximation results

$$\Big[\frac{\mathrm{d}^2\sigma}{\mathrm{d}\Omega_b \mathrm{d}E_b}\Big]_{\mathrm{post}}^{\mathrm{NEB}} = \frac{64\pi\mu_a\mu_b}{\hbar^4 k_a^3 k_b}\sum_{l_x m_x}\mathfrak{I}_{l_x m_x}(\vec{k}_a,\vec{k}_b), \tag{2.55}$$

where

$$\mathfrak{I}_{l_x m_x}(\vec{k}_a,\vec{k}_b) = -\int \mathrm{d}r_x W_x(r_x)\left|\sum_{l_a}\sum_{l_b}\mathfrak{R}_{l_x}^{l_a l_b}(r_x)\mathfrak{Y}_{l_x m_x}^{l_a l_b}(\hat{k}_a,\hat{k}_b)\right|^2. \tag{2.56}$$

2.4 Convergence of the post-form amplitude

Another difficulty arising in solving Eq. (2.12) are the well-known convergence problems of the post-form DWBA formula when applied to breakup reactions. This is because $\chi_b^{(-)}$, being a scattering state, will be infinitely oscillatory and the operator in the matrix element V_{bx} and the initial state (ψ_a in DWBA) depend on the $\vec{r}_{bx}$ coordinate and hence there is no natural cutoff in the $\vec{r}_b$ integration. As a consequence, the source term has infinite range. To overcome this problem, several solutions have been proposed in the literature. We discuss some of these solutions, which will be later used and compared in our calculations:

(i) The damping factor method proposed by Huby and Mines[64] and Vincent[139]. In this method the source term is multiplied by an exponential convergence factor, which damps the contribution of the integral at large distances, i.e., the source term of Eq. (2.12) can be interpreted as

$$\rho(\vec{k}_b, \vec{r}_x) \equiv \lim_{\alpha \to 0^+} \rho^{(\alpha)}(\vec{k}_b, \vec{r}_x), \tag{2.57}$$

with

$$\rho^{(\alpha)} = e^{-\alpha r_x} \rho(\vec{k}_b, \vec{r}_x). \tag{2.58}$$

It can be demonstrated that by using the damping α, the left-hand side (LHS) of Eq. (2.57) oscillates with zero mean at large r_x.

(ii) The binning method. In this method, the scattering states are first expanded in partial waves (see Sec 2.2), and the radial coefficients, $R_{\ell_b}(r_b, k_b)$ are then averaged over small energy or momentum intervals, i.e.,

$$\bar{R}_{\ell_b}(r_b, k_b^i) = N \int_{k_b^i - \Delta k_b/2}^{k_b^i + \Delta k_b/2} dk_b \, R_{\ell_b}(r_b, k_b), \tag{2.59}$$

where Δk_b is the bin width, k_b^i the central momentum of the bin and N is a normalization constant. The resulting bin wave function is square-integrable and thus leads to convergent results when used in the source term of Eq. (2.12).

(iii) The complex-integration by Vincent and Fortune[140]. They suggest using the actual scattering wave function, but choosing an integration contour along the complex plane in such a way that the oscillatory integrand is transformed into an exponential decay, thus improving the convergence and numerical stability of the calculation.

2.5 Extension of IAV model to $E_x < 0$

The sort of breakup cross section that considered by Ichimura, Austern and Vincent can be regarded as transfer to continuum ($E_x > 0$). In general, the inclusive cross section will contain also contributions coming from $E_x < 0$. For example, in a (d, pX) reaction, the prottons emitted at the higher energies will actually correspond to neutron transfer to bound states of the target nucleus. One would like to have one framework to describe both transfer to continuum state and as well as to bound states ($E_x < 0$). The explicit inclusion of all possible final bound states is unpractical because of the large number of final states and the undertaintities in their spin/parity assignments and spectroscopic factors. An alternative procedure was proposed by Udagawa and Tamura, as presented here. The key idea is to extend the complex potential to negative energies. Then, the bound states of the system are simulated by the eigenstates in this complex potential. The imaginary part will be associated with the spreading width of the single-particle states, which accounts for the fragmentation of these states into more complicated configurations due to the residual interactions. The formalism is greatly simplified if one assumes a constant imaginary part, i.e.:

$$W_x = -\Gamma/2. \tag{2.60}$$

The inhomogeneous equation Eq. (2.40) can be rewritten as

$$(H_x - E_x)\mathfrak{R}^{l_a l_b}_{l l_x}(r_x) = r_x \rho^{l_a l_b}_{l l_x}(r_x), \tag{2.61}$$

with

$$H_x = -\frac{\hbar^2}{2\mu_x}\Big[\frac{\mathrm{d}^2}{\mathrm{d}r_x^2} - \frac{l_x(l_x+1)}{r_x^2}\Big] + U_x. \tag{2.62}$$

H^0_x is the Hamiltonian H_x (defined in Eq. 2.62), when W_x is set zero in the latter. Then there is a set of (real) eigen-solutions ψ_i of this new Hamiltonian H^0_x:

$$(H^0_x - E_i)\psi_i = 0. \tag{2.63}$$

H^0 can be regarded as the radial single-particle Hamiltonian, and ψ_i and E_i as the corresponding single-particle wave functions and energies, respectively.

Under this assumption (W_x is constant), ψ_i also satisfies

$$(H_x - \tilde{E}_i)\psi_i = 0, \tag{2.64}$$

with

$$\tilde{E}_i = E_i - i\Gamma/2. \tag{2.65}$$

Namely, ψ_i is an eigenfunction of the complex Hamiltonian H_x with the complex eigenvalue $\tilde{E}_i$. The imaginary part Γ then describes the spreading (decaying) width of the eigenstate i[95].

In terms of ψ_i, one can expand $\mathfrak{R}^{l_a l_b}_{l l_x}$ as

$$\mathfrak{R}^{l_a l_b}_{l l_x} = \sum_i \frac{1}{E_x - E_i + i\Gamma/2} |\psi_i\rangle\langle\psi_i| r_x \rho^{l_a l_b}_{l l_x}\rangle. \tag{2.66}$$

Note that the sum over i is over the complete set of states i, which includes not only the discrete (bound) states, but also the continuum states with $E_x > 0$. Therefore, $\mathfrak{R}^{l_a l_b}_{l l_x}$ given by Eq. (2.66) includes continuum effects.

By using Eq. (2.66), the matrix element in Eq. (2.24) can be written as

$$\langle \mathfrak{R}^{l_a l_b}_{l l_x} | W_x | \mathfrak{R}^{l_a l_b}_{l l_x}\rangle = \sum_i \frac{\langle\psi_i|W_x|\psi_x\rangle}{(E-E_i)^2 + \Gamma^2/4} |\langle\psi_i| r_x \rho^{l_a l_b}_{l l_x}\rangle|^2. \tag{2.67}$$

Finally obtained

$$\Big[\frac{\mathrm{d}^2\sigma}{\mathrm{d}\Omega_b \mathrm{d}E_b}\Big]^{E_x<0}_{\text{post}} = \frac{64\pi\mu_a\mu_b}{\hbar^4 k_a^3 k_b} \frac{1}{2l_{bx}+1} \sum_i \frac{\Gamma}{2(E-E_i)^2 + \Gamma^2/2} \frac{\mathrm{d}\sigma_{l_x}}{\mathrm{d}\Omega_b}, \tag{2.68}$$

with

$$\frac{\mathrm{d}\sigma_{l_x}}{\mathrm{d}\Omega_b} = \Big| \sum_{l_a l_b l} \sum_{m_{bx} m_x} \Big\langle \psi_i | r_x \rho^{l_a l_b}_{l l_x} \mathfrak{Y}^{l l_x m_x m_{bx}}_{l_a l_b}(\hat{k}_a, \hat{k}_b) \Big\rangle \Big|^2. \tag{2.69}$$

The single-differential cross section given by Eq. (2.69) is nothing but the usual DWBA cross section of the transfer reaction, in which x is captured into a single-particle state i. It is thus seen that the double-differential cross section of Eq. (2.68) is, in fact, an energy average of the DWBA cross section of Eq. (2.69) with appropriate weight functions.

In this Chapter, we have reviewed the model purposed by IAV and discussed the partial wave expansion

of that model. In the following Chapters, we will investigate the application of IAV model.

I learned very early the difference between knowing the name of something and knowing something.

Richard Feynman

3 Applications

This chapter will present the calculations for several reactions induced by deuterons, ^{6}Li, ^{11}Be, ^{7}Li, ^{7}Be and ^{8}B projectiles and compare the calculated inclusive cross sections with experimental data to assess the validity of the theory. In all cases, the contributions for the elastic (EBU) and nonelastic (NEB) breakup cross sections are computed separately. The EBU cross sections are calculated with the CDCC formalism[4], using the coupled-channels code FRESCO[128]. This makes it possible to treat the EBU to all orders. For some cases, the CDCC and DWBA formalisms for EBU are compared. The NEB cross sections are calculated with the DWBA version of the IAV model, given by Eq. (2.24) and the accuracy of the Zero-Range approximation is tested by comparing zero range with finite range calculations.

3.1 Calculations for (d, pX)

There is a large body of exclusive and inclusive breakup data for deuteron-induced reactions. We have considered the inclusive (d, pX) data for the reactions d+^{93}Nb at $E_d = 25.2$ MeV from Ref.[108], and d+^{58}Ni at 80 and 100 MeV from Refs.[142,115].

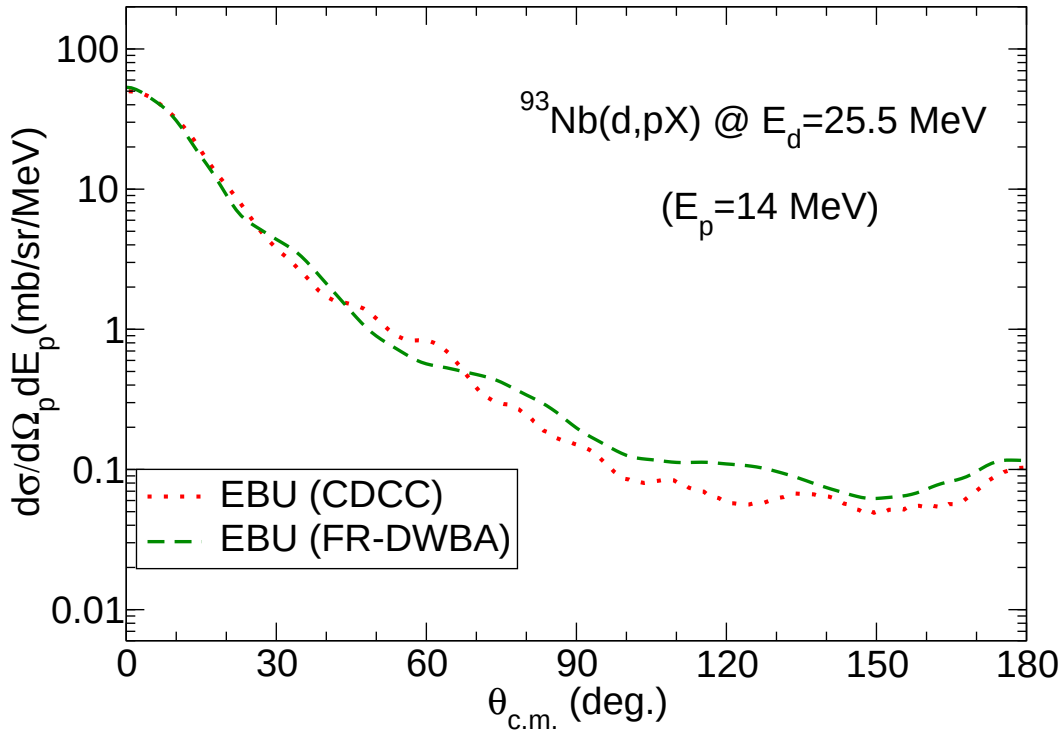

Figure 3.1: Calculated double differential cross section, as a function of the proton scattering angle, for the protons emitted in the ^{93}Nb(d,pX) reaction with an energy of 14 MeV, and a deuteron incident energy of $E_d = 25.5$ MeV. The dotted and dashed lines are the elastic breakup angular distributions calculated with CDCC and DWBA, respectively.

3.1.1 d+^{93}Nb

The data for d+^{93}Nb were already analyzed in Ref.[108], using the so-called surface approximation, in Ref.[79], using the zero-range version of the post-form DWBA formula discussed here, and in Ref.[112], using the prior form of the DWBA IAV model. These calculations give a reasonable account of the experimental data.

In our calculations, the elastic breakup cross sections have been obtained with the CDCC method[4]. In the CDCC formalism the deuteron breakup is treated as inelastic excitations to the p-n continuum. This continuum is truncated at a maximum excitation energy, and discretized in energy bins. For the present case, the p-n states were included for $\ell = 0 - 4$ partial waves, and up to a maximum excitation energy of 20 MeV. For the p-n interaction, the simple Gaussian form of Ref.[4] was considered. The proton-target and neutron-target interactions were adopted from the global parametrization of Koning and Delaroche (KD)[88], omitting the spin-orbit term, and evaluated at half of the deuteron incident energy. In the CDCC

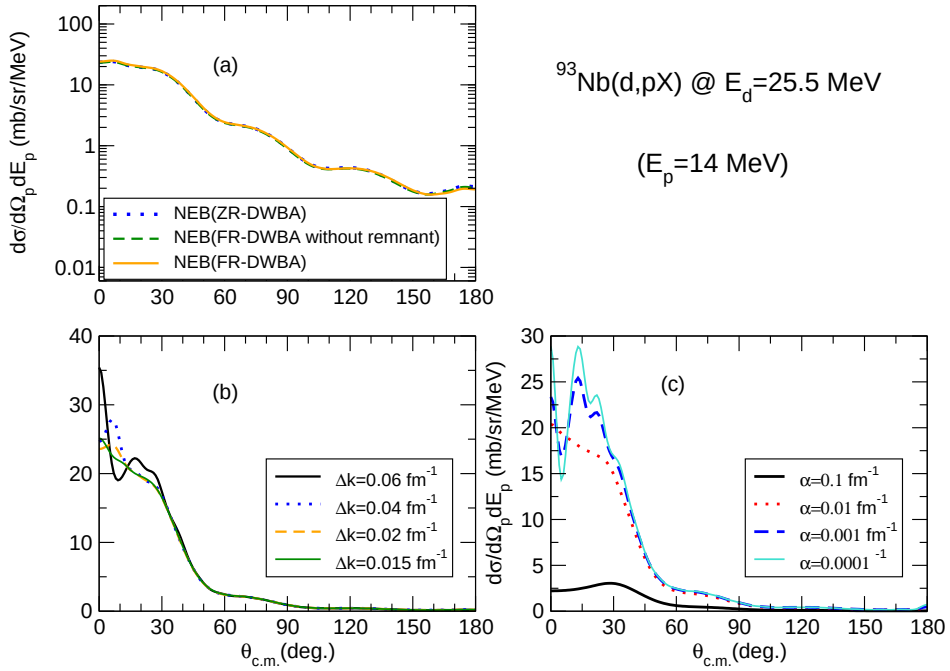

Figure 3.2: Calculated double differential cross section, as a function of the proton scattering angle, for the protons emitted in the ^{93}Nb(d, pX) reaction with an energy of 14 MeV, and a deuteron incident energy of $E_d = 25.5$ MeV. (a) Non-elastic breakup angular distribution calculated with ZR-DWBA (dotted line), FR-DWBA without remnant (dashed line) and full FR-DWBA (solid line); (b) Convergence of the NEB calculation with respect to the bin width, Δk_b, used for the b distorted waves; (c) Convergence of the NEB calculation with respect to the value of damping factor, α, used for the b distorted waves. See text for details.

method, the breakup cross sections are calculated in terms of the center of mass (c.m.) scattering angle and excitation energy of the p-n system. Therefore, to compare with the proton inclusive data, these breakup cross sections must be converted to the proton energy and scattering angle, making use of the appropriate kinematical transformation. This was done with the formalism and codes developed in Ref.[131]. Fig. 3.1 shows the elastic breakup angular distribution , for the protons emitted in the ^{93}Nb$(d,p$X) reaction with an energy of 14 MeV, and a deuteron incident energy of $E_d = 25.5$ MeV, with the CDCC method (dotted line) discussed above. For comparison we also show the EBU calculation obtained with DWBA post-form formalism. For this DWBA calculation, we used the exact finite-range treatment and included the full remnant term. The KD parameterization was also used for the proton-target and neutron-target interactions, but evaluated at the corresponding proton (E_p) and neutron (E_n) energies. In DWBA, one needs also the incoming channel optical potential (d+^{93}Nb), which was taken from Ref.[2]. It can been seen that the DWBA calculation (dashed line) is close to the CDCC calculation (dotted line) indicating

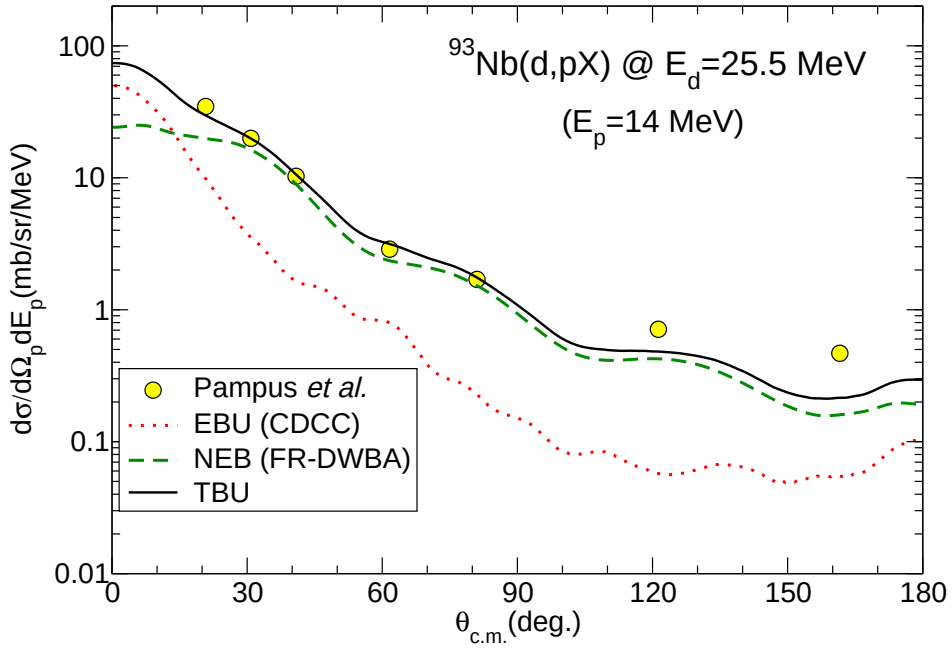

Figure 3.3: Experimental and calculated double differential cross section, as a function of the proton scattering angle, for the protons emitted in the ^{93}Nb(d,pX) reaction with an energy of 14 MeV, and a deuteron incident energy of $E_d = 25.5$ MeV. The dotted, dashed and solid lines are the elastic breakup (CDCC), the non-elastic breakup (FR-DWBA) and their incoherent sum, respectively. Experimental data are taken from Ref.[108].

that the former is accurate in this particular case.

For the NEB calculations, we have performed calculations using different approxiations, namely,(i) a exact finite-range calculation, including the full remant term, (ii) a finite-range calculation without remnant term and (iii) a zero-range calculation. For the ZR-DWBA calculations the zero-range constant $D_0 = 125$ MeV $\cdot$ fm$^{3/2}$ was used, and we included the finite-range correction factor (see, e.g., Refs.[18,119] and Section 2.3).

Fig. 3.2(a) shows double differential NEB cross section, comparing the results obtained with the different approximations. The dotted line is the ZR-DWBA calculation with the finite range correction factor $\Lambda(r_x)$ (see Sec. 2.3). The dashed line is the FR-DWBA calculation, omitting the remnant term in the transition operator (i.e., using $V_{\rm post} \approx V_{pn}$). Finally, the solid line is the full FR-DWBA calculation.

It can be seen that the ZR calculation (with finite-range correction) provides a very accurate result in the present reaction, thus supporting the validity of this approximation in this case. Further, the non-remnant term has a very small effect, and can be also safely ignored in the calculation.

In order to obtain meaningful results, the calculated observables must converge as the bin width Δk_b is progressively decreased [c.f. Eq. (2.59)]. This is verified in Fig. 3.2(b) for the present case, where the calculated NEB angular distribution for different values of Δk_b are shown. Although the rate of convergence was found to be slow, it is seen that for $\Delta k_b \approx 0.02$ fm^{-1} the calculations are well converged for the full angular range.

As discussed in Sec. 2.4, other approaches have been proposed to overcome the slow convergence of the breakup post-form calculations. One of these methods is the introduction of an exponential damping factor in the source term, i.e., $\exp(-\alpha r)$, and study the convergence of the of the calculated observables as $\alpha \to 0$. This convergence study is illustrated in Fig. 3.2 (c) for the present case. It is seen that for $\alpha \approx 0.001$ fm^{-1} the calculations are well converged. Moreover, the converged result is in good agreement with that found using the binning procedure. Convergence was found to be somewhat faster for the binning procedure so, unless stated otherwise, this method was adopted for the subsequent calculations presented below. In each, a convergence study with respect to the bin size was done, but only the converged results are presented.

In Fig. 3.3, the experimental [108] and calculated inclusive double differential cross section, $\mathrm{d}^2\sigma/\mathrm{d}E_p\mathrm{d}\Omega_p$, corresponding to a proton energy of $E_p = 14$ MeV are compared. The dotted line is the EBU calculation (CDCC), which is found to underestimate the data at all angles. The dashed line is the exact FR-DWBA calculation for the NEB part (see Section 2.2). The solid line is the sum of the EBU and NEB contributions. Except at very large angles, it is found to explain satisfactorily the data. It it to be noted that, at the largest angles, the cross section is very small and other sources of protons (such as those produced in fusion + evaporation) might also contribute. It is seen that, except for the smallest angles, the inclusive breakup cross section is largely dominated by the NEB contribution. Our results are consistent with those reported in Refs. [108] and [79].

3.1.2 d+^{62}Ni

Now the results of d+^{62}Ni reaction at 25.5 MeV are presented. The experimental data [86,97] for (d,pX) were analysed by Mastroleo *et. al* [97] using the Udagawa-Tamura's prior form and they found that their

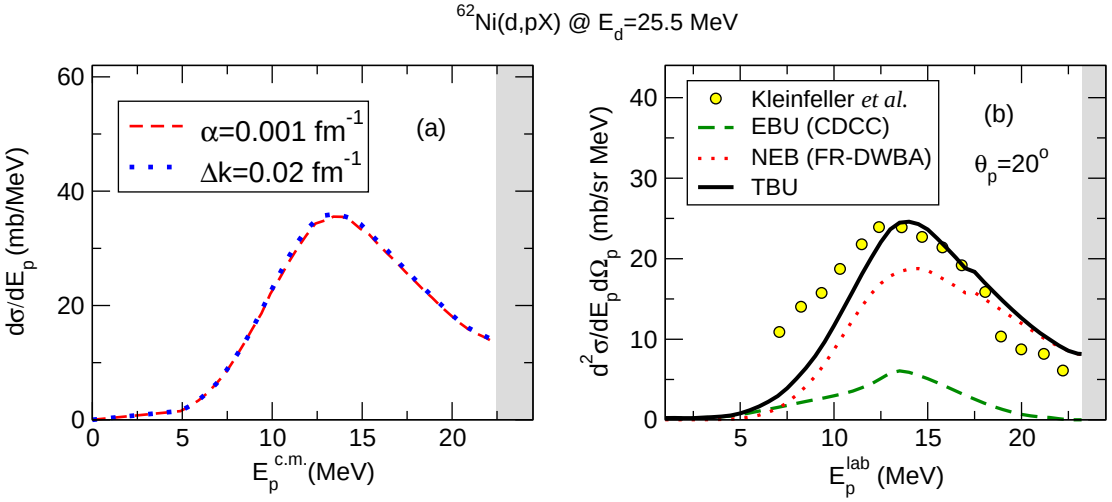

Figure 3.4: (a) Convergence of nonelastic breakup calculations with respect to bin width in fm^{-1} (dotted line) and damping factor (dashed line) used for the b distorted waves, as a function of the outgoing proton emitting energy, and a deuteron incident energy of $E_d = 25.5$ MeV; (b) Double differential cross section as a function of the proton energy in the laboratory frame, for $\theta_p = 20^\circ$. The dashed, dotted, and solid lines are the elastic breakup (CDCC), the non-elastic breakup (FR-DWBA) and their incoherent sum, respectively. The experimental data are taken from Refs.[86,97].

calculations successfully reproduced these data, whereas the calculations using the IAV model largely over-predicted them. We reexamine these results using the CDCC method for the EBU part and our implementation of the IAV model for the NEB part. In the CDCC calculation, we employ the same proton-target and neutron-target interactions as used in Ref.[97]. We keep the same $p + n$ interaction as for the d+^{93}Nb case. For the p-n continuum we considered the partial waves $\ell = 0 - 6$, and excitation energies up to 20 MeV. For the NEB part, we use the same potential as in Ref.[97].

Before comparing with the data, we compare the NEB results obtained with the two stabilization methods discussed above, namely, the binning method and the damping method. The converged (i.e. stabilized) results obtained with these two methods are displayed in Fig. 3.4(a) for the angle-integrated NEB cross section as a function of the proton energy in the CM frame. The shaded region corresponds to negative energies of the neutron, that is, transfer to bound states. In Fig. 3.4(a), the dashed line shows the calculation result using the damping factor method with $\alpha = 0.001$ fm^{-1} which gives almost identical result as bin method with the bin size, $\Delta k = 0.02$ fm^{-1}. In both cases, with the choice of the value of the factors, i.e.,α, Δk, the calculations are converged.

In Fig. 3.4(b) the calculated cross sections are compared with the experimental data from Refs.[86,97], corresponding to the double differential cross section as a function of the proton energy and a proton

detection angle of $\theta_p = 20^\circ$ in the laboratory frame. Note that, in this experiment, compound-nucleus contributions were estimated and subtracted so the data should mainly correspond to the direct breakup modes considered here. It is seen that the sum of them, EBU + NEB, reproduces reasonably well the magnitude and shape of the data, except for some underestimation at the smaller energies and some overestimation at the larger ones. Note that the low-energy tail will be mostly affected by the compound-nucleus subtraction and hence some uncertainty is expected at these energies. The results shown here are at variance with those reported in Ref.[97], who found an overestimation of the IAV model. A more detailed comparison between the IAV and UT models is deferred to Chapter 4.

3.1.3 d+^{58}Ni

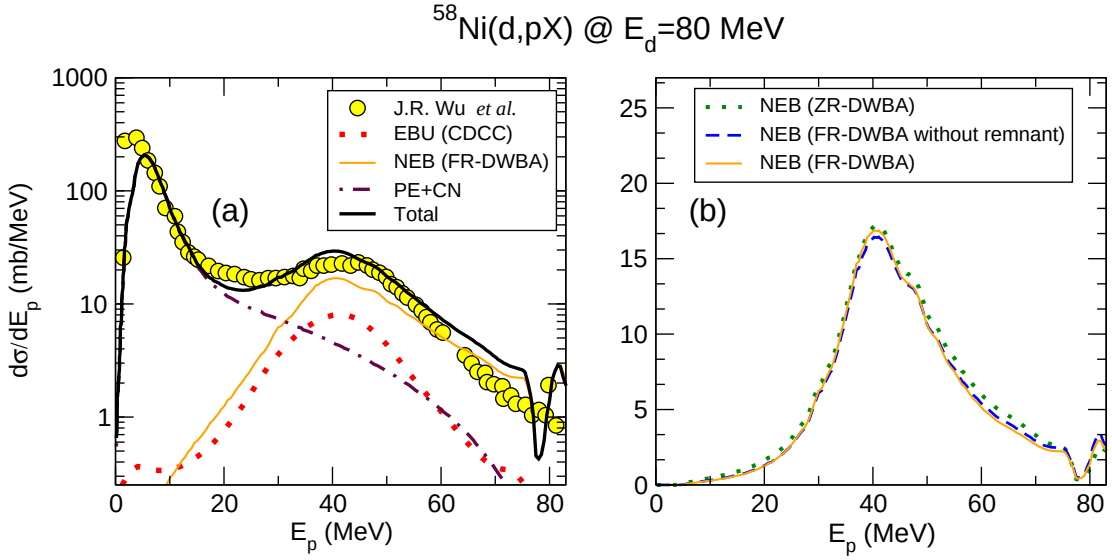

Figure 3.5: (a) Experimental and calculated angle-integrated proton differential cross section, as a function of the outgoing proton energy in the LAB frame, for the ^{58}Ni(d,pX) reaction at $E_d = 80$ MeV. The dotted and thin solid lines are the EBU and NEB contributions, calculated with CDCC and FR-DWBA, respectively. The dot-dashed line is the contribution coming from pre-equilibrium and compound nucleus[75]. The thick solid line is the incoherent sum of the three contributions. Experimental data are from Ref.[142]. (b) Non-elastic breakup calculated with ZR-DWBA (dotted), non-remnant FR-DWBA (dashed), and full FR-DWBA (solid) formulas.

Now the results for the ^{58}Ni(d,pX) reaction at 80 and 100 MeV are presented and compared with the data from Refs.[142,115]. These data have been also analyzed in Refs.[144,75,105], using the CDCC method for the EBU part, and the semi-classical Glauber approach for the NEB part. In the CDCC calculations, the proton-target and neutron-target interactions are obtained again from the Koning-Delaroche parametriza-

tion, and employed the same *p-n* interaction used before. For the *p-n* continuum we considered the partial waves $\ell = 0 - 6$, and excitation energies up to 50 MeV and 90 MeV for the data at $E_d = 80$ MeV and $E_d = 100$ MeV, respectively. For the NEB calculations, the d+^{58}Ni potential was taken from Ref.[2].

In Fig. 3.5, the angle-integrated energy differential cross section at E_d=80 MeV ($d\sigma/dE_p$) is presented. In Fig. 3.5(a), the dotted and thin solid lines correspond to the EBU (CDCC) and NEB (FR-DWBA) calculations. It is seen that the NEB contribution is much larger than the EBU part. Both distributions show a bell-shaped behavior, with a maximum around half of the deuteron energy. However, it is observed that the sum of these two contributions cannot explain the experimental yield at small proton energies. As shown in Ref.[75], these low-energy protons come mainly from compound nucleus followed by evaporation and from pre-equilibrium. Since these processes are not accounted for by the present formalism, in this work the estimate done in Ref.[75] was adopted (dot-dashed line in Fig. 3.5(a)). The total inclusive cross section, including this contribution (thick solid line) reproduces reasonably well the shape and magnitude of the data. Note that protons with energies larger than ∼74 MeV correspond to bound states of the neutron-target system and are therefore associated with a stripping mechanism. This contribution can be accommodated in the present formalism solving Eq. (2.12) for $E_x < 0$ and with boundary conditions appropriate for bound states instead of outgoing boundary conditions. Further, for high-lying bound excited states, were the density of levels will be very high, one may use the ideas of Udagawa and co-workers of extending the complex potential to negative energies to describe the spreading of single-particle states[133,134] (See details in Sec. 2.5). We consider the neutron single-particle states of ^{59}Ni as $1g_{9/2}$ ($E_x = -5.796$ MeV), $2d_{5/2}$ ($E_x = -3.911$ MeV), $3s_{1/2}$ ($E_x = -3.537$ MeV) where the energies correspond to the experimentally extracted centroids for these configurations [73][74] with the spreading width $\Gamma = 2$ MeV. Since our formalism ignores the spin-orbit interaction of the neutron-target potential, for each configuration the depth of this potential was adjusted to yield the corresponding separation separation energy. We note that, when the energy close to the threshold ($E_p \sim 74$ MeV), the numerical results are unreliable due to the difficultly of calculating the wave function of $n-^{58}$Ni system for $E_n \sim 0$. As a result, the nonelastic breakup differential cross section plotted in Fig. 3.5 exhibits a dip at $E_p = 74$ MeV which does not seem to be supported by the smoother trend of the experimental data. A proper understanding of this near-threshold behaviour and of its correct numerical treatment, while interesting, goes beyond the scope of this work and is left for future investigations.

In Fig. 3.5(b), the different approximations for the transition amplitude used in the NEB calculation

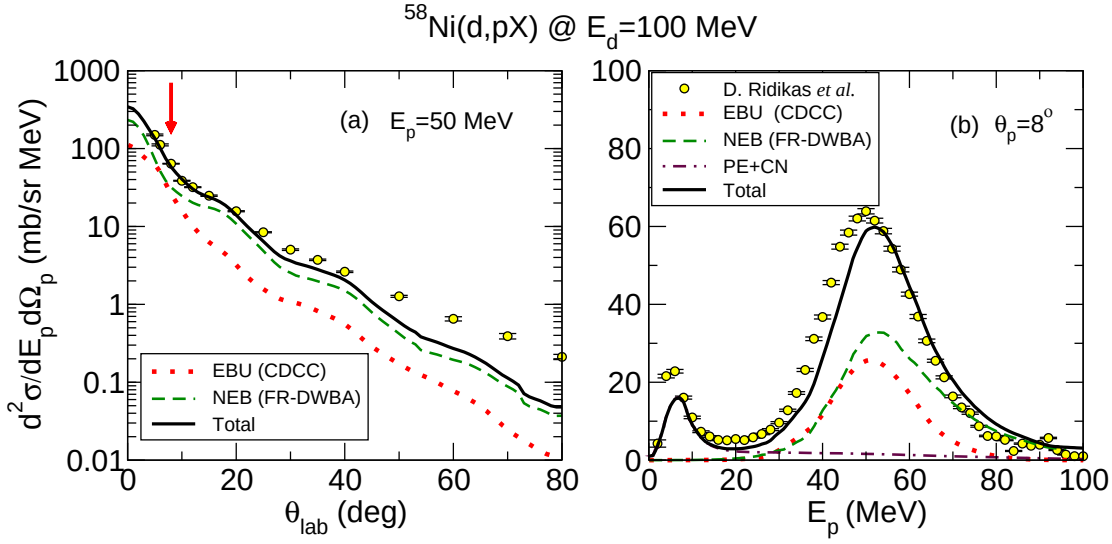

Figure 3.6: Double differential cross section of protons emitted in the ^{58}Ni(d,pX) reaction at $E_d = 100$ MeV in the laboratory frame. (a) Proton angular distribution for a fixed proton energy of $E_p = 50$ MeV. (b) Energy distribution for protons emitted at a laboratory angle of 8° (arrow in top figure). The meaning of the lines is the same as in Fig. 3.5, and are also indicated by the labels. Experimental data are from Ref.[115].

are compared, namely, zero-range DWBA (dotted), finite-range DWBA with no remnant (dashed) and full finite-range DWBA (solid). As in the previous case, the ZR-DWBA and FR-DWBA calculations agree very well for proton energies around and above the maximum, although some small differences are visible. The effect of the remnant term is again found to be very small.

Finally the results for the d+^{58}Ni reaction at 100 MeV are presented. The results are shown in Fig. 3.6, where the top panel contains the experimental and calculated proton angular distributions for protons detected at 50 MeV in the laboratory frame, and the bottom panel shows the energy distribution for the protons scattered at 8° in the laboratory frame. Again, it is seen that the inclusive breakup is dominated by the NEB contribution in the full angular range, particularly at large scattering angles. As in the 80 MeV case, both the EBU and NEB contributions exhibit bell-shaped distributions, with a maximum around $\approx E_d/2$. On the other hand, the protons coming from compound nucleus and pre-equilibrium dominate the low-energy region. Except for some underestimation of the cross section at the maximum, the agreement between the theory and the data is rather satisfactory.

3.2 (^{6}Li, αX)

We have seen that the IAV model provide a suitable description of inclusive breakup reaction induced by deuterons. As a second example, we consider now the case of ^{6}Li induced reactions, for which a large body of experimental data exist. Invariably, these data show a remarkably large yield of α particles. The understanding of the large α yields observed in reactions with ^{6}Li has been subject of many studies [110,28,83,107,19,124,89,117,113]. These works have shown (see e.g. Refs. [89,19]) that the total exclusive cross sections (α+d and α+p) are much smaller than the total α production cross section. Consequently, the α inclusive cross sections are largely underestimated by CDCC calculations which, as we have seen, account only for the EBU part. Here, we apply the IAV to calculation of the total inclusive cross sections of ^{6}Li induced reaction.

3.2.1 ^{209}Bi (^{6}Li, αX)

We first consider the ^{6}Li+^{209}Bi reaction at several bombarding energies between 24 and 50 MeV, for which experimental data exist [117]. The nominal Coulomb barrier for this system is around 30.1 MeV [31], so these data span energies below and above the barrier. The ^{6}Li nucleus is treated in a two-cluster model (α+d). CDCC calculations based on this model have been performed for many ^{6}Li induced reactions. In order to reproduce the elastic data, these calculations usually require a reduction of the imaginary part of the fragment-target interactions [63,11,116]. On the other hand, four-body CDCC calculations, based on a more realistic three-body model of ^{6}Li (α+p+n), are able to describe the elastic data for ^{6}Li+^{209}Bi without any readjustment of these potentials [141], thus suggesting that the need for a reduced absorption is related to the limitations of this two-body model for ^{6}Li. Since the inclusive formulas considered in this work are based on a two-body model of the projectile, the calculations are performed with the α+d model, and allow for the same kind of renormalization prescribed in previous works.

For that, first the elastic scattering within the CDCC framework is studied. These calculations include s-wave ($J^\pi = 1^+$), p-wave ($J^\pi = 0^-,\ 1^-,\ 2^-$), and d-wave ($J^\pi = 1^+,\ 2^+,\ 3^+$) continuum states. For the d wave, a finer division of bins is made in order to describe the ^{6}Li resonant states at 2.186 MeV ($J^\pi = 3^+$), 4.31 MeV ($J^\pi = 2^+$) and 5.7 MeV ($J^\pi = 1^+$). For the $\alpha + d$ ground state, a Woods-Saxon well is used with $V_0 = 78.46$ MeV, $r_0 = 1.15$ fm, and $a = 0.7$ fm [106]. A second Woods-Saxon well is used to describe the $p-$ and $d-$wave states with parameters $V_0 = 80.0$ MeV, $r_0 = 1.15$ fm, $a = 0.7$ fm

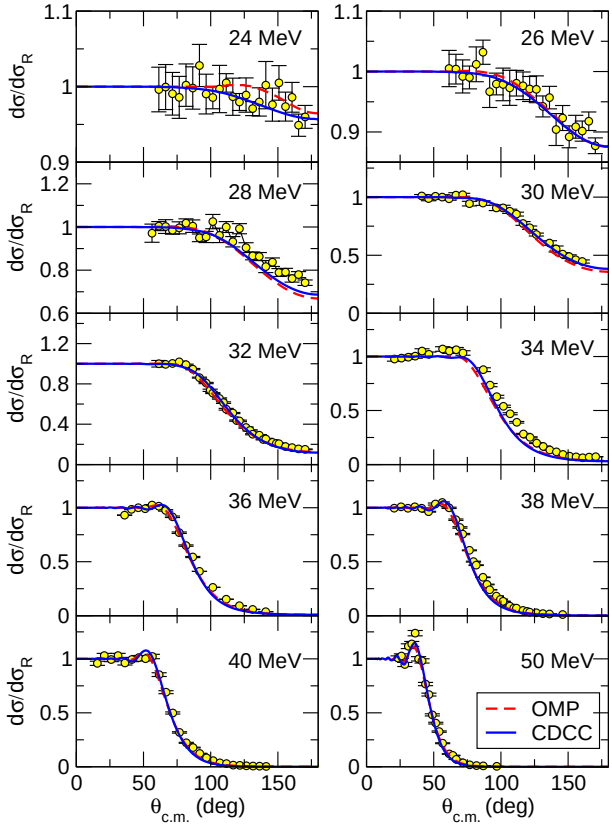

Figure 3.7: Elastic scattering of ^{6}Li+^{209}Bi at different incident energies. The solid and dashed lines are, respectively, the CDCC calculation and the optical model calculation with the optical potential from [29]. The experimental data are from Ref. [118] .

and supplemented with a spin-orbit term, with the usual Woods-Saxon derivative form, and parameters $V_{so} = 2.5$ MeV, $r_{so} = 1.15$ fm, $a_{so} = 0.7$ fm in order to place the $d-$wave resonances correctly. The $d-^{209}$Bi and $\alpha-^{209}$Bi optical potentials are taken from Refs.[57] and[6], respectively. Consistently with previous works, these calculations were found to underestimate the elastic data. It was found that, by removing the surface part of the $d-^{209}$Bi imaginary potential, a good description of the experimental elastic angular distributions is achieved. This is shown in Fig. 3.7 by solid lines. For comparison, the optical model calculation using the potential of Cook[29] (dashed lines) is also shown. Note that this reduction of the imaginary potential is consistent with the conclusions of Ref. [141], which points toward an effective suppression of the deuteron breakup in ^{6}Li scattering, compared to the free deuteron scattering.

Now the inclusive breakup cross sections (^{6}Li,αX) are discussed. The EBU contribution was obtained from the CDCC calculations discussed above. For the NEB calculations, we used Eq. (2.24), both in

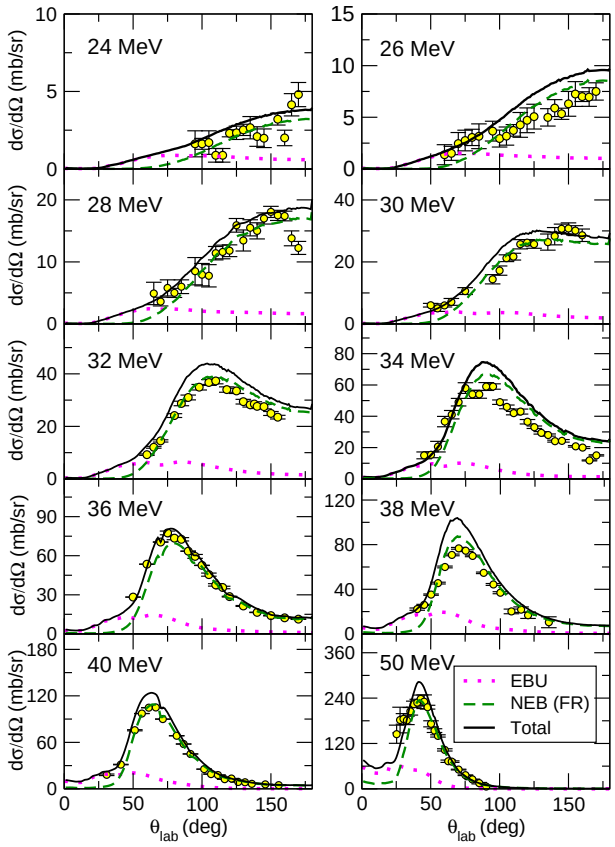

Figure 3.8: Angular distribution of α particles produced in the reaction ^{6}Li+^{209}Bi at the incident energies indicated by the labels. The dotted, dashed and solid lines correspond to the EBU (CDCC), NEB (FR-DWBA) and their sum, respectively. Experimental data are from Ref. [117].

the ZR and FR-DWBA approximations. The same optical potentials for α/d+^{209}Bi were used as in the CDCC calculations. For simplicity, the deuteron and target spins are ignored (note that, in the CDCC calculations, the inclusion of the deuteron spin is important to place correctly the $\ell = 2$ resonances). The distorted waves for the incoming channel are calculated with the optical potential of Cook quoted above.

In Fig. 3.8, the calculated and experimental angular distributions of α particles are compared, for several incident energies of ^{6}Li. The dotted and dashed lines are the EBU (CDCC) and NEB (FR-DWBA) results. Except for the lowest energies, the NEB is found to account for most of the inclusive breakup cross section, in agreement with previous findings [89,19]. The summed EBU + NEB cross sections (thick solid lines) reproduce fairly well the shape and magnitude of the data, both above and below the barrier. These results give confidence on the possibility of extending the formulation of the IAV theory to situations in

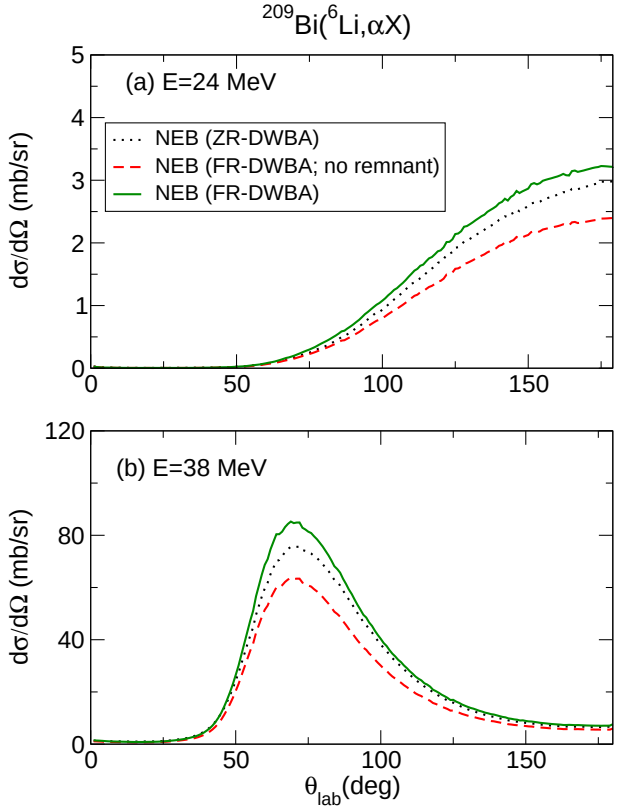

Figure 3.9: Angular distribution of α particles produced by non-elastic breakup (NEB) in the reaction ^{6}Li+^{209}Bi at the incident energies of (a) 24 MeV and (b) 38 MeV. The dotted, dashed and solid lines are the ZR-DWBA, FR-DWBA without remnant term and full FR-DWBA calculations, respectively.

which the unobserved particle is a composite system.

At the most forward angles (where the α yield is nevertheless small) the EBU is found to be larger than the NEB part. Using a semi-classical picture, this can be understood by noting that these small angles will correspond to distant trajectories. However, according to Eq. (2.24), the NEB is only effective for distances within the range of the deuteron-target imaginary potential and hence it will be very small for these distant trajectories. It is worth noting, however, that the separation between EBU and NEB parts in the (^{6}Li,αX) case is less clear than in the (d,pX) case. In the present model, the NEB is associated with the absorption due to the d+target imaginary potential. If an empirical deuteron-target potential is used, part of this absorption will be due to the breakup of the deuteron into p+n. However, in a more realistic description of ^{6}Li in terms of α+p+n, the breakup of ^{6}Li into α+p+n (leaving the target in the ground state) would actually correspond to elastic breakup. Despite this ambiguity, we believe that the sum of the two

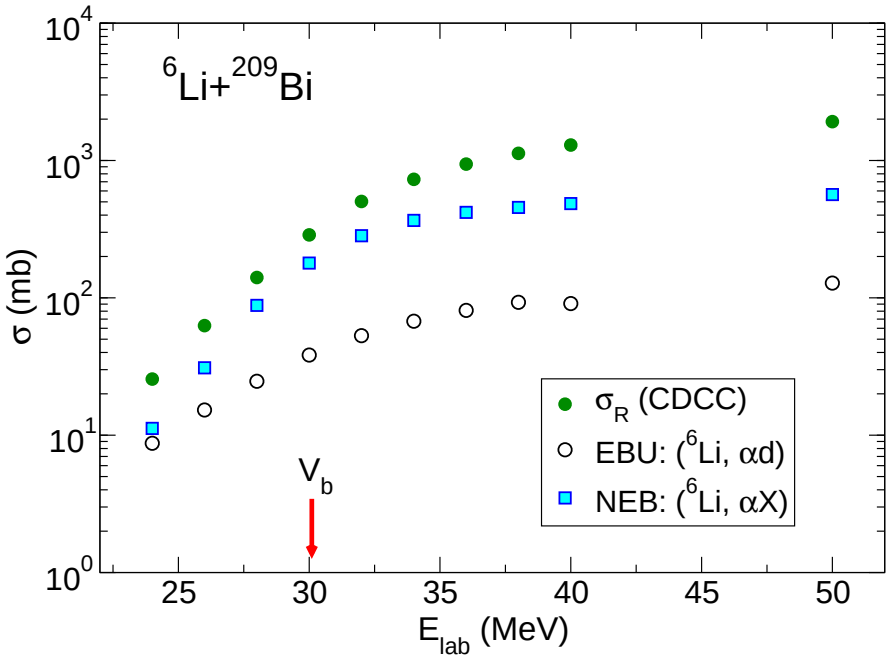

Figure 3.10: Integrated cross sections for the reaction ^{6}Li on ^{209}Bi as a function of the incident laboratory energy. The open circles and the squares are the EBU (CDCC) and NEB (FR-DWBA) contributions to the α inclusive cross section. The solid circles are the reaction cross sections, obtained from the CDCC calculations. The arrow indicates the nominal position of the Coulomb barrier.

contributions, that is, the TBU cross section, can be reasonably well estimated by the present model, as supported by the comparison with the data.

Now the validity of the ZR approximation is studied in the present reaction. This is shown in Fig. 3.9, were we show the angular distribution of α particles produced by NEB, calculated with different DWBA approximations, and at two different energies, one below (24 MeV) and one above (38 MeV) the barrier. The dotted, dashed and solid lines are the ZR-DWBA, FR-DWBA without remnant term and full FR-DWBA results, respectively. It is seen that the ZR-DWBA calculations underestimate systematically the FR-DWBA results by about $\sim 10-20\%$ and hence the validity of the ZR approximation is more questionable than in the deuteron case. Further, it is found that the no-remnant FR-DWBA calculation underestimates the full FR-DWBA result by about $\sim 30-40\%$, indicating that the effect of the remnant term is much more important than in the deuteron case, owning to the strong Coulomb interaction and the difference of the geometry, $\vec{r}_{bA}$ and $\vec{r}_b$, caused by the valence particle.

Finally, the incident energy dependence of the total α yield is studied. This is shown in Fig. 3.10. The

squares and the open circles correspond, respectively, to the NEB (FR-DWBA) and EBU (CDCC) contributions to the α production cross section. At energies above the nominal Coulomb barrier (indicated by the arrow) the NEB largely dominates the inclusive breakup. Below the Coulomb barrier, both contributions become comparable. This can be again explained in classical terms, by noting that, at these small energies, the distance of closest approach will be relatively large, due to the presence of the Coulomb barrier and, therefore, the imaginary part of the d+target potential (which is responsible for the NEB part) will have little effect. We have included in the same plot the total reaction cross sections, as extracted from the CDCC calculations, which are found to be very close to the values calculated with the Cook optical potential (not shown). It is seen that, at energies below the Coulomb barrier, the reaction cross section is almost exhausted by the (^{6}Li,αX) TBU cross section, whereas at energies above the Coulomb barrier other processes beyond the breakup seem to be present (e.g. pure target excitation, α absorption, complete fusion, etc). A more detailed analysis of these processes will be presented in Sec 3.8 .

3.2.2 ^{208}Pb (^{6}Li, αX)

Now the results for the ^{208}Pb(^{6}Li,αX) reaction at several energies between 29 and 39 MeV are presented, comparing with the data from Refs.[122,83]. The Coulomb barrier for this system is around 29.5 MeV[122]. The CDCC calculations use the same structure model and bin discretization as in the ^{209}Bi case. The $d-^{208}$Pb and $\alpha-^{208}$Pb optical potentials are taken from Ref.[57] and Ref.[6], respectively. As in the ^{209}Bi case, the surface term of the imaginary part of the $d+^{208}$Pb potential was removed. For the NEB calculations, the optical potential of ^{6}Li+^{208}Pb is taken from Ref.[29].

Fig. 3.11 shows the comparison of the calculated and experimental angular distributions of α particles produced in this reaction for several incident energies. The dashed and dotted lines are the EBU (CDCC) and NEB (FR-DWBA) results. As in the ^{6}Li+^{209}Bi case, the NEB is found to account for most of the inclusive breakup cross section. The squares and circles are the experimental data taken from Ref.[122] and Ref.[83], respectively. It is observed that there is an appreciable difference between the two sets of data. The sum of EBU and NEB reproduces reasonably well the magnitude and shape of the data of Ref.[122], except for some overestimation.

From the results shown here and in Sec. 3.2.1, it can be concluded that the $\alpha-$emitting channel is the dominant nonelastic breakup process in the ^{6}Li induced reactions on heavy targets. To investigate whether this conclusion is a general feature of ^{6}Li induced reactions or it is true only for specific cases, it

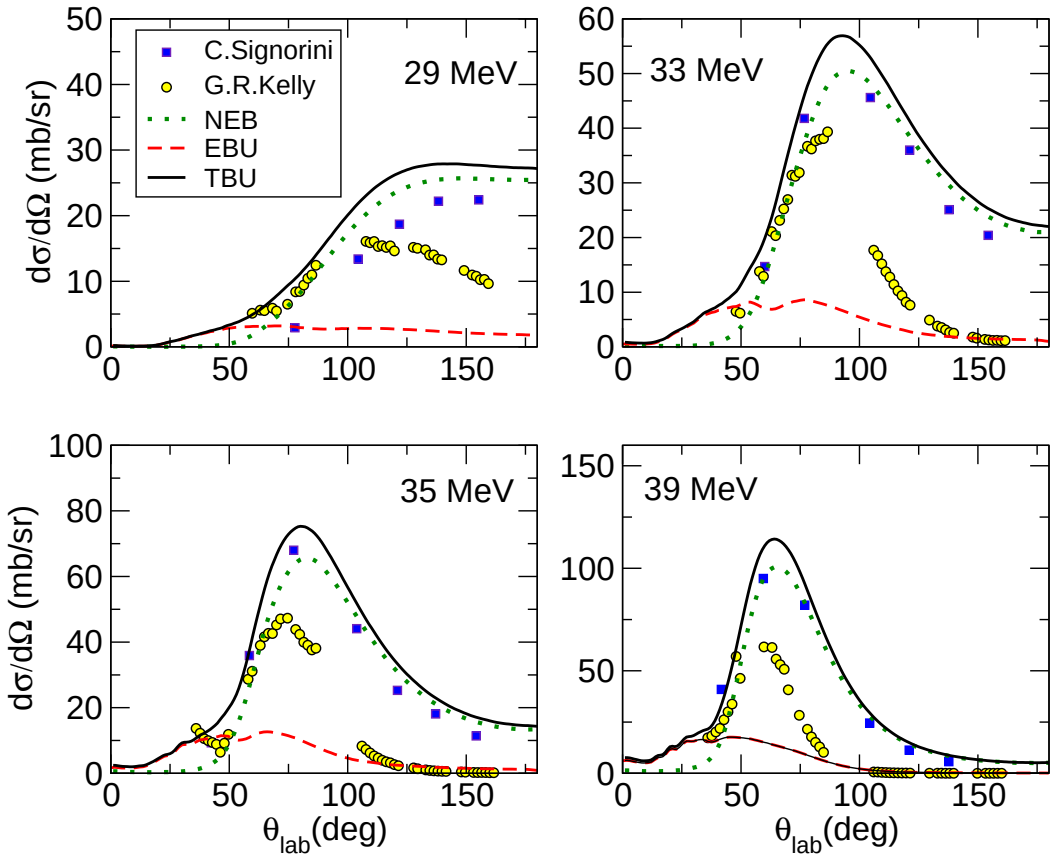

Figure 3.11: Angular distribution of α particles produced in the reaction ^{6}Li+^{208}Pb at the incident energies indicated by the labels. The dotted, dashed and solid lines correspond to the NEB (FR-DWBA), EBU (CDCC) and their sum, respectively. Experimental data are from Ref. [122,83], see text for details.

is important to carry out a systematic investigation of ^{6}Li induced reactions on various targets, especially medium-heavy and medium-mass targets.

3.2.3 ^{159}Tb (^{6}Li, αX)

This section presents the results for the reaction of ^{6}Li on the medium-heavy mass target ^{159}Tb, at several energies between 23 MeV and 35 MeV, whose angular distributions of inclusive α particles have been measured by Pradhan *et. al.* [113]. In Ref. [113], they considered that the inclusive α particles arise from the following processes: (i) breakup of ^{6}Li into α and d fragments where both fragments escape without being captured by the target, i.e., a no-capture breakup (NCBU) process, (ii) α particles resulting from d capture by the target ($d-$ICF), following the breakup of ^{6}Li into α and d, or a one step transfer to the target, (iii)

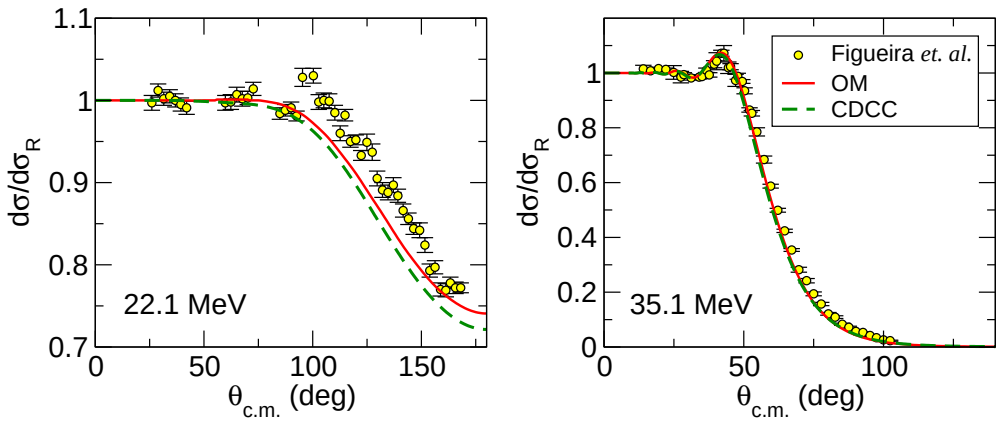

Figure 3.12: Elastic scattering of ^{6}Li+^{144}Sm at different incident energies. The solid and dashed lines are, respectively, the CDCC calculation and the optical model calculation with the optical potential from [29]. The experimental data are from Ref. [51] .

single-proton stripping from ^{6}Li to produce unbound ^{5}He that decays to an α particle plus a neutron, (iv) single-neutron stripping from ^{6}Li to produce an $\alpha-$unstable ^{5}Li, which will subsequently decay into an α particle plus a proton, and (v) single-neutron pickup from ^{6}Li to produce ^{7}Li, which breaks into an α particle and a triton if ^{7}Li is excited above its breakup threshold of 2.468 MeV. Under this assumption, the integrated inclusive $\alpha-$particle cross sections are nearly reproduced, but not for the angular distributions.

Considering the two-body structure of the projectile by using the IAV model, the processes discussed by Pradhan *et. al.* [113] can be re-defined as follows: the process (i) can be divided into two parts. First, the no-capture breakup with the target remaining in its ground state, i.e., EBU. Second, the non-capture breakup accompanied by target excitation, which we call "inelastic breakup" and is part of our "non-elastic breakup" cross section; processes (ii)-(iv) may be also embedded in the NEB part, for wich d is absorbed by the target or d breaks up into a p and a n following the breakup of ^{6}Li into α and d; it can also happen that after the breakup of ^{6}Li, the deuteron picks a neutron to become a tritium, contributing to the process (v). In general processes (ii)-(v) and inelastic breakup can be considered as nonelastic breakup and therefore accounted by IAV formalism.

Here the inclusive $\alpha-$particle cross section is analysed by means of IAV model which divides the inclusive breakup into elastic breakup and nonelastic breakup. First the elastic scattering with the CDCC framework is studied. Since there are no elastic scattering data available for the ^{6}Li+^{159}Tb system, the CDCC calculations are adjusted to reproduce the elastic scattering data of a similar system, i.e., ^{6}Li+^{144}Sm[51]. The same interaction of $\alpha - d$ as discussed in the previous cases is used. The optical

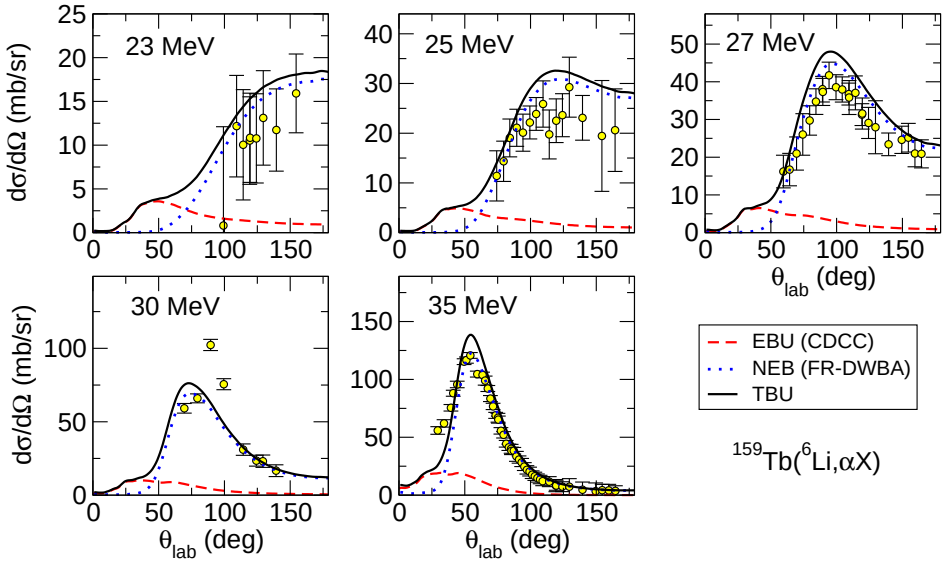

Figure 3.13: Angular distribution of α particle productions of the reaction ^{6}Li+^{159}Tb at the incident energies indicated by the labels. The dashed, dotted and solid lines are EBU calculated with CDCC, NEB calculated with finite-range DWBA and their sum, respectively. The experimental data are taken from Ref. [113]

potentials of $\alpha-^{144}$Sm and $d-^{144}$Sm were evaluated at $2/3$ and $1/3$ of the incident energy of ^{6}Li, respectively. The global optical model potential parameters[65,57] were used to describe the interactions at the corresponding energies. The CDCC calculation is shown in Fig. 3.12 by solid lines. For comparison, the optical model calculation using the potential of Cook[29] (dashed lines) is also shown. It can be seen that the CDCC result is similar to the optical model calculation, particularly at $E = 35.1$ MeV. At this energy, the calculations reproduce very well the elastic data. For the lower energy, the calculations underestimate the data at backward angles. Note that that, in contrast to the ^{6}Li reactions on heavy targets, i.e., ^{6}Li+^{209}Bi (Sec. 3.2.1) and ^{6}Li+^{208}Pb (Sec. 3.2.2), the surface term of imaginary part of $d-$target potential was kept in this case.

Now the inclusive breakup cross sections ^{159}Tb(^{6}Li,αX) are discussed. The EBU contribution was obtained from the CDCC calculations discussed in the previous paragraph. For the NEB calculation, the same optical potentials $\alpha/d+^{144}$Sm were used. The Cook potential[29] was used to calculate the distorted wave of the incoming channel.

In Fig. 3.13, the calculated and experimental angular distributions of α particles are compared, for several incident energies of ^{6}Li. The dashed and dotted lines are the EBU (CDCC) and NEB (FR-DWBA) results. Similar to the heavy target systems, i.e., ^{6}Li+^{209}Bi (Sec. 3.2.1) and ^{6}Li+^{208}Pb (Sec. 3.2.2), the

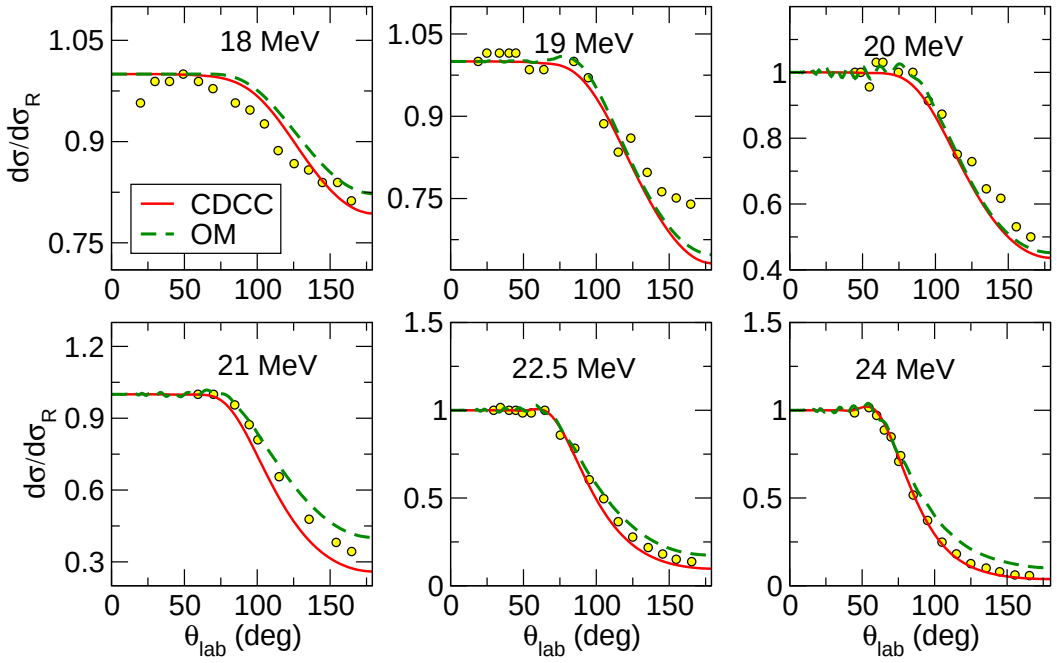

Figure 3.14: Elastic scattering of ^{6}Li+^{118}Sn at different incident energies. The solid and dashed lines are, respectively, the CDCC calculation and the optical model calculation with the optical potential from [110]. Experimental data are from Ref. [110].

NEB is found to account for most of the inclusive breakup cross section, and the summed EBU + NEB cross sections (solid lines) reproduced fairly well the shape and magnitude of the data, except some small overestimation.

3.2.4 ^{118}Sn (^{6}Li, αX)

In this section the results for ^{118}Sn(^{6}Li, αX) at energies between 18 and 24 MeV are presented and compared with the data from Ref. [110]. The optical potential parameterizations of Refs [65,57] are used for $\alpha-^{118}$Sn and $d-^{118}$Sn. For the NEB calculations, the optical potential of ^{6}Li+^{118}Sn is taken from Ref. [110].

First the validity of the two-cluster of ^{6}Li was studied for the elastic scattering of ^{6}Li + ^{118}Sn at several incident energies. It is found that the CDCC calculations with this model give a good agreement with the experimental data. This is shown in Fig. 3.14 by solid lines. For comparison, the optical model calculation using the potential mentioned in Ref. [110] (dashed lines) is also shown.

Fig. 3.15 shows the comparison of the calculated and experimental angular distributions of α particles produced in the reaction ^{6}Li+^{118}Sn, for several incident energies. The dashed line is the EBU result from

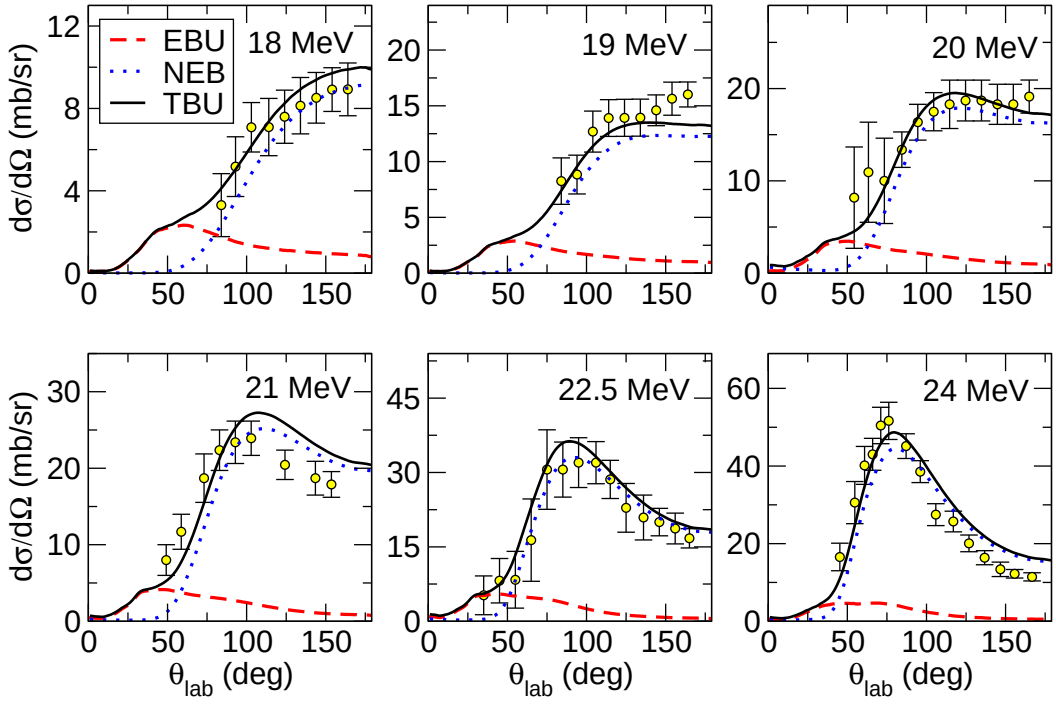

Figure 3.15: Angular distribution of α particles produced in the reaction ^{6}Li+^{118}Sn at the incident energies indicated by the labels. The dotted, dashed and solid lines correspond to the NEB (FR-DWBA), EBU (CDCC) and their sum, respectively. Experimental data are from Ref. [110].

the CDCC calculation, whereas the dotted line is the NEB result using the IAV formalism. It can be seen that NEB accounts for most of the inclusive breakup cross section and the EBU becomes the dominant breakup mode for angles smaller than $\sim$ 50 degrees. The summed EBU + NEB (solid line) reproduces remarkably well the shape and magnitude of the data.

We have seen that the IAV model works rather well for ^{6}Li reactions with heavy-mass and medium-mass targets. In the following subsections, we examine the validity of the model for the lighter targets.

3.2.5 ^{59}Co (^{6}Li, αX)

As discussed before, for the heavy mass targets ^{209}Bi and ^{208}Pb and medium-heavy mass targets ^{159}Tb and ^{118}Sn the nonelastic breakup process dominates the inclusive α production in the ^{6}Li induced reactions. In this section we present analysis of the reaction of ^{6}Li on a much higher mass target, ^{59}Co, at $E_{\rm lab} = 21.5$ MeV, which is above the Coulomb barrier ($V_B = 12.0$ MeV). The inclusive α particles have been reported by Souza *et. al.* [124]. First the elastic scattering is studied with the CDCC method to test the validity of

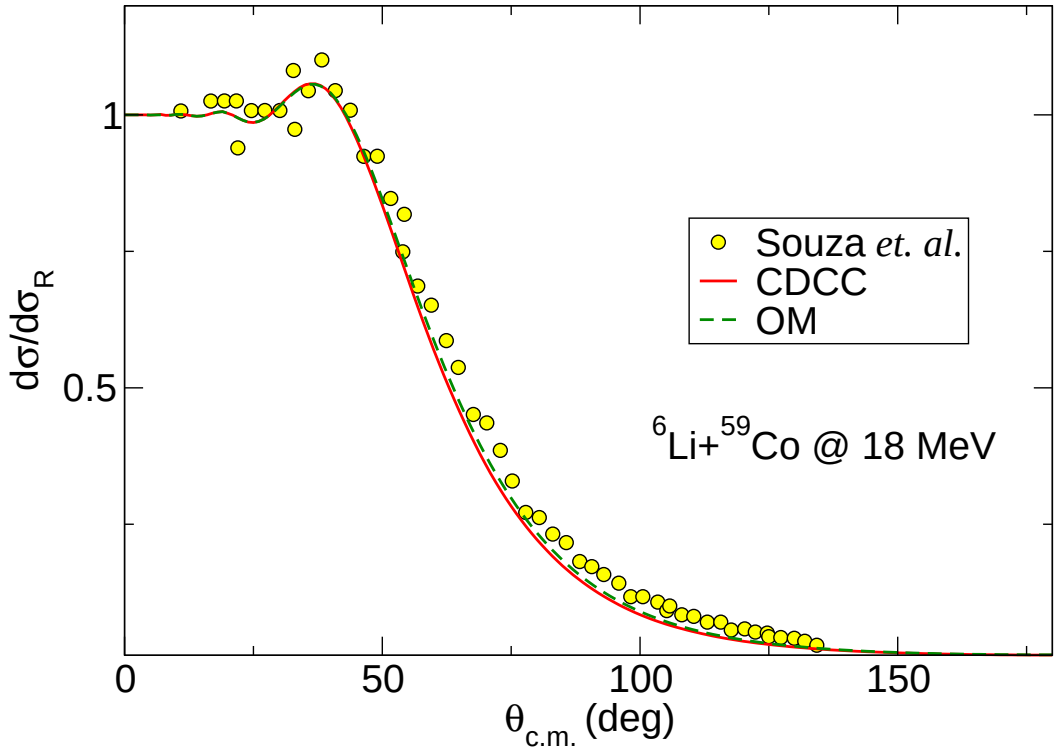

Figure 3.16: Elastic scattering of ^{6}Li+^{59}Co at incident energy of 18 MeV. The solid and dashed lines are, respectively, the CDCC calculation and the optical model calculation with the optical potential from [29]. Experimental data are from Ref. [125].

the two-body projectile model in this reaction. Since there are no elastic scattering data available at 21.5 MeV, the CDCC calculation is compared with the elastic scattering data at a lower energy, i.e., $E_{\rm lab} = 18$ MeV. The optical model potentials for α+^{59}Co and d+^{59}Co were taken from Refs [65] and [57], respectively, and evaluated at $2/3$ and $1/3$ of the incident ^{6}Li energy. The CDCC calculation is shown in Fig. 3.16 by the solid line. For comparison, the optical model calculation using the potential of Cook [29], dashed line, is also shown. It can be seen that both CDCC and optical model calculations reproduce fairly well the experimental data of Souza *et. al.* [125]. We notice that no renormalization of the deuteron potential was required in this case.

Now the inclusive breakup cross section ^{59}Co (^{6}Li, αX) is discussed. The EBU contribution was obtained from the CDCC calculation discussed above. The distorted wave for the incoming channel is calculated with the optical potential of Cook [29]. In Fig. 3.17, the calculated and experimental angular distributions of α particles are compared. The dashed and dotted lines are, respectively, the EBU (CDCC)

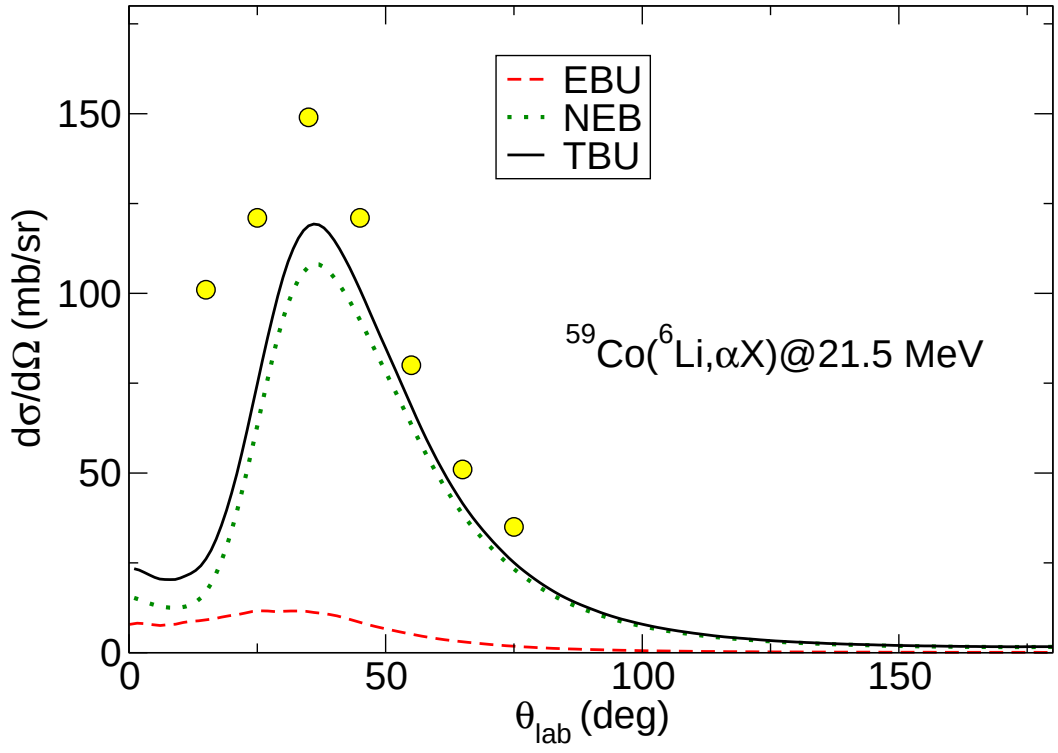

Figure 3.17: Angular distribution of α particles produced in the reaction ^{6}Li+^{59}Co at incident energy of 21.5 MeV. The dashed, dotted, and solid lines are, respectively, the EBU (CDCC), NEB(FR-DWBA) and their sum. Experimental data are taken from Ref. [124].

and NEB (FR-DWBA) calculations. Except for the forward angles, the NEB was found to dominate the inclusive α productions. The summed cross section, EBU + NEB, reproduces well the shape of the experimental data, although the magnitude is underestimated by 30% at the maximum. This might indicate that, in this reaction, there might be other relevant mechanisms leading to the production of α particles. Possible candidates are the formation of a compound nucleus followed by α evaporation and also transfer populating bound states of the target.

The experimental and calculated α production spectra for $E_{\rm lab} = 21.5$ MeV and at $\theta_{\rm lab} = 15°$, 25°, 35°, 45°, 55°, 65° and 75° are shown in Fig. 3.18. Except at $\theta_{\rm lab} = 15°$, the sum of EBU and NEB reproduces the peak of the α production spectra. For the low energy part, the main contribution of the inclusive α production may come from compound nucleus followed by evaporation and pre-equilibrium which is not considered in the present calculations, whereas for high energy α particles may be attributed to the contribution of transfer (n, p, or d) to the target. Further calculations are planned to investigate

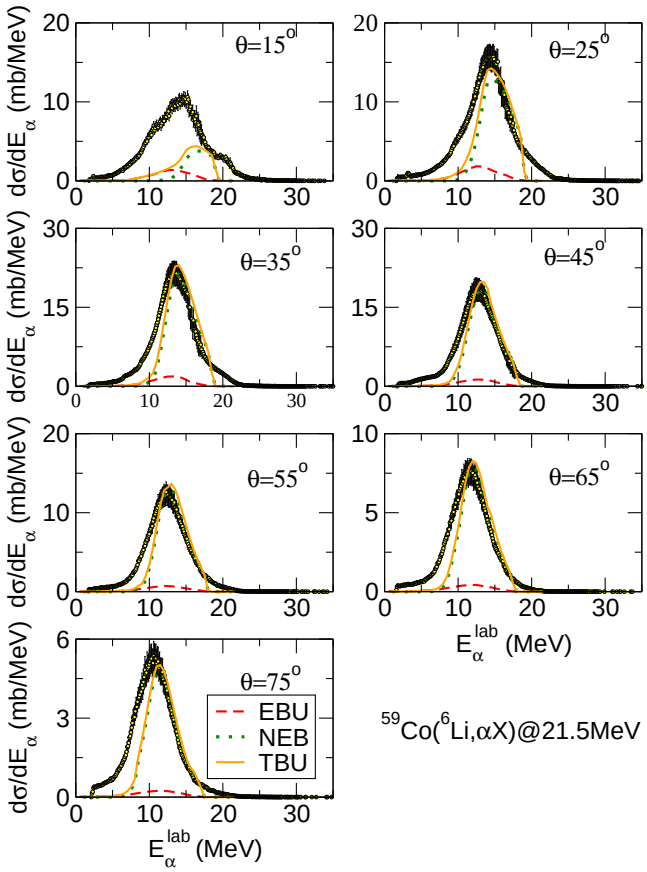

Figure 3.18: Experimental and calculated inclusive α energy spectra for $E_{\rm lab} = 21.5$ MeV, at $\theta_{\rm lab} = 15, 25, 35, 45, 55,$ 65 and 75 degrees. The dashed, dotted, and solid lines are respectively the EBU (CDCC), NEB(FR-DWBA) and their sum. Experimental data are taken from Ref. [124].

these possibilities.

3.2.6 ^{58}Ni (^{6}Li, αX)

Now the α production of ^{6}Li + ^{58}Ni at several incident energies between 12 MeV and 20 MeV is studied. The angular distributions of inclusive α particles have been measured by Pfeiffer *et. al.* [110]. To test the two-body structure of ^{6}Li and the fragment-target interactions, the elastic scattering data were compared with CDCC calculations. The same optical model potentials as in the ^{6}Li+^{59}Co case were used. Fig. 3.19 shows the elastic scattering of ^{6}Li + ^{58}Ni at several energies. The solid lines are the CDCC calculations which give good agreement with the experimental data from Ref. [110]. For comparison the optical model calculation using the potential mentioned in Ref. [110] (dashed line) is also shown.

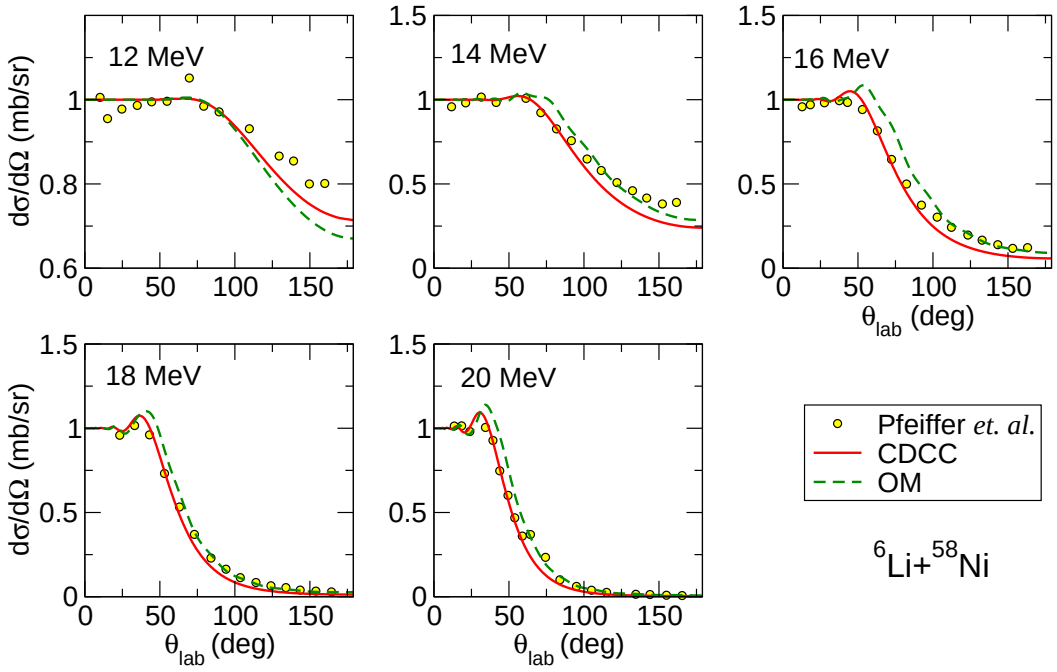

Figure 3.19: Elastic scattering of ^{6}Li+^{58}Ni at several energies indicated by the labels. The solid and dashed lines are, respectively, the CDCC calculation and the optical model calculation with the optical potential from [110]. Experimental data are from Ref. [110].

We present now the inclusive alpha cross sections. For the NEB calculation, the ^{6}Li optical potential from Ref. [110] was used. Fig. 3.20 shows the comparison of the calculated and experimental angular distributions of α particles produced in this reaction, for several incident energies. The dashed line is the EBU result obtained with the CDCC calculation and the dotted line is the NEB result using the IAV formalism. Again, the NEB part dominates the inclusive α productions. In general, the summed EBU + NEB cross section (solid lines) reproduces fairly well the shape and magnitude of the data. At 14, 16 and 18 MeV some underestimation is observed, which might be associated with other α-production channels, as pointed out in the ^{6}Li+^{59}Co case.

From the results presented in the previous sections, we may conclude that the strong α-production channel observed in ^{6}Li experiments originates mostly from non-elastic breakup mechanisms. In all cases analyzed so far, the EBU mode turns out to account for a relatively small fraction of the total inclusive alpha cross section and its contribution is only important for the alpha particles emitted at small angles. We found also a indirect evidence that other alpha production mechanisms, such as fusion or transfer, might have some contribution for the lighter targets.

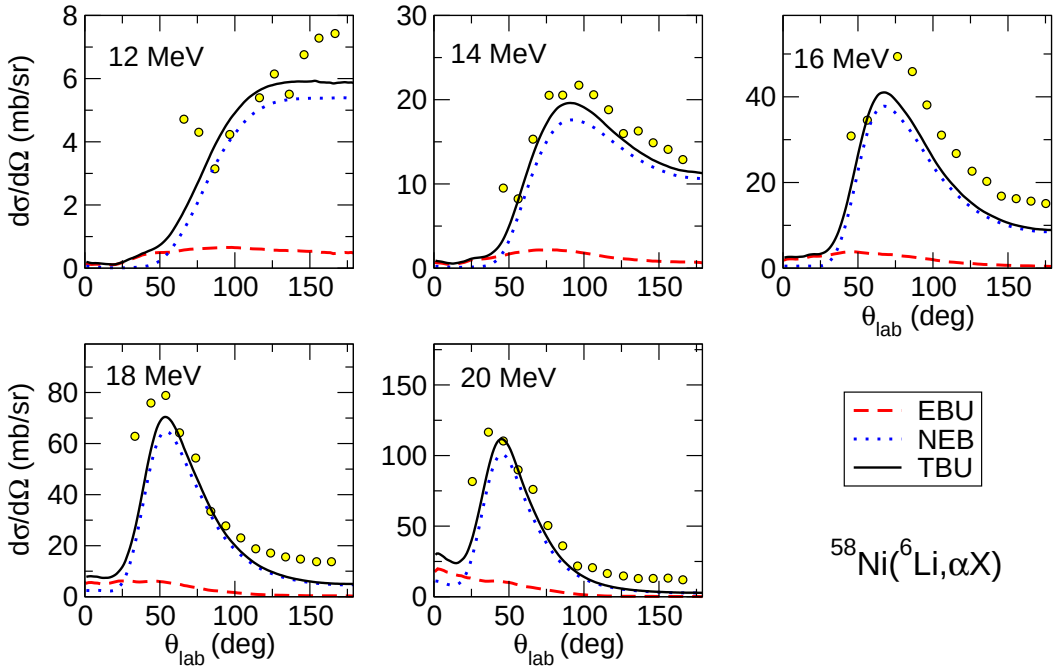

Figure 3.20: Angular distribution of α particles produced in the reaction ^{6}Li + ^{58}Ni at the incident energies indicated by the labels. The dashed, dotted and solid lines are, respectively, the EBU (CDCC), NEB (FR-DWBA) and their sum. Experimental data are from Ref.[110].

3.2.7 Systematics of inclusive α production

Systematic studies of α production yields in ^{6}Li reactions show an interesting universal behaviour when plotted as a function of the incident energy scaled by the Coulomb barrier energy. As an example, we show in Fig. 3.21 the results reported by Pakou *et. al.*[107]. It is seen that the experimental α production shows some kind of universal behaviour except for a few cases (^{6}Li+^{28}Si and ^{6}Li+^{58}Ni). In this section, we will investigate whether our calculations exhibit also this universal behaviour. For this study, we have considered the systems ^{59}Co, ^{118}Sn, ^{159}Tb, ^{208}Pb and ^{209}Bi. The results are shown in Fig. 3.22 (a), where we plot the calculated $\sigma_{\alpha}^{\rm TBU}$ cross sections as a function of the reduced energy ($E_{\rm c.m.}/V_{\rm b}$), with $V_{\rm b}$ the energy of Coulomb barrier, estimated as $V_{\rm b} = Z_p Z_t e^2/(r_B(A_p^{1/3} + A_t^{1/3}))$, where Z_p (Z_t) and A_p (A_t) are atomic number and atomic mass of the projectile (target), respectively, and $r_B = 1.44$ fm. The squares, circles, diamonds, up triangles, left triangles and down triangles correspond, respectively, to the reactions of ^{6}Li + ^{58}Ni, ^{6}Li + ^{59}Co, ^{6}Li + ^{118}Sn, ^{6}Li + ^{159}Tb, ^{6}Li + ^{208}Pb and ^{6}Li + ^{209}Bi. It can be seen that for the medium-heavy and heavy targets the inclusive breakup cross sections show same trend,

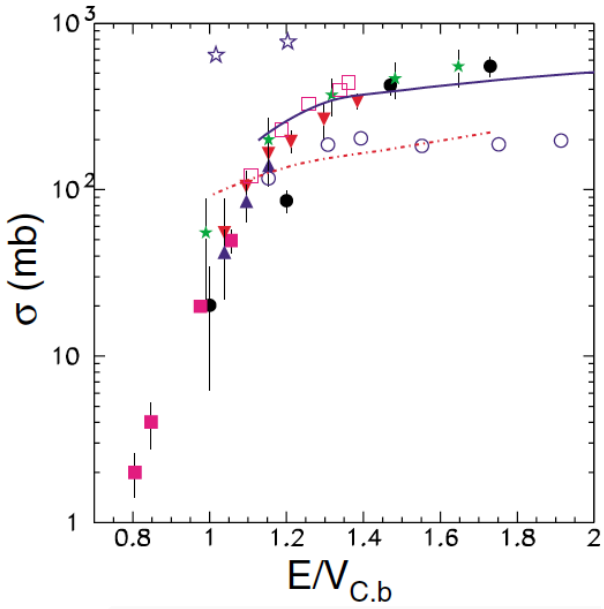

Figure 3.21: α particle cross section in reactions involving ^{6}Li scattering on several targets. ^{6}Li+^{28}Si, ^{6}Li+^{58}Ni, ^{6}Li+^{118}Sn, ^{6}Li+^{120}Sn, and ^{6}Li+^{208}Pb are designated with solid circles, solid stars, up and down solid triangles, and solid boxes, respectively. The plot is taken from Ref. [107].

but not for the medium mass targets. We recall however that, for these lighter systems, there might be additional contributions from other channels, such as compound nucleus and transfer to bound states, which are not accounted for by the IAV formalism. Fig. 3.22 (b) shows the reduced inclusive breakup α cross sections, $\sigma_{\alpha}^{\mathrm{TBU}}/(\pi R_B^2)$ with $R_B^2 = r_B(A_p^{1/3} + A_t^{1/3})$, as a function of the reduced energy. The curves of reduced inclusive breakup cross sections are clearly different for medium, medium-heavy and heavy mass targets. For a given reduced energy, the reduced inclusive breakup cross section decreases with the product Z_pZ_t, in agreement with the calculations of Ref. [24].

We have also studied the relative importance of EBU versus NEB as a function of the incident energy. For that, we display in Fig. 3.23 the ratio of EBU over TBU (= EBU + NEB) It is seen that, for incident energies below the Coulomb barrier, the elastic breakup cross section becomes comparatively more important as the energy decreases. By constrast, for energies above the Coulomb barrier, the ratio shows an almost constant behavior. It can also be seen that, while for the heavy mass targets elastic breakup plays an important role in the inclusive α production, especially below the Coulomb barrier, for the medium mass targets elastic breakup is less important and the nonelastic breakup is dominant.

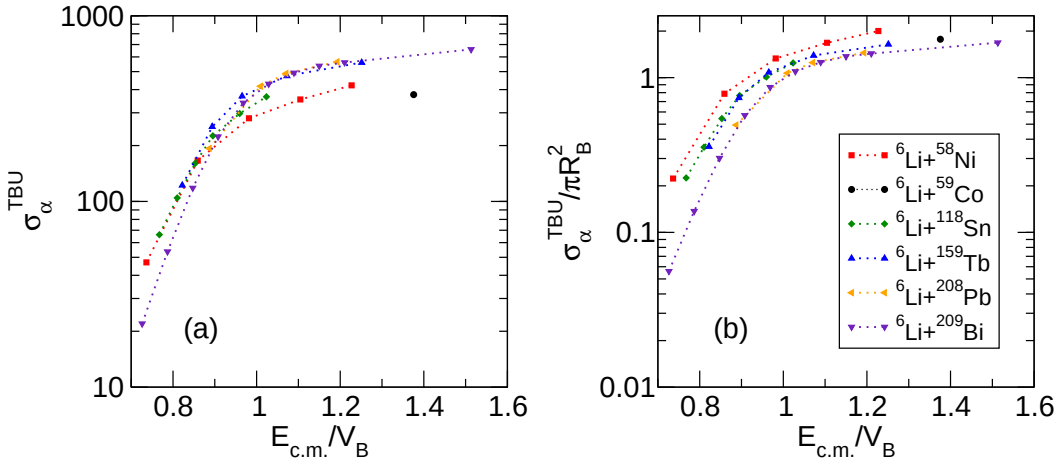

Figure 3.22: (a) Inclusive breakup α cross sections involving ^{6}Li projectile with several different targets as a function of $E_{\mathrm{c.m.}}/V_{\mathrm{b}}$. (b) Reduced inclusive breakup α cross sections as a function of $E_{\mathrm{c.m.}}/V_{\mathrm{b}}$ for the same systems as (a). See text for the details.

In conclusion, the α production in the reactions involving the weakly bound ^{6}Li projectile and different masses and charges targets have been discussed in this subsection. The calculated total breakup cross sections (TBU = EBU + NEB) showed some universal trend for the heavy targets, but significant deviations have been found for the light targets. This could indicate that the latter do not obey the universal behaviour, but we cannot rule out that the deviations are due to the presence of additional α production mechanisms, not included in our calculations. This problem deserves further investigation which goes beyond the goals and capabilities of this dissertation.

3.3 (^{11}Be,^{10}Be X)

So far, we have considered the case of reactions induced by the weakly bound nuclei d and ^{6}Li. We extend now our study to the case of the halo nuclei, considering first the case of ^{11}Be. This nucleus has been largely studied in the literature, both experimentally and theoretically. It is the archetype of one-neutron halo nucleus in which one nucleon has a large probability of being at large distances of the center of the nucleus, well beyond the range of the nuclear potential. It has a single bound excited state and a very small separation energy (0.5 MeV). Consequently, this nucleus breaks easily in collisions with other nuclei. In particular, in reactions with heavy targets, the nucleus is strongly polarized due to the action of the Coulomb potential on the ^{10}Be core, thus favouring the dissociation of the projectile. Therefore,

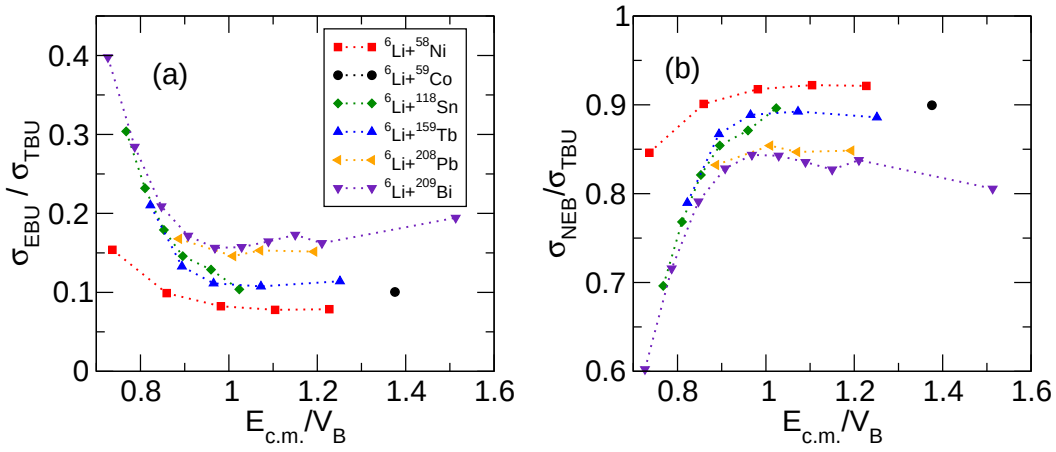

Figure 3.23: (a) Ratios of calculated EBU over TBU (= EBU + NEB) for different systems. (b) Ratios of calculated NEB over TBU (= EBU + NEB) for different systems. See text for the details.

elastic breakup is expected to be an important breakup mode. Experimental data for ^{10}Be observables in reactions with ^{11}Be have been reported in Refs.[36,109,35]. These works suggest that the inclusive ^{10}Be cross section is dominated by the elastic breakup. In this section, we focus on the calculation of nonelastic breakup process of ^{11}Be on a medium mass target, ^{64}Zn.

For that purpose, the ^{11}Be + ^{64}Zn reaction at an incident energy of 28.7 MeV, corresponding to about 1.4 times the Coulomb barrier, was considered. The EBU part is estimated using the CDCC formalism, assuming a ^{10}Be + n two-body model for ^{11}Be. Within this simplified model, the ^{11}Be ground state ($1/2^+$) and the first excited state ($1/2^-$; $E_x = 320$ KeV) are described, respectively, by the pure single-particle configurations $2s_{1/2}$ and $1p_{1/2}$, coupled to the ground state of ^{10}Be. In order to attain convergence of the calculated cross sections, we needed to include $n-^{10}$Be partial waves up to $\ell \approx 5$, and a maximum excitation energy of $\varepsilon = 12$ MeV, with respect to the neutron separation threshold.

The $n-^{10}$Be interaction, which is required to generate the ^{11}Be wave functions, was adopted from Ref.[25]. This potential consists of a central and a spin-orbit components, of WS shape, with a fixed geometry and a parity-dependent depth. For even partial waves, this potential reproduces the ground state separation energy as well as the position of the $5/2^+$ resonance at $E_x = 1.8$ MeV, assuming that these states are described by pure $2s_{1/2}$ and $1d_{5/2}$ configurations, respectively. For the $\ell = 1$ states, the depth was adjusted to reproduce the separation energy of the $1/2^-$ bound state. For other odd partial waves, the depth determined for $\ell = 1$ was used. We note that this potential reproduces also the continuum $B(E1)$ distribution extracted from the Coulomb dissociation experiment of Fukuda *et. al.*[52].

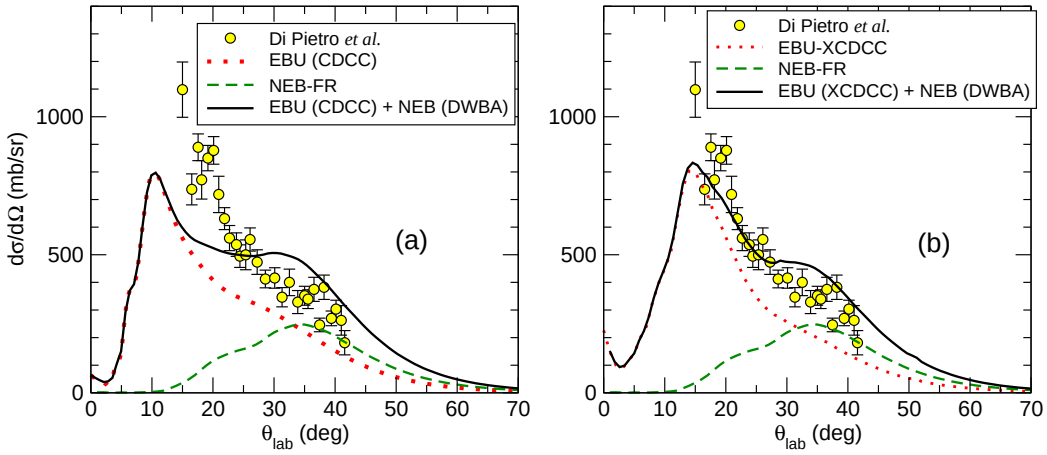

Figure 3.24: Differential cross section for the angular distribution of inclusive ^{10}Be produced in ^{11}Be+^{64}Zn. (a) Elastic breakup calculated with CDCC (dotted line), nonelastic breakup with (FR-DWBA) and their sum (solid line). (b) Elastic breakup calculated with XCDCC (dotted line), nonelastic breakup with (FR-DWBA) and their sum (solid line). I The experimental data are from Ref.[36].

The optical potential for ^{10}Be-target was taken from Ref.[36] where it was extracted from the fit of the ^{10}Be + ^{64}Zn elastic scattering data. The $n-$target potential was taken from the global parametrization of Koning and Delaroche[88], evaluated at the corresponding energy. For the NEB calculation, the optical potential of ^{11}Be+^{64}Zn was also taken from Ref.[36]. This potential reproduces the elastic scattering data.

The calculated inclusive ^{10}Be angular distribution is compared with the experimental results in Fig. 3.24. In panel (a) the EBU contribution (dotted line) was obtained from the CDCC calculation discussed above. It can be seen that the EBU contribution dominates the inclusive ^{10}Be production, and follows a similar shape compared with the data, but the absolute magnitude is underestimated by about 30% for angles around $\theta = 20°$. The NEB obtained from the IAV model (dashed line in Fig. 3.24) shows a comparable contribution with EBU for angles larger than 30 degrees and becomes negligible for small angles. The underestimation at the smaller angles ($\theta < 25°$), it can be attributed to the limitations of the structure model used for the ^{11}Be nucleus. Recent studies have demonstrated that this simple single-particle picture is not accurate for ^{11}Be due to the effect of core excitations. These effects have been recently incorporated in an extended version of the CDCC formalism (XCDCC)[126,33]. Calculations using this XCDCC method have been recently reported for this reaction[33], so we include also these results for comparison. These results are shown in Fig. 3.24 (b), where the EBU is now obtained with the XCDCC method, whereas the IAV is the same as in the panel (a). As anticipated, the inclusion of core excitations produces an increase

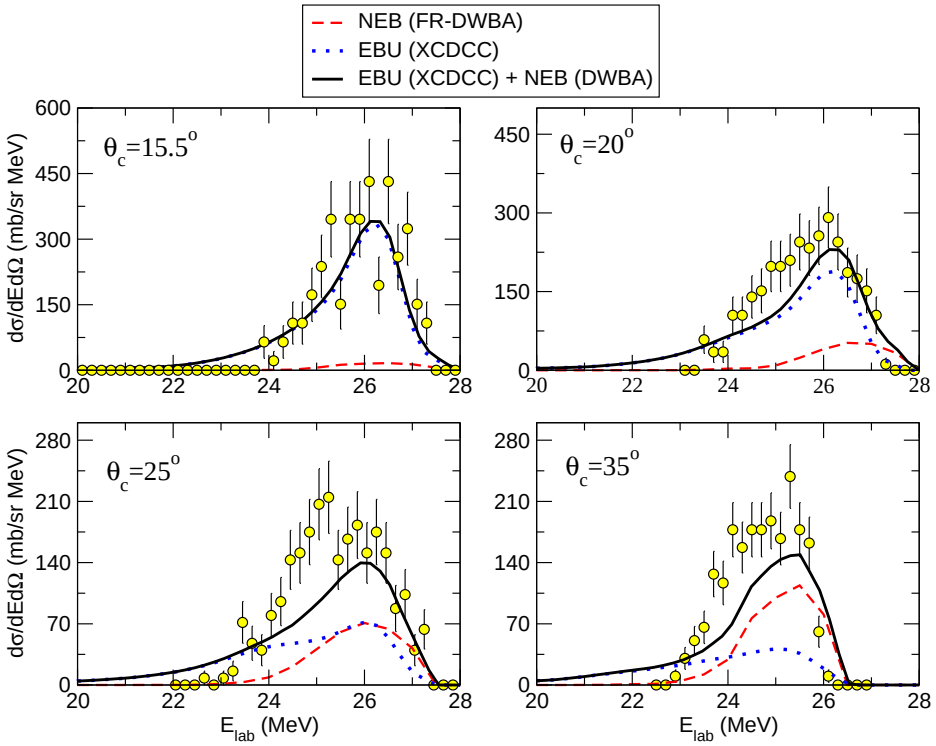

Figure 3.25: Experimental and calculated inclusive ^{10}Be energy distributions produced in the reaction ^{11}Be + ^{64}Zn at energies of 28.7 MeV for the laboratory angles indicated. The dotted, dashed and solid lines are respectively, the EBU (XCDCC), NEB (DWBA) and their sum. The experimental data were taken from Ref. [111].

of the EBU contribution, improving significantly the agreement with the data at small angles.

Ideally, the NEB should be also calculated with the same structure model used in the XCDCC calculations. However, this extension has not yet been implemented.

In addition, we show in Fig. 3.25 the calculated breakup energy distributions of the ^{10}Be fragments, together with with the preliminary data for this channel[111] , for four measured laboratory angles. The solid curves are the sum of EBU obtained with XCDCC (dotted lines) and NEB (dashed lines) calculated with DWBA. The general features of the data, their magnitude, centroids, and widths, are well described by the calculations. For the forward angles, the EBU component dominates the TBU, whereas the NEB part is relatively small. At larger angles, i.e., $\theta = 25^o$ and $\theta = 35^o$, the NEB cross section are comparable with EBU.

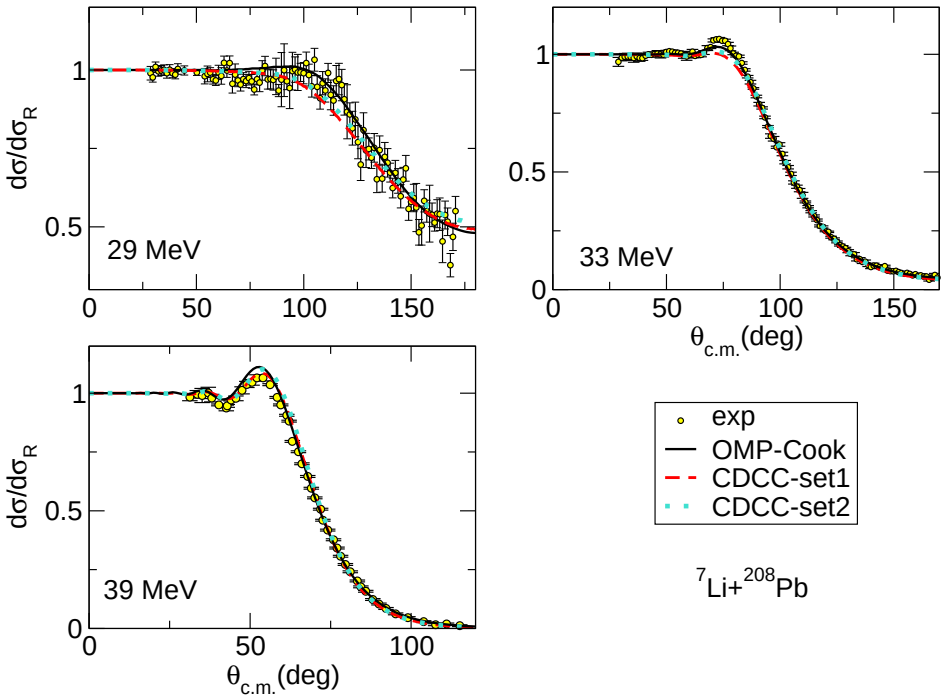

Figure 3.26: Elastic scattering of ^{7}Li + ^{208}Pb at different incident energies. The dashed, dotted and solid lines are, respectively, with the full t—target imaginary part of the optical potential, reduced t—target imaginary part and the optical potential from Ref.[29]. experimental data are taken from Ref.[81]

3.4 (^{7}Li,αX)

For the three projectiles considered so far (^{6}Li, d, ^{11}Be) the g.s. consists of a s wave configuration and we have been able to use the simplified NEB formula for $l_{bx} = 0$ (see Sec. 2.2.1). To test the validity of the IAV model, it is important to extend our study to more general cases, for which $l_{bx} \neq 0$.

For that purpose, the ^{7}Li+^{208}Pb reaction at bombarding energies between 29 and 39 MeV were considered, for which experimental data exit. The ^{7}Li nucleus is treated in a two-cluster model ($\alpha + t$). Compared to the ($\alpha + d$) two-cluster model of ^{6}Li, the main difference between the two nuclei is the internal angular momentum l_{bx}, for ^{6}Li $l_{bx} = 0$, whereas for ^{7}Li $l_{bx} = 1$. Furthermore the difference in breakup threshold energy of the two Li isotopes, 1.474 MeV for $\alpha + d$ breakup of ^{6}Li compared to 2.468 MeV for the $\alpha + t$ breakup of ^{7}Li is also important.

In order to test the validity of the α+t two cluster model of ^{7}Li breakup, first the elastic scattering of the same reaction was studied using the CDCC framework. The $\alpha-t$ interaction, which is required to generate

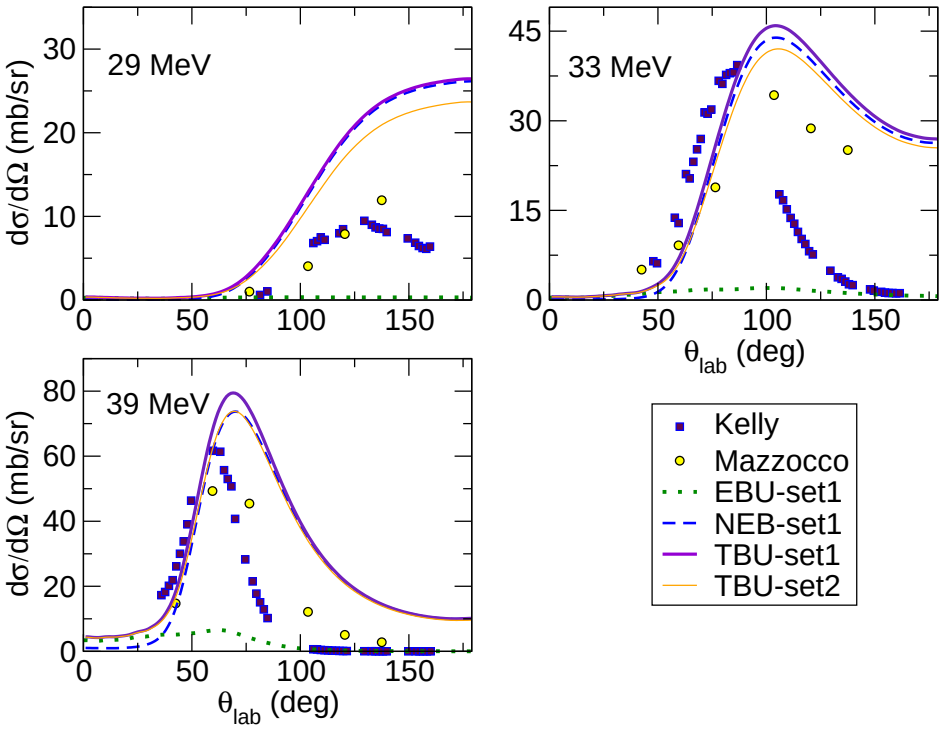

Figure 3.27: Angular distribution of α particles produced in the reaction ^{7}Li + ^{208}Pb at energies indicated by the labels. The dotted, dashed and thick solid lines are, respectively, the EBU, NEB and their sum, for which the calculations were performed with full imaginary part of $t-^{208}$Pb optical potential. For comparison, the TBU calculation with the reduced imaginary part of the $t-^{208}$Pb optical potential is also showed as thin solid line. The experimental data are taken from Refs. [98,83]

the ^{7}Li ground state wave function as well as the bound excited state and continuum wave functions was taken from Ref. [16]. This potential consists of a central and a spin-orbit component, of Gaussian shape, with a fixed geometry and a parity-dependent depth. The potential well depths were adjusted to give the correct binding energy or resonance energy for bound or resonant states, respectively. In order to achieve the convergence of the calculated cross sections, we needed to include $\alpha - t$ partial waves up to $\ell = 3$. For the f wave, a finer division of bins is used in order to reproduce the $\ell = 3$ resonant states at 4.63 MeV $(7/2^-)$ and 6.68 MeV $(5/2^-)$ correctly. The $\alpha-^{208}$Pb and $t-^{208}$Pb optical potentials are taken from Refs. [6] and [78], respectively. For comparison, the optical model calculation using the potential of Cook [29] was also performed. Fig. 3.26 shows the elastic scattering of ^{7}Li + ^{208}Pb at different incident energies. The data are taken from Ref. [81]. The dashed and solid lines are, respectively, the CDCC and optical model calculations. It can be seen that the optical model calculation reproduces better the data, particularly at

$E = 29$ MeV. As in the ^{6}Li case we have performed and additional calculation allowing for a modification of the fragment-target potentials. In this case, we modified the t+^{208}Pb potential, which was rescaled by 0.8. The corresponding elastic angular distributions, displayed by the dotted line in Fig. 3.26, show a better agreement with the optical model calculation and hence with the data.

Now the inclusive breakup cross section (^{7}Li,αX) is discussed. The EBU part was obtained from the CDCC calculation discussed above with both the full imaginary part as well as with the reduced imaginary part of $t-^{208}$Pb optical potential. The NEB part was calculated with the IAV model using the exact finite range DWBA formalism with the two sets of $t-^{208}$Pb optical potentials. In Fig. 3.27 the dotted and dashed lines are, respectively, the EBU (CDCC) and NEB (DWBA) components calculated with the full $t-^{208}$Pb optical potential. First, it is noticeable that the two data sets[98,83] agree with each other well at forward angles, but they clearly differ at backward angles. We recall that a similar discrepancy was already found for the ^{6}Li+ ^{208}Pb data, measured by the same groups. Concerning the comparison with the calculations, we observe a good agreement with the data by Mazzocco *et. al.*[98] at forward angles for $E = 33$ and 39 MeV, but a large overestimation at larger angles. At 29 MeV, the overestimation is observed in the full angular range. This discrepancy is found for the two potential sets. The reason of that is not clear at this stage but new experimental data for this, or nearby systems, would be desirable to clarify this large discrepancy.

3.5 (^{7}Be,$\alpha/t\,X$)

We consider now the similar case ^{7}Be. Being the mirror nucleus of ^{7}Li, they exhibit a similar structure. The ^{7}Be nucleus is radioactive with a well pronounced ^{3}He + ^{4}He cluster structure and is bound by only 1.586 MeV with respect to ^{7}Be $\rightarrow$ ^{3}He + ^{4}He breakup. As in the ^{7}Li case, the g.s. of ^{7}Be has a dominated $l_{bx} = 1$ configuration. We have performed calculations for the ^{7}Be+^{58}Ni reaction which has been recently measured at an incident energy of 21.5 MeV[99]. Interestingly, these data show a dominance of the alpha production channel over the ^{3}He channel (by a factor of $\sim$ 4). This suggest that these fragments are not produced by elastic breakup but more complicated processes are present. Consequently, we may anticipate a large contribution arising from NEB.

The EBU component was calculated within the CDCC framework. The ^{4}He-target was obtained from a Woods-Saxon potential fit to the 12 MeV ^{4}He + ^{58}Ni elastic scattering data of Ref.[90] with the following parameters : $V = 49.5$ MeV, $R_0 = 5.88$ fm, $a_0 = 0.5$ fm, $W = 11.0$ MeV, $R_w = 5.69$ fm and $a_w = 0.5$ fm.

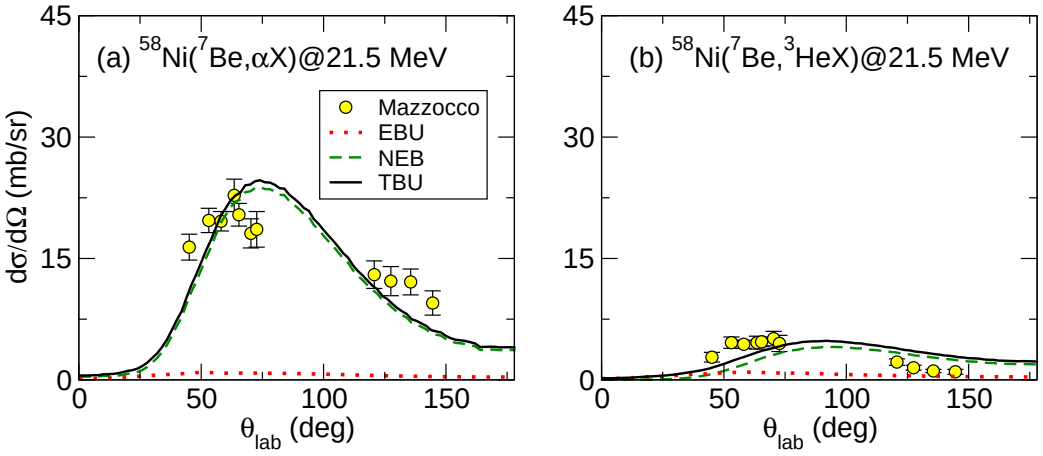

Figure 3.28: Angular distribution of α particles (a) and ^{3}He particles (b) produced in the reaction ^{7}Be + ^{58}Ni at energies of 21.5 MeV. The dotted, dashed and thick solid lines are, respectively, the EBU (CDCC), NEB (DWBA) and their sum. The experimental data are taken from Ref.[99]. Note the different scale of the plots.

The ^{3}He-target interaction was taken from the 8.95 MeV t+^{58}Ni parameters of Ref.[50]. The interaction between the ^{7}Be cluster constituents was taken from[16]. This potential was properly tuned to reproduce the binding energies of the ^{7}Be ground state and first excited state and also the excitation energies of the $7/2^-$ ($E_{ex} = 4.57$ MeV) and $5/2^-$ ($E_{ex} = 7.21$ MeV) resonances assuming a $\ell = 3$ configuration. The continuum states in ^{7}Be were discretized up to 12 MeV above the ^{3}He + ^{4}He breakup threshold. Finer energy bins were introduced for the resonances. For the NEB calculations, the ^{7}Be + ^{58}Ni optical potential was taken from the 21.5 MeV ^{7}Li + ^{58}Ni parameters from Ref.[29].

Fig. 3.28(a) shows the angular distribution of α particles. The dotted line is the EBU component calculated by the CDCC formalism, whereas the dashed line is the NEB part obtained by the DWBA version of IAV model. In contrast to the ^{7}Li + ^{208}Pb case, the sum of EBU and NEB (solid line) reproduces fairly well the shape and magnitude of the experimental data. Fig. 3.28(b) shows the angular distribution of ^{3}He particles. The EBU part was obtained from the same CDCC calculation, whereas for the NEB part the role of participant and spectator were interexchanged. The sum of EBU and NEB reproduces well the experimental data of forward angles but, for the larger angles, the data are overestimated by $\sim 60\%$. We stress, however, that the ^{3}He yield is much smaller than that for ^{4}He and uncertainties in our calculations, might lead to larger relative errors for the former case.

We have also compared the experimental and calculated energy distribution of α and ^{3}He fragments. This is shown in Fig 3.29 (a) and (b) for ^{4}He and ^{3}He, respectively. The dotted and dashed histograms

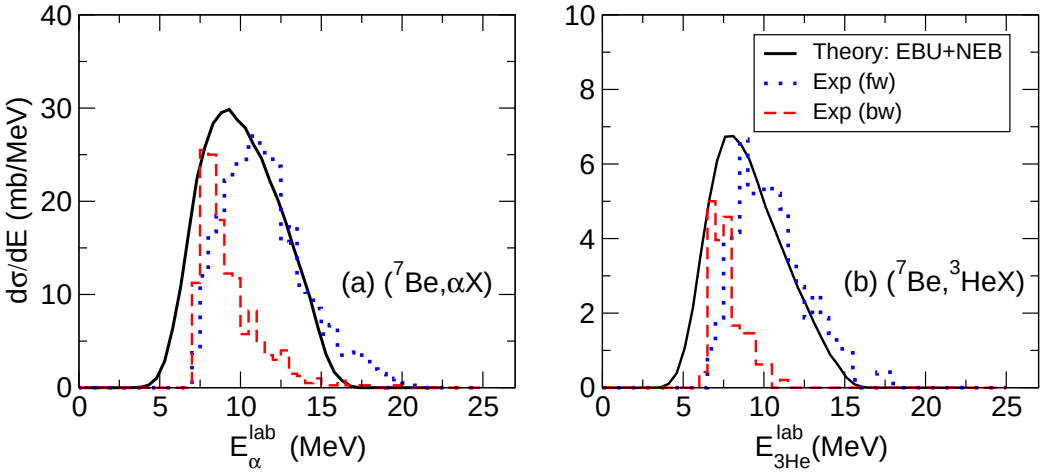

Figure 3.29: Experimental and calculated inclusive α (a) and ^{3}He (b) produced in the reaction ^{7}Be + ^{58}Ni at energies of 21.5 MeV. The solid line is the sum of EBU (CDCC) and NEB (DWBA) see test for details. The dotted and dashed histograms are respectively corresponding to the events detected at forward and backward angles Ref.[99] arbitrarily normalized to approximately match the maximum of the calculation.

depict the spectra at forward and backward angles, respectively. Since the experimental spectra are given in counts, they were arbitrarily normalized for a better comparison with the theoretical curves. The overall trend of the data is well reproduced. It is also apparent that the fragments with outgoing energies below a certain threshold ($E_{^4\mathrm{He}} < 7.3$ MeV and $E_{^3\mathrm{He}} < 6.6$ MeV) were not detected, as it is indeed explained in Ref.[99]. These low-energy fragments contribute mostly at large angles and this might explain part of the overestimation found for the ^{3}He particles.

We have tried to elucidate the origin of the dominance of the ^{4}He yield over the ^{3}He yield. In general, the fragment with larger penetrability is expected to interact stronger with the target nucleus and, hence, to have a larger non-elastic breakup cross section. However, in this particular case, the two fragments have the same charge and similar masses, so they will have similar penetrabilities. Another aspect to be considered is the fact that the ^{4}He nucleus is a compact system, and will not be broken or excited by the target. By contrary, non-elastic channels channels are expected to be more relevant in the ^{3}He+^{58}Ni case. In particular, the neutron pickup channel is expected to be very important.

These arguments suggest that the ^{3}He+^{58}Ni system will have a larger reaction cross section as compared to the ^{4}He+^{58}Ni system for the relevant kinetic energies. To verify this, we have computed the corresponding reaction cross sections as a function of their corresponding ^{3}He and ^{4}He incident energies. This is shown in Fig.3.30, where these reaction cross sections are indicated by solid and dotted lines, re-

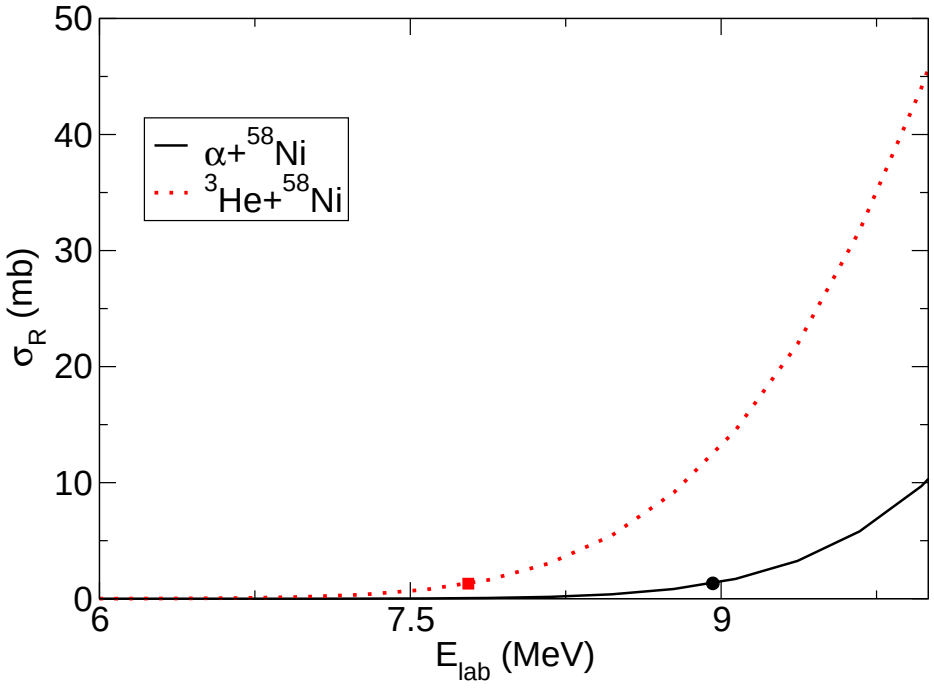

Figure 3.30: Calculated reaction cross section of $\alpha/^3$He + ^{58}Ni as function of incident energy in lab frame.

spectively. In each case, the circle corresponds to the average incident energy for each fragment (i.e. $3/7$ and and $4/7$ of the incident energy, respectively). As anticipated, it is seen that the reaction cross section is significantly larger for the ^{3}He projectile, and this should explain, at least partially, the dominance of the (^{7}Be,^{3}HeX) channel.

3.6 (^{8}B,^{7}Be X)

We consider now the case of the ^{7}Be production in reactions with the proton halo nucleus ^{8}B. The valence proton has dominant $p_{3/2}$ configuration and hence this is another example of $l_{bx} \neq 0$. In particular, we investigate the reaction ^{58}Ni(^{8}B,^{7}BeX) at $E_{lab} = 25.8$ MeV for which experimental data exit[131,87].

In the CDCC calculation, the ^{8}B is treated in a ^{7}Be$-p$ two-cluster model, assuming a pure $p_{3/2}$ configuration for the ground state. For simplicity, the ^{7}Be intrinsic spin was neglected. The $p-^7$Be binding potential was taken from Esbensen and Bertsch[44]. The potential used to construct the bin states was the same (real) potential as used to bind the ^{8}B ground state. The ^{7}Be$-p$ partial waves were needed up to $\ell = 4$ with bins extending up to $\varepsilon_{max} = 8$ MeV to obtain converged results for these three-body observ-

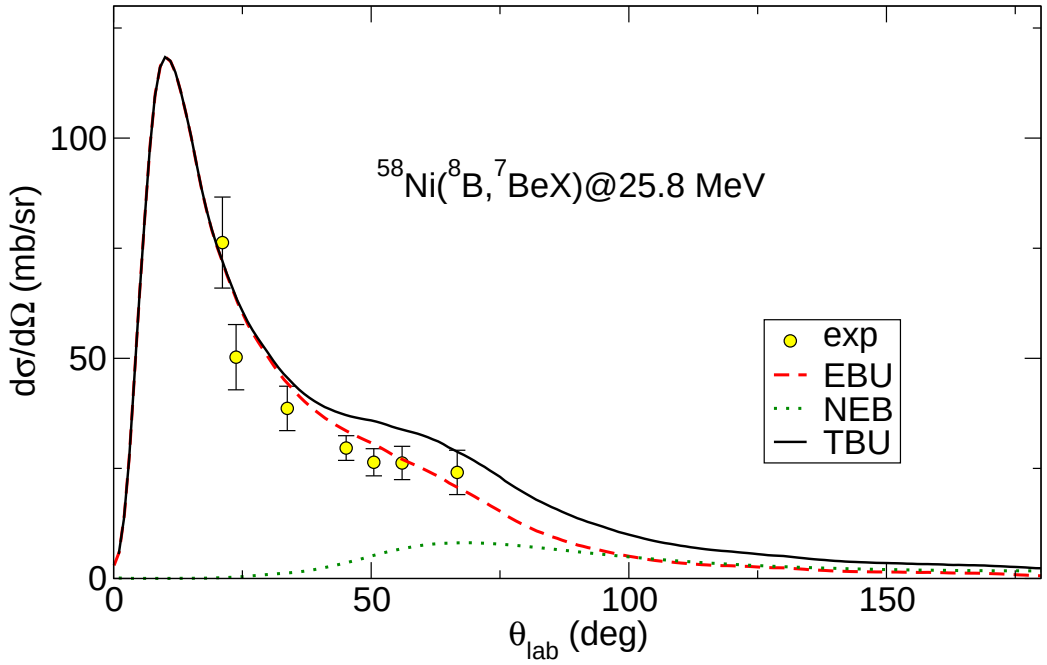

Figure 3.31: The calculated and experimental laboratory-frame 7Be cross section angular distribution following the breakup of 8B on 58Ni at 25.8 MeV. The dashed, dotted and solid lines are respectively, the EBU (CDCC), NEB (DWBA) and their sum. The experimental data was taken from [131,87]

ables. For the ^{7}Be−^{58}Ni system, the interaction of Moroz *et al.* [101] was used, as in the earlier analysis [131]. The p−^{58}Ni potential is taken from the global parametrization of Koning and Delaroche [88]. For the NEB calculation , the optical potential of ^{8}B+^{58}Ni was taken from Ref. [1].

Fig. 3.31 shows the calculated and experimental ^{7}Be cross section angular distribution following the breakup of ^{8}B on ^{58}Ni at 25.8 MeV. The dashed, dotted and solid lines are respectively, the EBU (CDCC), NEB (DWBA) and their sum. It can be seen that the calculated result gives an overall good agreement with the experimental data [131,87]. Similar to the halo nucleus case of ^{11}Be, the inclusive breakup is dominated by the EBU part, whereas the NEB part gives a small contribution and is negligible at small angles. This can be understood within a semi-classical picture by noting that these small angles will correspond to distant trajectories. However, according to Eq. (2.24), the NEB is only effective for distances within the range of the proton-target imaginary potential and hence it will be very small for these distant trajectories. For the backward angles, the NEB part is comparable to the EBU part.

Fig. 3.32 shows the calculated breakup energy distributions of the ^{7}Be fragments, together with the data from Refs. [131,87], for four measured laboratory angles. For the smallest angle ($\approx 20°$), the data are

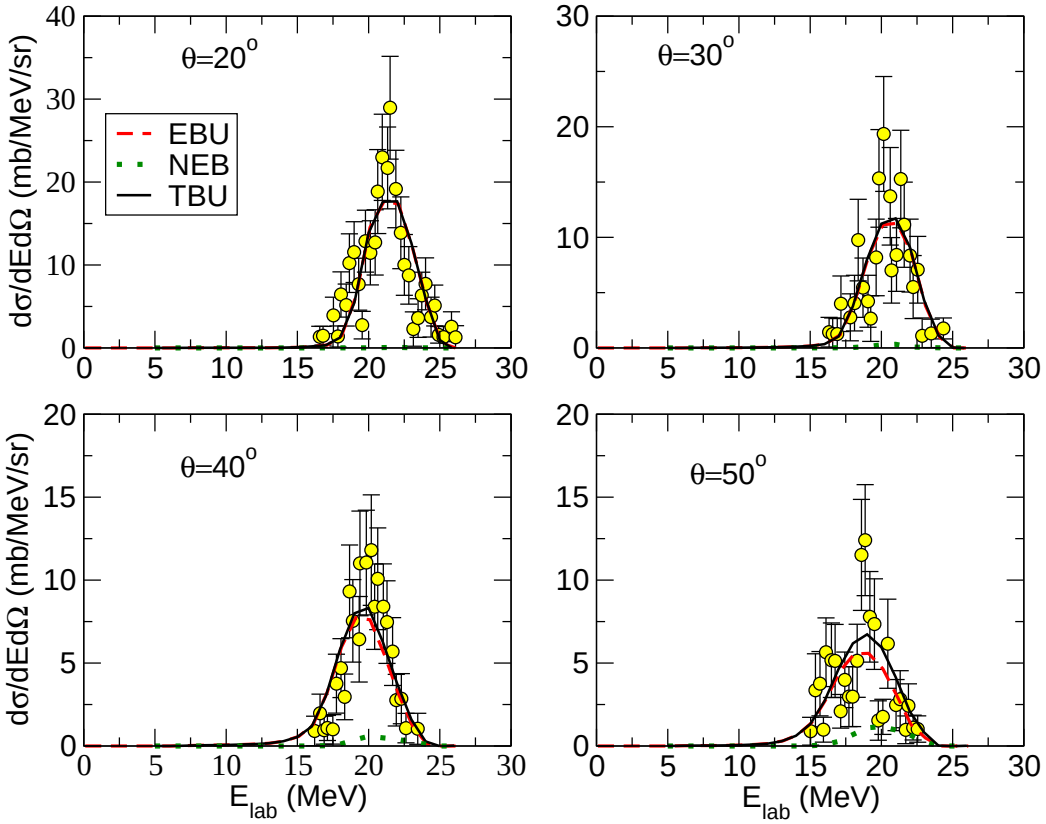

Figure 3.32: Experimental and calculated inclusive ^{7}Be energy distribution produced in the reaction ^{8}B + ^{58}Ni at energies of 25.8 MeV for the laboratory angles indicated. The dashed, dotted and solid lines are respectively, the EBU (CDCC), NEB (DWBA) and their sum. The experimental data were taken from [131,87].

the average of the distributions at $\theta_{\rm lab} = 19^\circ$ and $\theta_{\rm lab} = 21^\circ$. For the largest angles, $\theta_{\rm lab} = 50^\circ$, the curves and data are similarly the average of the distributions obtained at $\theta_{\rm lab} = 50^\circ$ and $\theta_{\rm lab} = 60^\circ$. The solid curves are the sum of EBU (dashed lines) and NEB (dotted lines). The general features of the data, their magnitude, centroids, and widths, are well described by the calculations. As discussed above, the EBU component dominates the TBU, whereas the NEB part is relatively small. Although a full understanding of this result would require additional calculations, we may speculate that, for a proton participant, the NEB will be suppressed compared to a neutron case due to the repulsive effect of the proton-target interaction.

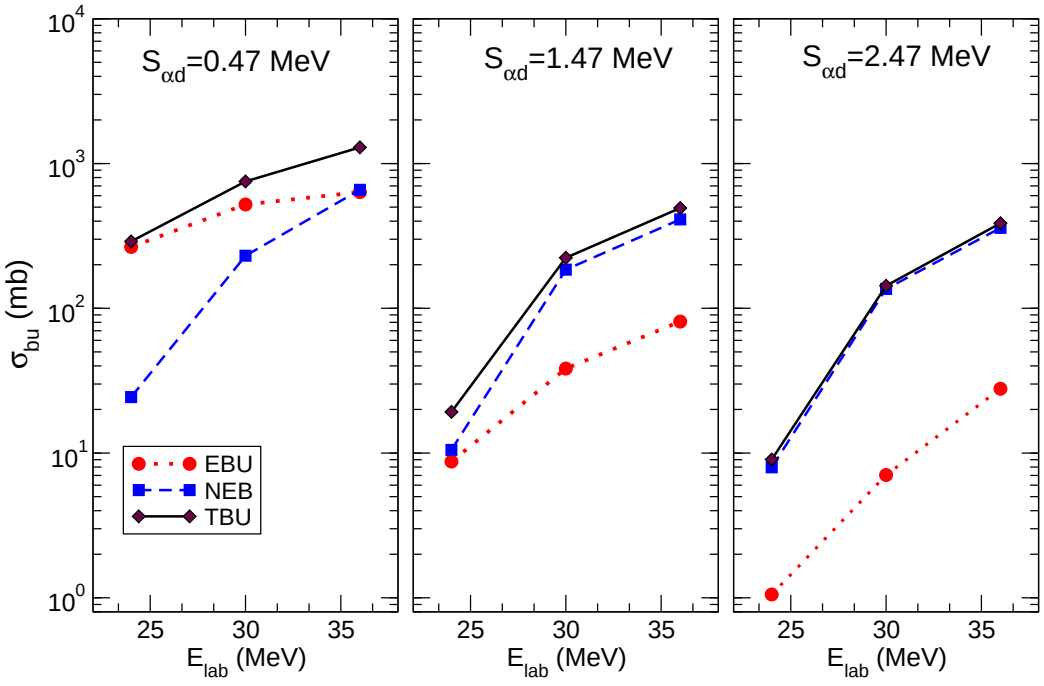

Figure 3.33: Elastic (EBU), non-elastic (NEB) and total breakup (TBU=EBU+NEB) cross sections for the ^{209}Bi (^{6}Li, αX) reaction as a function of the ^{6}Li incident energy, and for three different values of the separation energy of ^{6}Li.

3.7 Influence of the separation energy and the incident energy on the EBU and NEB

As we have discussed above, for the weakly bound nuclei, such as deuteron, ^{6,7}Li and ^{7}Be, the NEB part dominates the TBU. It is nevertheless expected that the relative importance of EBU versus NEB will depend on several factors, such as the target mass/charge (see details in Sec. 3.2.7), the separation energy of the projectile and the incident energy. For example, in the scattering of halo nuclei, such as ^{11}Be and ^{8}B, on heavy targets, long-range Coulomb couplings favor the distant breakup of the projectile thus enhancing the EBU component over the NEB one. The effect has been found to be particularly remarkable at energies around and below the Coulomb barrier (see details in Sec. 3.6 and Sec. 3.3). One may expect that, as the incident energy decreases, the EBU component will become progressively more important as compared to the NEB part, because the breakup will occur at larger distances, thus suppressing the absorption of the x+target system. Taking ^{6}Li + ^{209}Bi reaction system as an example, we have studied this dependence by performing calculations at three incident energies, one below, one around and one above the Coulomb barrier ($V_b \approx 30.1$ MeV). Simultaneously, we have also studied the dependence on

the binding energy by varying artificially the separation energy of the ^{6}Li nucleus ($S_{\alpha d}$). The results are presented in Fig. 3.33 for the ^{209}Bi (^{6}Li, αX) reaction. The left, middle and right panels correspond to the binding energies $S_{\alpha d}$=0.47 MeV, 1.47 MeV (the physical one) and 2.47 MeV, respectively. In each panel, the EBU, NEB and TBU cross sections are displayed as a function of the incident energy.

It is seen that the EBU depends strongly on the separation energy, decreasing by $\sim 1-2$ orders of magnitude when the latter is artificially increased from 0.47 MeV to 2.47 MeV. By contrast, the NEB breakup shows a moderate reduction with this variation of binding energy. As a consequence, the relative importance of EBU versus NEB varies drastically with the separation energy. For $S_{\alpha d}$=1.47 MeV and 2.47 MeV, the TBU is largely dominated by the NEB component, whereas for $S_{\alpha d}$=0.47 MeV (typical of halo nuclei), the EBU component dominates. This different behavior of the EBU and NEB components can be understood as follows. The EBU is a peripheral process and thereby highly sensitive to the tail of the $\alpha-d$ wave function. Since the magnitude of the wave function at large distances is mostly determined by the separation energy of the two clusters, it is conceivable that the EBU is reduced as the binding energy is increased. On the contrary, Eq. (2.24) indicates that the NEB component depends on the internal region, and will be therefore sensitive to the overall size of the projectile and target, being therefore less sensitive to the change in the tail of the $\alpha-d$ relative wave function.

Regarding the dependence on the incident energy shown in Fig. 3.33, for the physical separation energy (middle panel), the NEB largely dominates at energies around and above the barrier, and the EBU only becomes competitive at energies well below the barrier, for which the breakup is expected to occur at large projectile-target separations, and the absorptive effect of the d+target interaction will be less effective. For the more weakly-bound case (left panel) the EBU and NEB contributions turn out to be similar above the barrier but, as the incident energy decreases, the NEB drops faster than the EBU, making the latter dominant. This result corroborates the dominance of EBU observed in breakup experiments with halo nuclei (Sec. 3.3 and Sec. 3.6). Conversely, for the tightly bound case (right panel), the NEB dominates in the whole energy range.

These results confirm the strong sensitivity of the relative importance of EBU and NEB on the incident energy as well as on the separation energy. In particular, for halo nuclei, we expect a dominance of EBU at energies around and below the barrier, whereas for tightly bound nuclei we expect a dominance of NEB for all energies.

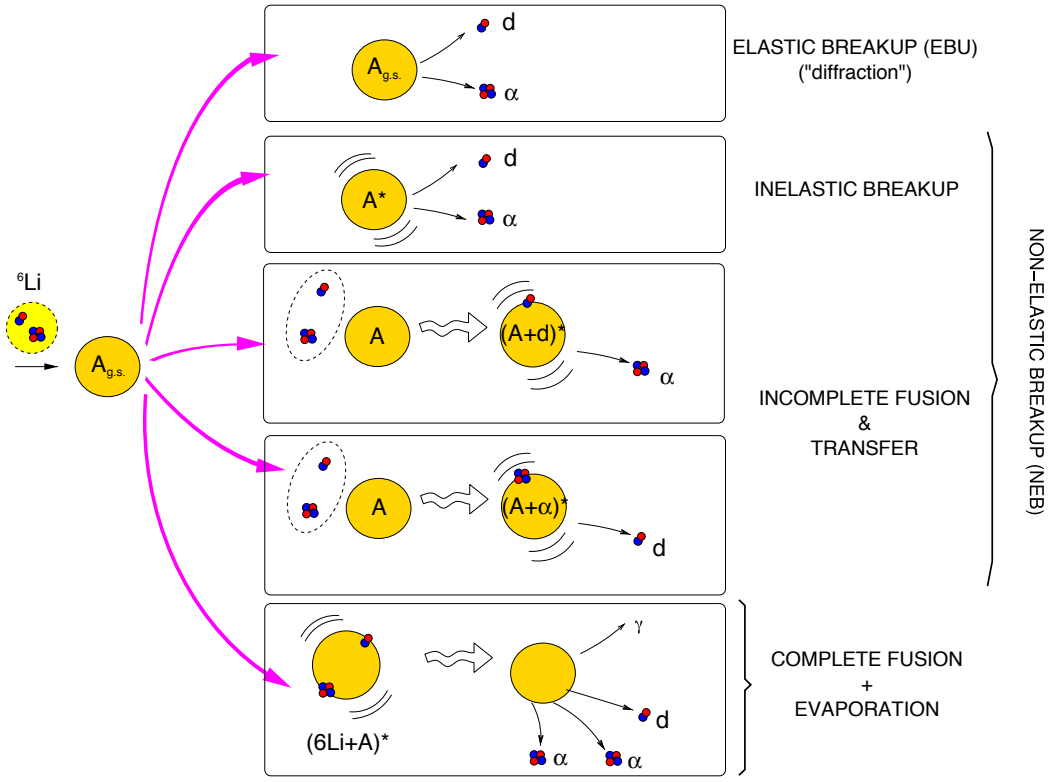

Figure 3.34: Two-body projectile reaction modes for the ^{6}Li + A system.

3.8 Reaction modes and reaction cross section of ^{6}Li + ^{209}Bi

For a weakly bound nucleus, it is expected that breakup contributes a significant fraction of the reaction cross section. We have investigated this in a quantitative way for the ^{6}Li+^{209}Bi reaction. For example, for the two-body projectile using the notation introduced above, the reaction can be represented as $a+A \rightarrow X$, where X is any possible configuration of the $b+x+A$ system. The main contributing processes will be the following:

(i) The *elastic breakup* process (EBU), in which the three outgoing particles are emitted in their ground state, i.e., $a+A \rightarrow b+x+A_{\rm gs}$.

(ii) Inelastic breakup (INBU), in which the breakup is accompanied by the excitation of some of the fragments. For example, if the target is excited, $a+A \rightarrow b+x+A^{*}$, whereas if the core particle is excited, $a+A \rightarrow b^{*}+x+A_{\rm gs}$.

(iii) Particle transfer, leading to the bound states of the $A+x$ system, i.e., $a+A \rightarrow b+B$ ($B \equiv A+x$), or the bound states of the $A+b$ system, i.e., $a+A \rightarrow x+B$ ($B \equiv A+b$)

(iv) Incomplete fusion (ICF), in which the fragment x is absorbed by the target, forming a compound nucleus C, which will eventually decay by particle or gamma-ray emission: $a+A \rightarrow b+C$, or the fragment b is absorbed by the target, forming a compound nucleus C, which will eventually decay by particle or gamma-ray emission: $a+A \rightarrow x+C$

(v) Complete fusion (CF) followed by evaporation. We include also in this category the preequilibrium (PE) processes.

In Fig. 3.34, these processes are schematically depicted for a ^{6}Li+A reaction (assuming a two-body dissociation ^{6}Li$\rightarrow\alpha$+d).

The EBU cross sections [process (i)], can be obtained with the CDCC framework, as we have done in the calculation presented in Sec. 3.2.1.

The calculation of INBU, process (ii), has been less explored in the literature. In the case of target excitation, this was done by the Kyushu group in the early days of the CDCC method[143] for the case of deuteron scattering, with the aim of comparing the relative importance and mutual influence of target-excitation and deuteron breakup in elastic and inelastic scattering of deuterons. Process (iii), i.e., transfer of x to bound states of A, has been traditionally treated within the DWBA method[119]. For weakly-bound projectiles, the coupling to the breakup channels becomes important, and this effect is known to affect the transfer cross sections. This effect can be incorporated using the adiabatic distorted wave model of Johnson and Soper (ADWA)[77] and more elaborate versions of it (e.g.[76]). A recent review of these theories can be found in Ref.[20].

The process (iv), ICF, is very challenging from the theoretical point of view to the extent that, at present, no fully-quantum mechanical theory exists to calculate ICF cross sections. For this reason, alternative methods, based on semiclassical ideas, have been proposed in the literature[96,39,37]. Moreover, from the experimental point of view, the identification of this process is not without its difficulties since, many times, the products coincide with those produced in the transfer reactions.

Processes (ii)-(iv) correspond to the NEB, as defined in Chapter 1 and evaluated with the IAV, Eq. 2.24, in our calculation.

Process (v) is qualitatively different from the previous ones, because it takes place via the formation of a compound nucleus, rather than via a direct process. The calculation of detailed cross sections, as a

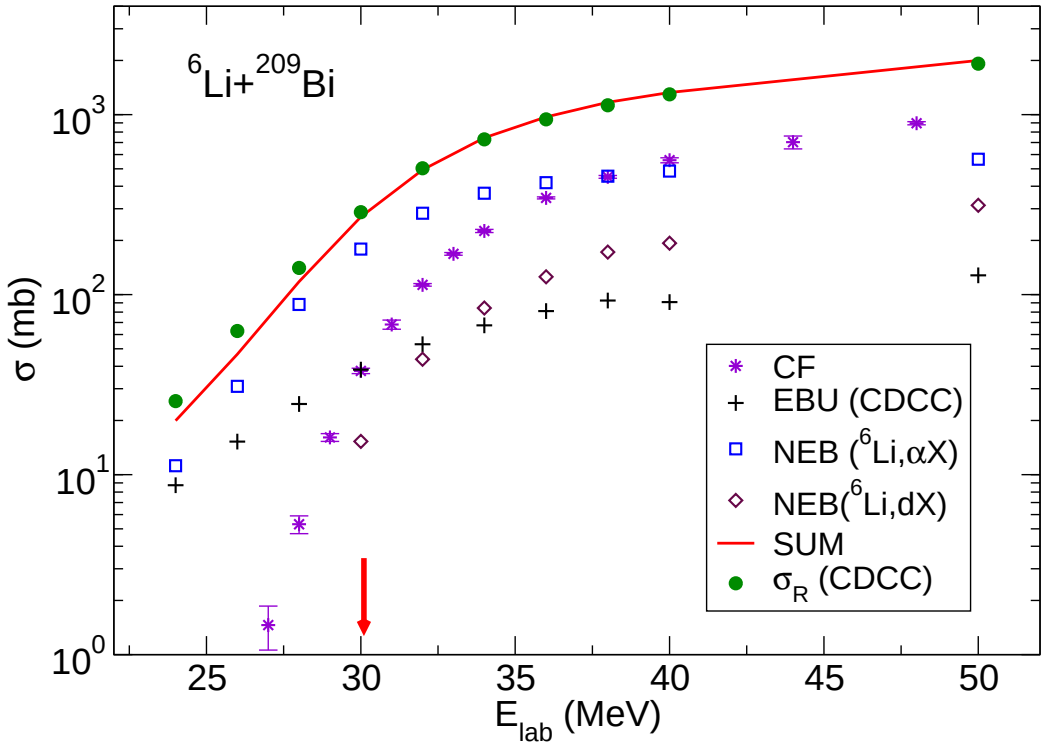

Figure 3.35: Decomposition of the reaction cross section for the ^{6}Li+^{209}Bi reaction at several incident energies. The pluses, squares, diamonds and stars are respectively, elastic breakup, nonelastic breakup for α as a spectator, nonelastic breakup for d as a spectator and the complete fusion which were taken from Ref. [32]. Their sum (solid line) is remarkably close to the reaction cross sections which obtained from the CDCC calculations. The arrow indicates the nominal position of the Coulomb barrier.

function of the angle/energy of the outgoing particles, requires the use of statistical models, first proposed by Bohr [12], and whose modern formulation can be found in many textbooks [129].

According to the previous discussion the reaction cross section for two-body projectile reaction system can be written as

$$\sigma_R = \sigma_{\mathrm{CF}} + \sigma_{\mathrm{EBU}} + \sigma^{(b)}_{\mathrm{NEB}} + \sigma^{(x)}_{\mathrm{NEB}}. \tag{3.1}$$

where $\sigma^{(b)}_{\mathrm{NEB}}$ is the part of the NEB cross section observing b particle and $\sigma^{(x)}_{\mathrm{NEB}}$ is the part of the NEB cross section observing x particle. Here the ^{6}Li + ^{209}Bi reaction was taken as an example to investigate decomposition of the reaction cross sections. This is shown in Fig. 3.35 for different incident energies. The crosses, squares and diamonds are, respectively, the cross sections of elastic breakup, nonelastic breakup for α as a spectator, nonelastic breakup for d as a spectator. For completeness, we include also the experimental CF cross section reported by Dasgupta *et al.* [32]. The sum of these contributions is

compared at each energy with the reaction cross section, obtained from the CDCC calculation. It is seen that the sum EBU+NEB+CF is remarkably close to the reaction cross section.

This is a very interesting result which suggests that the reaction cross section for this reaction is well exhausted by the sum of the breakup modes considered here, plus the CF cross section. Other contribution to the reaction cross section, such as pure target excitations (not accompanied by projectile breakup) are small in this case.

The situation may be of course qualitatively different for other systems. Although it is our purpose to extend our study to other projectiles and/or targets, we have not been able to accomplish this before the submission of this dissertation, and the study is differed for the future.

In this Chapter, we have we have compared the IAV model with inclusive breakup data for reactions induced by several weakly bound nuclei, including the halo nuclei ^{11}Be and ^{8}B. Our results can be summarized as follows:

- Overall, our calculations show a very encouraging agreement with the data, which reinforces the validity of the IAV model.
- For the non-halo systems, the have found that the inclusive breakup data is dominated by non-elastic breakup channels. In particular, this result explains why the alpha production yields reported in ^{6}Li and ^{7}Li reactions are largely overestimated the CDCC calculations, since the latter method accounts only for the EBU part.
- Despite the dominance of NEB for the non-halo nuclei (d, ^{6}Li, ^{7}Li, ^{7}Be), we have found that the relative importance of EBU and NEB depends on several structure and dynamical factors, such as the projectile binding energy, and the incident energy. For example, at sub-Coulomb energies the EBU becomes progressively more important as compared to the NEB part.
- For the halo nuclei studied here (^{11}Be, ^{8}B), the EBU is found to be dominant, at least for the targets and energies considered in our analysis.

In the following Chapter, we will address the problem of the post-prior equivalence in inclusive breakup reactions induced by weakly bound nuclei.

Physics depends on a universe infinitely centred on an equals sign.

Mark Z. Danielewski

4

Post-Prior Equivalence

In the introductory chapter, we saw that there was an intense activity in the 1980s by several theoretical groups with the aim of developing appropriate theories for the evaluation of inclusive breakup cross sections[5,9,17,67,71,79,121,135,137]. This research was leaded by two main groups, the group of Austern, Ichimura and Vincent (IAV), on one side, and the group of Tamura and Udagawa (UT).

In the preceding chapters, we have implemented and applied extensively the IAV model. However, as pointed out in the introductory chapter, there was a long-standing debate between these two groups regarding the validity of their respective models. In this chapter we explain in more detail the formal differences of these two models and we compare them numerically for some practical cases.

From the formal point of view, the main difference between the two models is that the IAV uses the post-form representation of the transition amplitude, whereas UT used the prior-form representation. This is in contrast to the DWBA formula for transfer between bound states, where it is well known that the post and prior formulas are fully equivalent. This discrepancy led to a long-standing controversy between these two groups, which lasted for more than a decade. The heart of the discussion was the fact that the transformation of the post form DWBA expression of IAV to its prior form gave rise to additional terms,

not present in the UT prior formula (see Sec. 1.2.5). These additional terms guaranteed the post-prior equivalence for NEB, but they were nevertheless regarded as unphysical terms by UT. To support their conclusions, UT performed calculations for several inclusive reactions[93,97], in which they showed that the IAV calculations largely overestimated the data.

This result is at variance with the numerical results presented in the previous chapters, where we have shown that the IAV model gives a very reasonable account of inclusive experimental data for most of the reactions analysed in this work. Moreover, recent calculations performed by other groups, using also the IAV model[27,112], show also a good agreement with the data. To clarify the situation, we have compared these two models, performing calculations for the same reaction, and comparing with experimental data. For a meaningful comparison, we have used the same input ingredients (e.g. potentials) in the two models. As an additional motivation, with this study we aim at obtaining a better understanding of the post-prior equivalence in the context of inclusive breakup reactions, both at a formal as well as at a numerical level.

Before presenting the numerical results, we briefly recall the main differences between the two formulations.

4.1 The post-prior formulas

Using the post-form DWBA, the inclusive breakup differential cross section, as a function of the detected angle and energy of the fragment b, is given by

$$\frac{d^2\sigma}{d\Omega_b dE_b} = \frac{2\pi}{\hbar v_a}\rho(E_b)\sum_c |\langle \chi_b^{(-)}\Psi_{xA}^{c,(-)}|V_{\rm post}|\chi_a^{(+)}\varphi_a\varphi_A^0\rangle|^2\delta(E-E_b-E^c), \tag{4.1}$$

where $V_{\rm post} \equiv V_{bx} + U_{bA} - U_{bB}$ is the post-form transition operator, $\rho_b(E_b) = k_b\mu_b/((2\pi)^3\hbar^2)$ (with μ_b the reduced mass of $b+B$ and k_b their relative wave number) , $\varphi_a(\vec{r}_{bx})$ and φ_A^0 are the projectile and target ground-state wave functions, $\chi_a^{(+)}$ and $\chi_b^{(-)}$ are distorted waves describing the $a-A$ and $b-B$ relative motion, respectively, and $\Psi_{xA}^{c,(-)}$ are the eigenstates of the $x+A$ system, with $c=0$ denoting the x and A ground states. Thus, for $c=0$ this expression gives the EBU part, whereas the terms $c\neq 0$ give the NEB contribution.

The theory of IAV allows to perform the sum in a formal way, making use of the Feshbach projection

formalism and the optical model reduction, leading to a closed form for the NEB differential cross section:

$$\left.\frac{d^2\sigma}{dE_b d\Omega_b}\right|_{\rm NEB}^{\rm IAV} = -\frac{2}{\hbar v_a}\rho_b(E_b)\langle\psi_x^{\rm post}|W_x|\psi_x^{\rm post}\rangle, \tag{4.2}$$

where W_x is the imaginary part of the optical potential U_x, which describes $x+A$ elastic scattering. The function $\psi_x^{\rm post}(\vec{r}_x)$ (the x-channel wave function hereafter) describes the $x-A$ relative motion when the target is in the ground state and the b particle scatters with momentum $\vec{k}_b$, and is obtained by solving the inhomogeneous equation

$$(E_x^+ - K_x - U_x)\psi_x^{\rm post}(\vec{r}_x) = (\chi_b^{(-)}|V_{\rm post}|\chi_a^{(+)}\varphi_a\rangle, \tag{4.3}$$

where $E_x = E - E_b$ and $V_{\rm post} \equiv V_{bx} + U_{bA} - U_{bB}$.

Udagawa and Tamura[137] derived a very similar formula for the same problem, but making use of the prior form. Their final result is formally identical to Eq. (4.2), but with the x-channel wave function given by $\psi_x^{\rm prior}$, which is a solution of

$$(E_x^+ - K_x - U_x)\psi_x^{\rm prior}(\vec{r}_x) = (\chi_b^{(-)}|V_{\rm prior}|\chi_a^{(+)}\varphi_a\rangle, \tag{4.4}$$

with $V_{\rm prior} \equiv U_{xA} + U_{bA} - U_{aA}$.

Despite their formal analogy, the UT and IAV expressions lead to different predictions for the NEB cross sections. An important result to understand the connection between these two expressions is the relation[93]

$$\psi_x^{\rm post} = \psi_x^{\rm prior} + \psi_x^{\rm no}, \tag{4.5}$$

where

$$\psi_x^{\rm no}(\vec{r}_x) = \langle\chi_b^{(-)}|\chi_a^{(+)}\varphi_a\rangle, \tag{4.6}$$

is the so-called non-orthogonality (NO) overlap.

Replacing Eq. (4.6) into Eq. (4.2) one gets

$$\left.\frac{d^2\sigma}{dE_b d\Omega_b}\right|_{\rm NEB}^{\rm IAV} = \left.\frac{d^2\sigma}{dE_b d\Omega_b}\right|_{\rm NEB}^{\rm UT} + \left.\frac{d^2\sigma}{dE_b d\Omega_b}\right|_{\rm NEB}^{\rm NO} + \left.\frac{d^2\sigma}{dE_b d\Omega_b}\right|_{\rm NEB}^{\rm IN}, \tag{4.7}$$

where we have introduced the NO *cross section*

$$\left.\frac{d^2\sigma}{dE_b d\Omega_b}\right|_{\rm NEB}^{\rm NO} = -\frac{2}{\hbar v_a}\rho_b(E_b)\langle\psi_x^{\rm no}|W_x|\psi_x^{\rm no}\rangle, \tag{4.8}$$

and the interference (IN) term

$$\left.\frac{d^2\sigma}{dE_b d\Omega_b}\right|_{\rm NEB}^{\rm IN} = -\frac{4}{\hbar v_a}\rho_b(E_b){\rm Re}\langle\psi_x^{\rm prior}|W_x|\psi_x^{\rm no}\rangle. \tag{4.9}$$

Equation (4.7) represents the post-prior equivalence of the NEB cross sections in the IAV model, with the RHS corresponding to the prior-form expression of this model. The first term is just the UT formula, which is formally analogous to the IAV post-form formula (4.2), but with the x-channel wave function given by $\psi_x^{\rm prior}(\vec{r}_x)$. The two additional terms, which are responsible for the discrepancy of the IAV and UT results, arise from the NO overlap. These terms ensure the post-prior equivalence of the NEB cross sections. However, UT considered that these two additional terms are unphysical and hence that the post-prior equivalence does not hold for the NEB. We note here that this problem does not hold for the EBU part, for which the post and prior formulas are well known to give identical results[71]. To support their interpretation, Mastroleo, Udagawa and Tamura[97] performed calculations for the reactions ^{58}Ni(α,pX) at $E_\alpha = 80$ MeV and ^{62}Ni(d,pX) at $E_d = 25.5$ MeV. In both cases, they found that the sum of the EBU (calculated with DWBA) and the NEB (calculated with the IAV model) overestimates the data. This result was interpreted as evidence for the failure of the IAV model, and support for the UT theory.

This interpretation was later questioned in subsequent works by Ichimura *et al.*[72,73,70] and also by Hussein and co-workers[66]. These works clearly demonstrated that the UT formula provides only the so-called *elastic breakup fusion* component, which corresponds to breakup without simultaneous excitation of the target A by the interaction U_{xA}, and that the prior-post equivalence does indeed hold for inclusive processes as well.

In the following section, we apply the IAV and UT models to specific reactions comparing, in the former, the prior and post results.

4.2 Post-prior equivalence for the $x-A$ channel wave function

The relation between Udagawa and Tamura (UT) model and Ichimura, Austern and Vincent (IAV) model has been discussed in the previous section. The relation of the IAV and UT model for the $x-A$ channel

wave function is given by Eq. (4.5). It should be noted that $\psi_x^{\rm no}(\vec{r}_x)$ is long ranged and behaves as $\mathcal{O}(1/r_x^2)$ for $r_x \to \infty$. To overcome this long range behaviour, the energy *binning* procedure introduced in Sec. 2.4 and applied in the calculations of Chapter 3 is used here. With the finite range partial wave expansion Eq. (2.39), the radial part of Eq. (1.58) can be rewritten as

$$\mathfrak{R}^{l_a l_b}_{l l_x}(r_x)\Big|^{\rm post} = \mathfrak{R}^{l_a l_b}_{l l_x}(r_x)\Big|^{\rm prior} + \mathfrak{R}^{l_a l_b}_{l l_x}(r_x)\Big|^{\rm no}. \tag{4.10}$$

For the UT model, the $x-A$ channel partial wave function $\mathfrak{R}^{l_a l_b}_{l l_x}(r_x)\Big|^{\rm prior}$ can be calculated with the exact the same formula as $\mathfrak{R}^{l_a l_b}_{l l_x}(r_x)\Big|^{\rm post}$, but changing the interaction form from $V_{\rm post}$ to $V_{\rm prior}$, and the non-orthogonality term (NO) is calculated as:

$$\mathfrak{R}^{l_a l_b}_{l l_x}(r_x)\Big|^{\rm no} = \rho^{l_a l_b}_{l l_x}(r_x)\Big|^{\rm no}, \tag{4.11}$$

where $\rho^{l_a l_b}_{l l_x}(r_x)\Big|^{\rm no}$ is nothing, but Eq. (2.38) by setting the interaction $V_{\rm post} = 1$.

As an example, the reaction ^{93}Nb(d,pX) at an incident energy of 25.5 MeV was considered. The details about the interaction potentials can be found in Sec. (3.1.1). We recall that the post-form expression has a marginal convergence, due to the oscillatory behaviour of the source term. To overcome this problem, in the present calculations we resort to the binning procedure used in the calculations presented in Chapter 3. Although this stabilization procedure is not needed in the prior-form method, we use the same averaged χ_b distorted waves in this case, in order to have a meaningful comparison of the two methods. Fig. (4.1) shows the comparison of the x channel wave function $\mathfrak{R}^{l_a l_b}_{l l_x}(r_x)$ calculated with IAV and UT models, respectively, for partial wave $l_a = 5$, $l = 5$, $l_b = 0$ and $l_x = 5$. It is seen that, for both the real and the imaginary parts, the IAV and UT x-channel wave functions are similar at large distances, but they clearly differ at short distances. Addition of the NO term to the UT function, gives a result in remarkable agreement with the IAV curve. This result confirms the relation (4.10) at a numerical level.

4.3 Testing the post-prior equivalence for the ^{62}Ni(d,pX) reaction

As a first example, we consider the ^{62}Ni(d,pX) reaction. This reaction was analysed by Mastroleo, Udagawa and Tamura, leading them to the conclusion that the IAV model tended to largely overestimate the data, a result that they attributed to the presence of spurious contributions in this model. Therefore,

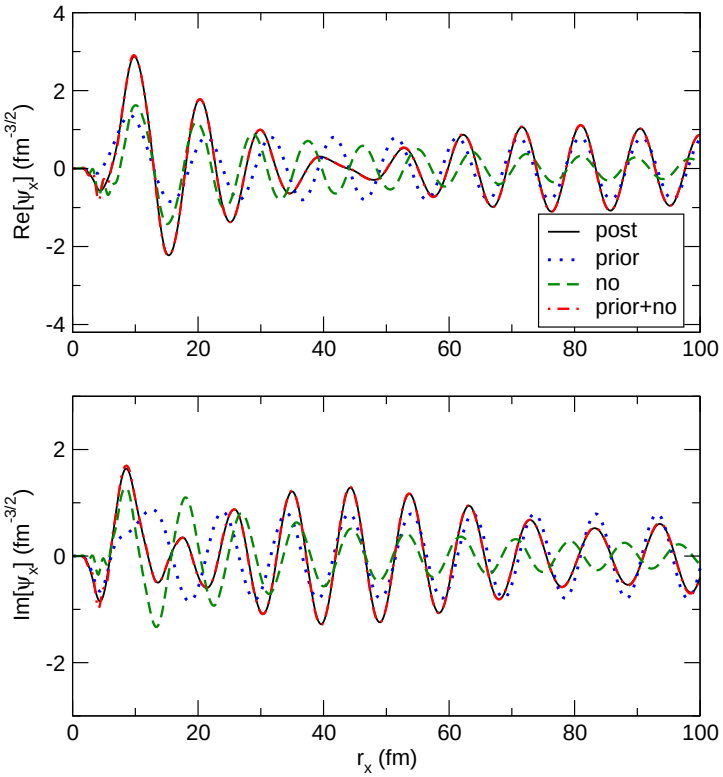

Figure 4.1: x channel wave function $\mathfrak{R}^{l_a l_b}_{l l_x}(r_x)$ for $l_a = 5, l = 5, l_b = 0$ and $l_x = 5$ of ^{93}Nb(d, pX) at incident energy of 25.5 MeV with outgoing p energy at 14 MeV. The real and imaginary parts are shown in pangels (a) and (b), respectively.

it seems timely to start reexamining these results using our implementation of the two models.

For that purpose, the reaction ^{62}Ni(d, pX) at $E_d = 25.5$ MeV, which had already been investigated in Sec. 3.1.2, has been considered. The same potentials used the calculations shown in Sec. 3.1.2 are also used here. As noted before, to evaluate the post-form formula the distorted waves χ_b are averaged over small momentum intervals. Although this procedure is not required for the prior-form formula, to have consistent ingredients in both calculations, the same averaged distorted waves were used in that case.

In Fig. 4.2 (a), the post-form IAV calculation (thick solid line) with the prior calculation (dashed line), for the angle-integrated proton energy distribution in the c.m. frame. The agreement between the prior and post calculations is seen to be very satisfactory, with only small differences possibly due to numerical inaccuracies. This agreement corroborates the post-prior equivalence at the numerical level. The choice of one or another representation becomes therefore a matter of numerical convenience. The separate contributions of the prior-form calculations (i.e., prior, NO, IN) , according to Eq. (1.59), are also shown

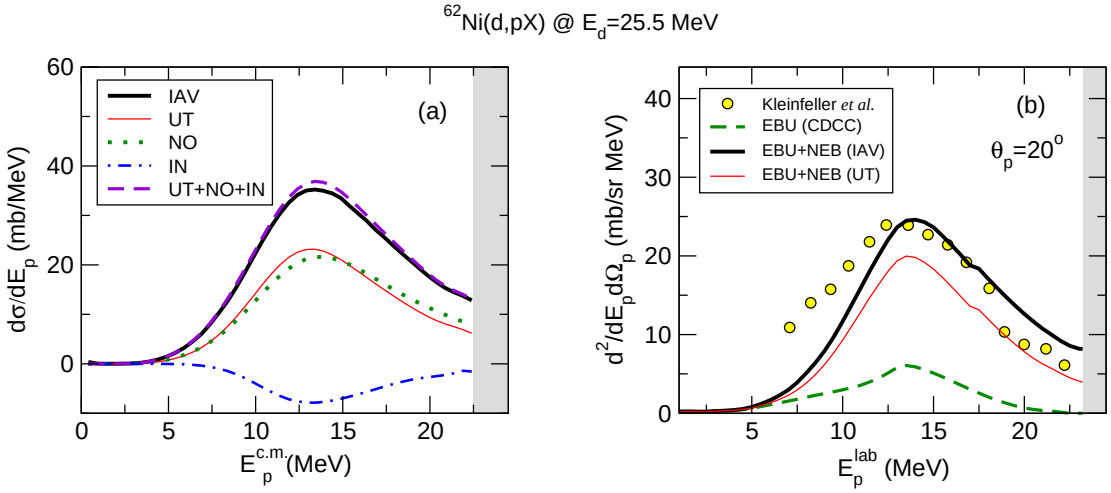

Figure 4.2: Proton energy spectra for ^{62}Ni(d,pX) at 25.5 MeV, (a) Comparison of the post and prior results; (b) Comparison of IAV and UT models with the data from Refs.[86,97], corresponding to the double differential cross section as a function of the proton energy in the laboratory frame, for $\theta_p = 20^\circ$.

in Fig. 4.2 (a). It is seen that the full IAV calculation and the UT result (thin solid line) are in clear disagreement and that the inclusion of the NO term is essential to achieve the post-prior equivalence.

In Fig. 4.2 (b), the calculations are compared with the experimental data from Refs.[86,97], corresponding to the double differential cross section as a function of the proton energy and for a proton detection angle of $\theta_p = 20^\circ$ in the laboratory frame. Note that the reaction has analyzed in Sec. 3.1.2 and here the calculation of UT model is also presented. It is seen that the sum EBU + NEB(UT), represented by the thin solid line, largely under-predicts the data. In contrast, the sum EBU + NEB(IAV) (thick solid line) reproduces reasonably well the magnitude and shape of the data, except for some underestimation at the smaller energies and some overestimation at the larger ones. It should be noticed that the low-energy tail will be mostly affected by the compound nucleus subtraction and hence some uncertainty is expected at these energies. The results shown here are in contrast with those reported in Ref.[97], who found an overestimation of the IAV model. Since we have tried to use, whenever possible, the same input ingredients as theirs, the reason for the discrepancy is unclear to us.

4.4 Testing the post-prior equivalence for the ^{209}Bi(^{6}Li,αX) reaction

As a second example, the reaction ^{6}Li+^{209}Bi, which has been analyzed in Sec. 3.2.1 using the post-form IAV formula, is considered. The calculations shown in Sec. 3.2.1 reproduced rather well the shape and

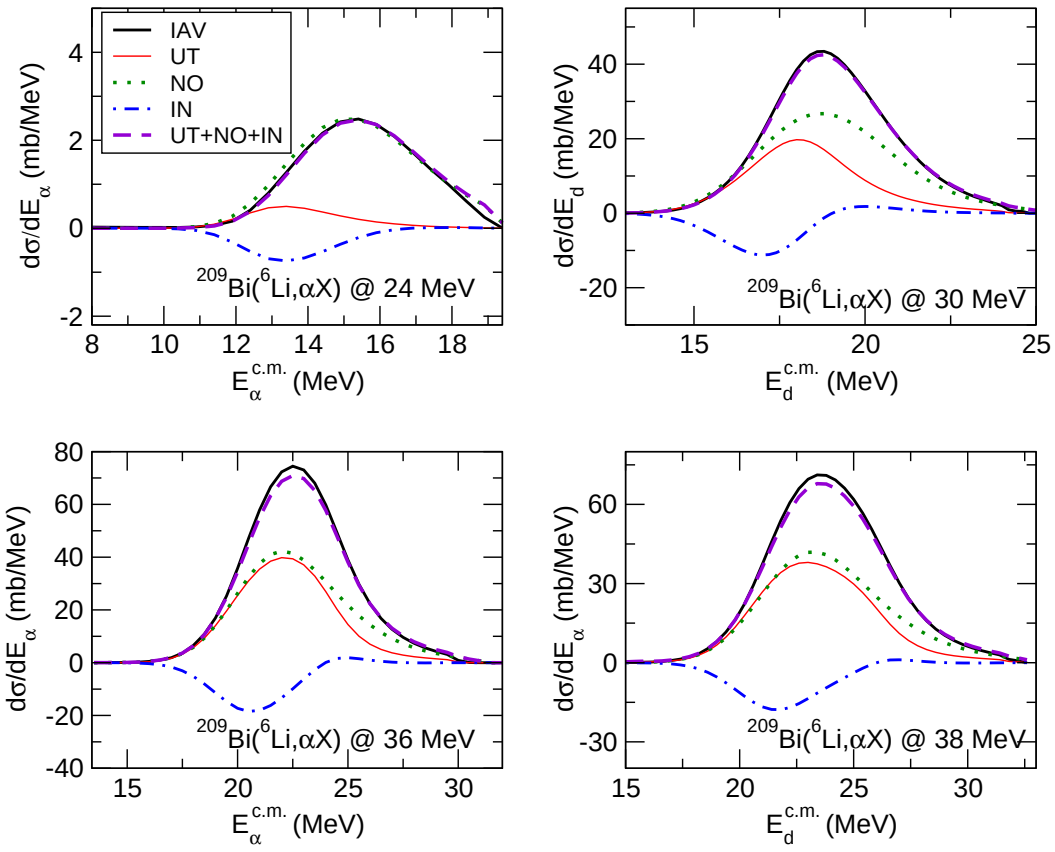

Figure 4.3: Angular-integrated energy differential cross section, as a function of the α c.m. energy, for the reaction ^{6}Li+^{209}Bi at the incident energies indicated by the labels. See text for the details.

magnitude of the experimental angular distribution of the α particles for a wide range of incident energies above and below the Coulomb barrier. To test the post-prior equivalence, several different incident energies are selected. The same potentials are employed as in Sec. 3.2.1.

The results are shown in Fig. 4.3 for the angle-integrated α energy distribution (in the c.m. frame), with the same meaning for the lines as in Fig. 4.2 (a). The results are qualitatively similar to those found in the deuteron case; namely, (i) the post-form IAV model and the prior-form UT model yield significantly different results, and (ii) the sum UT+NO+IN gives a result very close to the post-form IAV model. Thus, the post-prior equivalence is also well fulfilled in this case.

In Fig. 4.4, the calculations are compared with the data from Ref.[117], which correspond to the angular distribution of α particles in the laboratory frame. The EBU cross section corresponding to the CDCC calculation and NEB cross calculated by IAV formalism are taken from Sec. 3.2.1. The EBU+NEB(IAV)

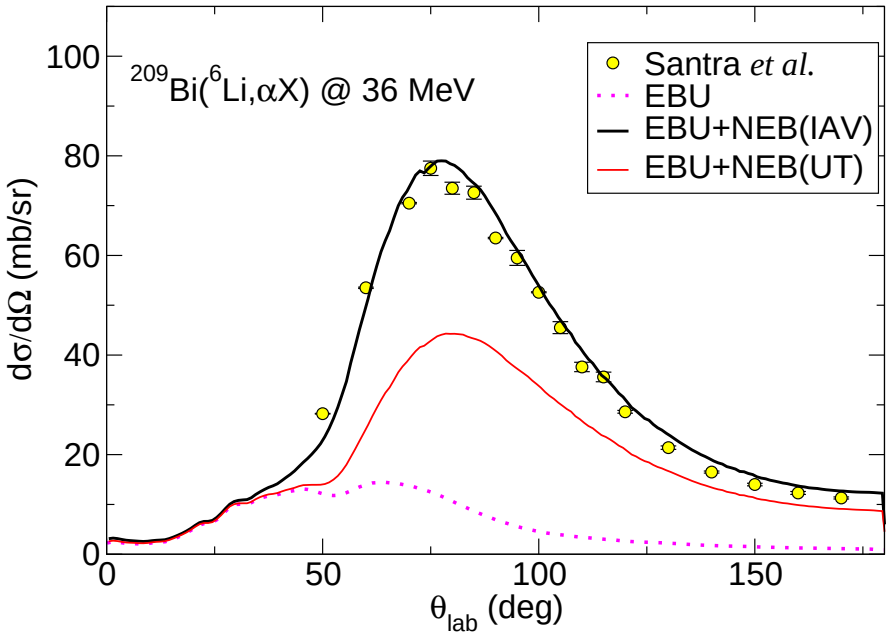

Figure 4.4: Experimental and calculated angular distribution of α particles, in the laboratory frame, for the ^{6}Li+^{209}Bi reaction at 36 MeV. The data are taken from Ref. [117].

calculation (thick solid line) reproduces remarkably well the shape and magnitude of the data. In contrast, the EBU+NEB(UT) calculation, represented by the thin solid line, clearly underestimates the data. This result reinforces the reliability of the IAV model.

In conclusion, in this chapter, we addressed the problem of the post-prior equivalence in the calculation of NEB cross sections within the closed-form DWBA models proposed in the 1980s by Ichimura, Austern, and Vincent [71] and by Udagawa and Tamura [137]. We performed calculations for the ^{62}Ni(d, pX) and ^{209}Bi(^{6}Li, αX) reactions. In both cases, we find an excellent agreement between the post and prior expressions of the IAV model, confirming this equivalence at a numerical level. Moreover, the IAV model reproduces rather well the data in both reactions. In contrast, the UT model has been found to underestimate the experimental cross sections.

The results presented in this work indicate that the IAV model provides a reliable framework to calculate NEB cross sections in reactions induced by deuteron and ^{6}Li projectiles.

Whether we like it or not, modern ways are going to alter
and in part destroy traditional customs and values.

Werner Heisenberg

5

Extension to Incomplete Fusion

The collisions of weakly bound nuclei have turned on great interest, both theoretical and experimental, over past decade[21,22]. In such collisions, the breakup cross section tends to be very large and breakup couplings may have a strong influence on the cross sections for several other channels. An important example is the fusion process, which becomes much more complex. In addition to the usual fusion reaction, in which the whole projectile merges with the target, there are other fusion processes taking place in collisions with weakly bound nuclei. There is the possibility that one or more, but not all, parts of projectile are absorbed by the target, whereas the other part(s) escapes the interaction region. It can also happen that all the parts of projectile are sequentially absorbed by the target, producing the same compound nucleus as in the case of direct fusion. When the compound nucleus does not contain all of the projectile's fragments, the process is named *incomplete fusion* (ICF), whereas the fusion of all of the projectile's nucleons with the target is called *complete fusion*. The CF cross section is the sum of the cross section for the direct fusion of the projectile with the target (DCF) and of the sequential fusion of all of the projectile's fragments (SCF). In Fig. 5.1, these processes are schematically depicted for a ^{6}Li+A reaction (assuming the two-body dissociation $^{6}\mathrm{Li} \rightarrow \alpha + d$)

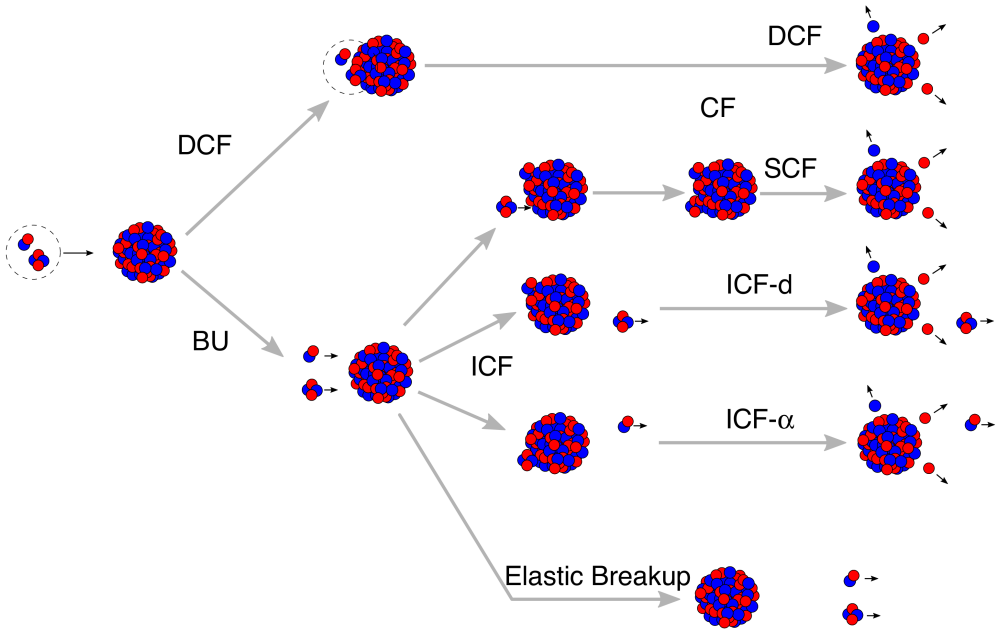

Figure 5.1: The basic idea of the fusion and breakup processes that can take place in ^{6}Li induced reaction. For simplicity ^{6}Li is considered as $\alpha - d$ two cluster model.

Many theoretical approaches have been proposed to study fusion reactions with weakly bound nuclei[21,22], including simple classical models[55,38], semi-classical models[14,96] and fully quantum-mechanical calculations[56,40,41,82] using the continuum discretized coupled channel method (CDCC). However in the CDCC calculations there is no procedure to distinguish CF and ICF.

This chapter will present possible extensions of IAV model to the calculation of ICF cross sections. This is a very timely topic in fusion studies, since there are experimental evidences indicating that in some cases ICF can be a significant part of the total fusion cross section. Moreover, ICF cross sections are needed for many applications, such as for surrogate reactions, as explained below. The calculation of ICF cross section is a very challenging problem to the extent that, nowadays, there are no fully quantum mechanical methods to reliably calculate these cross sections and most of the calculations rely on classical or semiclassical models. We note here that ICF is part of the NEB cross section. However, to extract the ICF cross section, one has to isolate it from other sources of NEB, such as transfer or target excitation. In this chapter we propose a simple model to make this separation and apply it to several cases.

5.1 A simple model for ICF within the IAV theory

In this section, we discuss a simple model to estimate the ICF cross section. To estimate the ICF part, the imaginary part of $x - A$ potential, W_x, has been divided into two parts,

$$W_x = W_x^{\mathrm{CN}} + W_x^{\mathrm{DR}} \tag{5.1}$$

one part W_x^{CN} corresponding to the formation of compound nucleus and the other part W_x^{DR} associated to all the remaining processes included in NEB, such as target excitation and the breakup of the x particle. The potential W_x^{CN} is parameterized in some convenient way (e.g., using a Woods-Saxon form) and its parameters are adjusted in order to reproduce the fusion cross section for the binary $x + A$ process. This procedure requires therefore the knowledge of the fusion cross section for the $x + A$ two-body reaction. In some cases, this quantity is known experimentally, but, if this not the case, one may resort to some theoretical estimate, for example, from a coupled-channel calculation. In the applications discussed below, we will use these two procedures. Once the parameters of W_x^{CN} have been determined, the ICF cross section is estimated as

$$\left.\frac{\mathrm{d}^2\sigma}{\mathrm{d}E_b\mathrm{d}\Omega_b}\right|^{\mathrm{ICF}} = -\frac{2}{\hbar v_a}\rho_b(E_b)\left\langle \psi_x^{\mathrm{IAV}}\middle| W_x^{\mathrm{CN}}\middle|\psi_x^{\mathrm{IAV}}\right\rangle. \tag{5.2}$$

Notice that, by construction, $\sigma^{\mathrm{ICF}} < \sigma^{\mathrm{NEB}}$, as it should be. Note also that the remaining part $\sigma^{\mathrm{NEB}} - \sigma^{\mathrm{ICF}}$ is associated with nonelastic direct processes of $x + A$, such as $x + A$ inelastic scattering.

5.2 Incomplete fusion contribution in $(^6Li, \alpha X)$ reactions

The collision of ^{6}Li on ^{209}Bi was considered as an example, whose inclusive α production was discussed in Sec. 3.2.1. First, the fusion potentials, W^{CN}, for α+^{209}Bi and d+^{209}Bi were extracted. For that, we made use of the experimental fusion cross sections for these systems, which are shown in Fig. 5.2(a) and (b), respectively. For the former case, we consider the (α, n) [6] and $(\alpha, 2n)$ [61] contributions. We found that the optical potential of α+^{209}Bi mentioned in Ref. [6] reproduce well these fusion data, as can be seen in Fig. 5.2 (a). This can be explained by noting that the α particle is tightly bound, and cannot be easily excited or broken up, thus making the fusion the dominant reaction channel. On the other hand, for the d+^{209}Bi case, we regarded $(d, 2n)$ and $(d, 3n)$ as sources of fusion channel. To determine, W^{CN}, we start from the parameters of the optical model potencial of Ref[57]. In order to reproduce the fusion data,

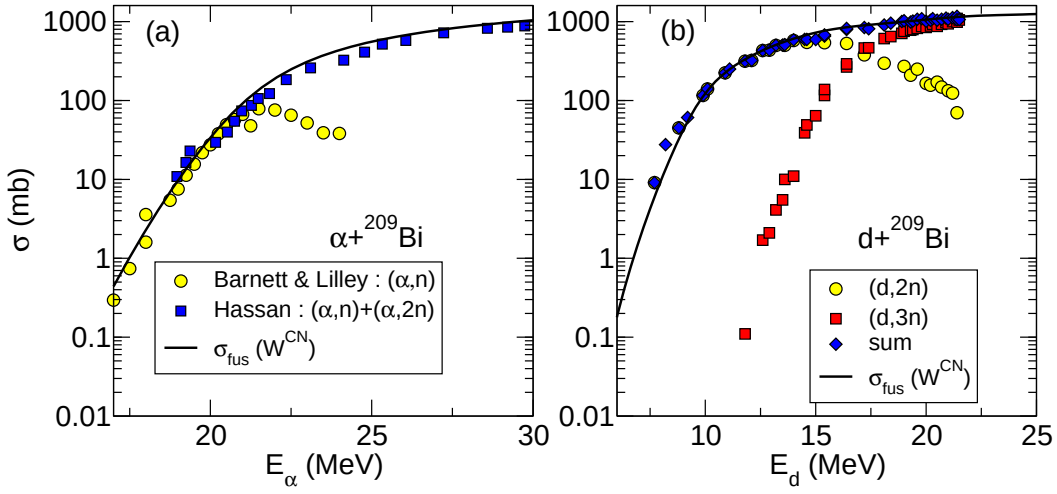

Figure 5.2: Calculated and experimental complete fusion cross section energy distribution of α+^{209}Bi (a) and d+^{209}Bi (b) in lab frame. The experimental data are taken from Refs.[6,61] for α+^{209}Bi, and Ref.[114] for d+^{209}Bi.

the radius of this potential needed to be reduced. This result is not unexpected, since direct channels, such as (d,p) or deuteron breakup, are expected to be important and must be therefore removed from the fusion potential. As shown in Fig 5.2 (b), with this fusion potential, the calculated fusion cross section reproduces fairly well the experimental data.

Now we compare the calculated ICF cross sections with the corresponding experimental data, reported in Ref.[32]. We note that the experimental data correspond to the cross sections for the production of nuclei with atomic numbers one or two units higher than that of Bi, namely, At and Po isotopes. Considering the dominant $d+\alpha$ structure of ^{6}Li, we may associate these processes with the absorption of the deuteron or the α clusters, respectively. Consequently, the total ICF cross section, will be calculated as the sum of the deuteron absorption (with the α surviving after the reaction) and the α absorption (with the deuteron surviving after the reaction). Using the notation introduced in previous chapters, these two contributions will be denoted as (^{6}Li, αX) and (^{6}Li, dX), respectively. Fig. 5.3 shows the calculated and experimental incomplete fusion cross section energy distribution as a function of the incident ^{6}Li energy. For comparison, we also show the experimental fusion data of ^{6}Li+^{208}Pb from Ref.[94]. It can be seen that the agreement between experiment and theory is poor. The calculated results largely overestimate the experimental data of Dasgupta *et. al.*[32] and underestimate the experimental data of Liu *et. al.*[94].

However, the experimental data of Dasgupta *et. al.* might have underestimated the actual incomplete fusion cross section, as some residues are populated both in complete and incomplete fusion and so

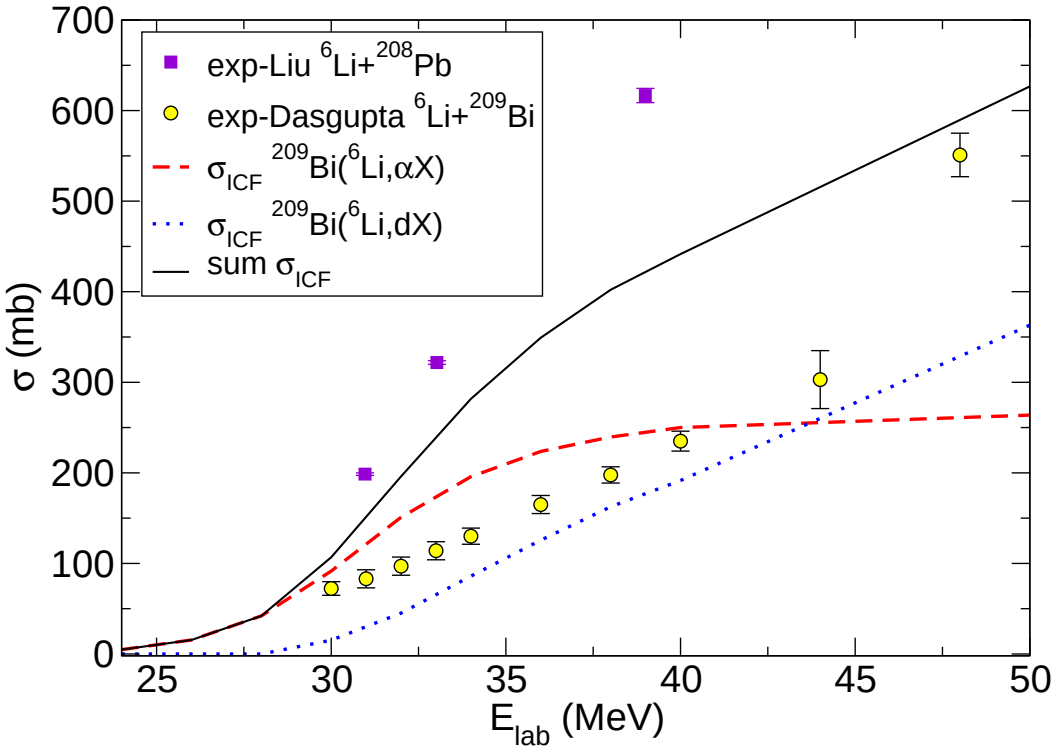

Figure 5.3: Calculated and experimental incomplete fusion cross section energy distribution of ^{6}Li+^{209}Bi in lab frame. The experimental data was taken from Refs. [32,94]

there is no way to disentangle experimentally the two components. Moreover, some residues produced in incomplete fusion events can proceed from the alpha decay of complete fusion evaporation residues. This contribution was in fact subtracted in the experimental analysis, but, as a result, larger error bars affect the data[32]. Under these circumstances, the incomplete fusion cross section of Dasgupta *et. al.* might be considered as a lower limit for the actual incomplete fusion cross section.

Concerning the comparison with the ^{6}Li+^{208}Pb case, it must be borne in mind that we assume that the ICF for this reaction has the same magnitude as that for ^{6}Li+^{209}Bi. Moreover, the experimental analysis of these data were extracted in a more indirect way. Each detected deuteron was assumed to have an alpha counterpart, and the α-ICF was obtained from the inclusive deuteron cross section, after subtracting the cross sections for the $\alpha + d$ and $\alpha + p$ coincidence channels, which were measured in this experiment. Similarly, the d-ICF cross section was also estimated. To do so, one has to make some strong assumptions, such as that the alpha and deuteron evaporation cross sections might be neglected (rather strong, especially for deuterons) and that α-, p- and n-transfer cross sections can be neglected as well.

Under these hypotheses, the evaluated ICF cross section for the system ^{6}Li+^{208}Pb might overestimate the actual ICF cross section.

We cannot rule out some uncertainties in our computed ICF cross sections. For that reason, further tests of the proposed model with ICF data are necessary to validate its reliability.

5.3 Application to surrogate reactions

Neutron induced reaction cross sections are important in several domains such as nuclear structure, nuclear astrophysics and nuclear technology. As reported in Ref.[46], these cross sections are key input information for modeling stellar element nucleosynthesis via $s-$ and $r-$processes. They also play an essential role in the design of advanced nuclear reactors for the transmutation of nuclear waste, or reactors based on innovative fuel cycles like Th/U cycle. However, direct measurements of these cross sections may encounter a variety of difficulties: The energy relevant for a particular application is often inaccessible. For the astrophysical purposes, such as descriptions of stellar environments and evolution, reaction rates at energies below 100 keV are needed. Furthermore, many important reactions involve unstable nuclei which are difficult to produce with currently available techniques or are too short lived to serve as targets in present setups, for which the *surrogate reaction method* can overcome this problem.

The *surrogate reaction method* aims at determining neutron induced cross sections for compound-nuclear reactions that involve targets which are difficult to produce. In this method, the same compound nucleus as in the neutron-induced reaction of interest is produced via an alternative or surrogate reaction. The surrogate reaction method is schematically represented in Fig. 5.4. The left part of this figure illustrates the desired reaction, $n+A$, which leads to the formation of the compound nucleus B^*. The nucleus B^* can decay via different exit channels: neutron evaporation, fission, and γ emission. On the right hand side of Fig. 5.4, the same compound nucleus B^* is produced through a surrogate reaction. As shown in Fig. 5.4, the surrogate reaction is an inclusive breakup reaction between the projectile, d, and the target A, leading to a heavy residual nucleus B^* and an ejectile p.

In most applications of the surrogate method, the surrogate reaction is used to measure the decay probability P_χ corresponding to a given decay model χ and the desired neutron induced reaction cross section is

$$\sigma_{B_\chi}^{CN}(E_n) = \sigma_B^{CN}(E_n) P_\chi(E_n) \tag{5.3}$$

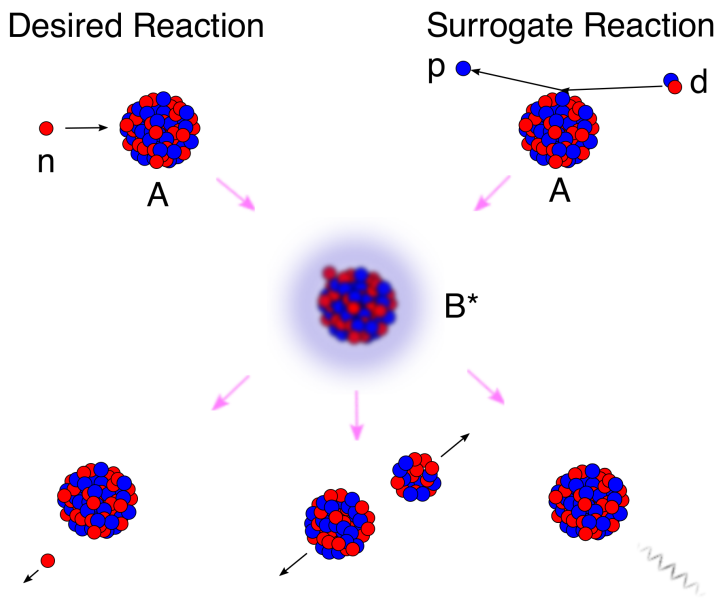

Figure 5.4: Schematic representation of the desired and surrogate reaction mechanisms. The basic idea of the surrogate approach is to replace the first step of the desired reaction, $n + A$, by an surrogate reaction, $d + A \rightarrow p + B^*$, that is experimentally easier to populate the same compound nucleus. The subsequent decay of the compound nucleus into the relevant channel which can be measured and used to extract the desired cross section. Three typical decay channels are showed here: neutron evaporation, fission, and γ emission.

where $\sigma_B^{CN}(E_n)$ is the cross section for the formation of a compound nucleus B via the absorption of a neutron by the target A and E_n is the relative energy of $x - A$ system. The compound nucleus formation cross section σ_B^{CN} can be estimated by phenomenological optical model calculations with an accuracy of about 10% for nuclei no too far from the stability valley[46]. Then, in the surrogate method the decay probability is estimated as[43]:

$$P_\chi(E_n) = \frac{N_\chi^C(E_n)}{N^S(E_n)\varepsilon_\chi(E_n)}, \tag{5.4}$$

where $N^S(E_n)$ is the total number of detected protons as a function of E_n, i.e., the inclusive total breakup (TBU). $N_\chi^C(E_n)$ is the "coincidence spectrum", corresponding to the number of protons detected in coincidence with the observable that identifies the decay mode, i.e., incomplete fusion with neutron absorbed by the target, and $\varepsilon_\chi(E_n)$ is the associated detection efficiency. The (n, x) cross sections determined using these decay probabilities tend to underestimate the direct neutron induced data. One possible explanation is, that in the surrogate reaction, there are sources of protons which do not lead to the formation of the compound nucleus (CN) B^*. These protons are however detected and included in the quantity $N^S(E_n)$ of

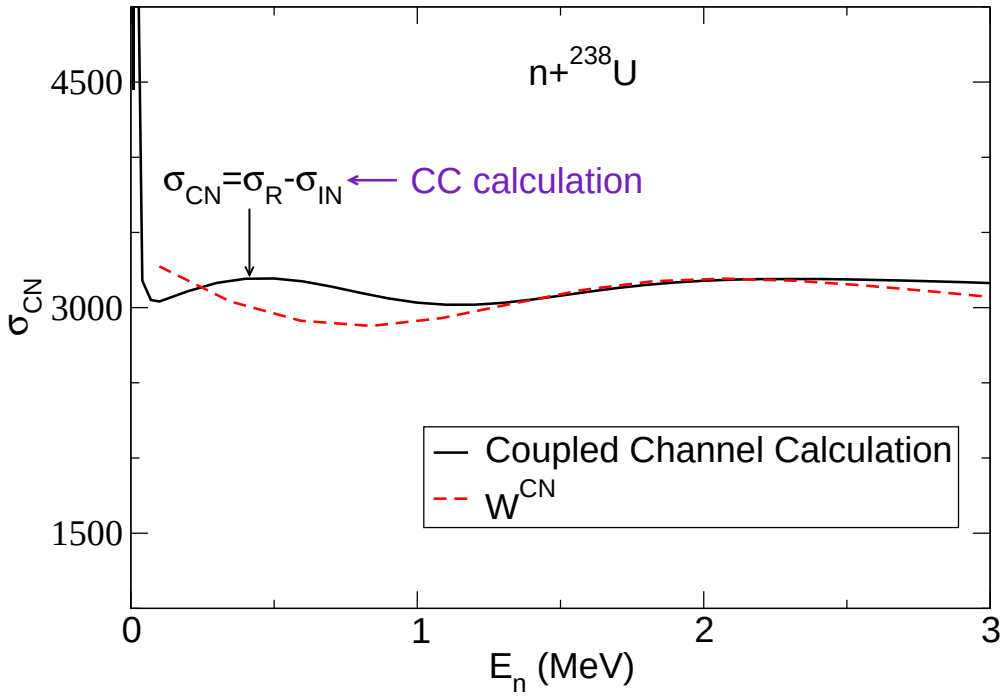

Figure 5.5: Calculated fusion cross section for the $n+^{238}$U system. The solid line is result obtained from the code EMPIRE [62] using the CC method, whereas the dashed line is the absorption obtained with the fusion potential W_x^{CN}. See text for details.

Eq. (5.6). Consequently, $N^S(E_n)$ must be corrected by multiplying it by the fraction of protons which are actually associated with the formation of B^* or, in other words, by the fraction of protons leading to ICF. This amounts at multiplying $N^S(E_n)$ by the factor:

$$\frac{\sigma_{\mathrm{ICF}}(E_n)}{\sigma_{\mathrm{TBU}}(E_n)}, \tag{5.5}$$

or, equivalently, correcting $P_\chi(E_n)$ as

$$P_\chi^{\mathrm{corr}}(E_n) = \frac{P_\chi^{\mathrm{meas}}(E_n)\sigma_{\mathrm{TBU}}(E_n)}{\sigma_{\mathrm{ICF}}(E_n)}, \tag{5.6}$$

where $P_\chi^{\mathrm{meas}}(E_n)$ is the measured decay probability.

As an example, the surrogate reaction ^{238}U (d,pf) is considered. This reaction was recently measured by B. Jurado and her collaborators from Bordeaux as a surrogate for the ^{238}U(n,f) reaction, where "f" denotes a fission channel. The experimental results presented here and the corresponding theoretical

analysis have been recently submitted for publication[43] and are also included in the Ph.D. thesis of Q. Ducasse[42].

First the fusion potential of $n-^{238}$U, $W^{\rm CN}$, was studied. In this case, since we did not find experimental data for the total fusion cross section for this system, we relied on the fusion cross section predicted by a coupled-channel calculation, supplied by Dr. Roberto Capote[26] and performed with the code EMPIRE[62]. This calculation assumed that the dominant non-elastic channels for $n+^{238}$U correspond to the inelastic scattering populating the first low-lying states of ^{238}U. These states were treated within the rotational model, with deformation parameters of $\beta_2 = 0.222$ and $\beta_4 = 0.102$. The CN cross section is then obtained subtracting the summed cross section for the population of these states to the reaction cross section, also obtained from this calculation. The resulting CN cross section is shown in Fig. 5.5 (the black solid line). To determine W_x, we consider single-channel optical model calculation for $n+^{238}$U, using the optical model potential from Ref.[58]. The absorption cross section due to an imaginary potential $W^{\rm CN}$ is then calculated as:

$$\sigma_{\rm CN} = -\frac{2}{\hbar v_a}\langle \chi_a^{(+)} | W_x^{\rm CN} | \chi_a^{(+)} \rangle, \tag{5.7}$$

where $\chi_a^{(+)}$ is calculated with the neutron optical potential of Han[58], and $W_x^{\rm CN}$, has the same form as the imaginary part of Han, but with a smaller interaction radius, $r_w^{\rm CN} < r_w$. By modifying the value of $r_w^{\rm CN}$, the fusion shown in Fig. 5.5 (dashed line) is obtained, which shows a reasonable agreement with the CC fusion cross section (solid line).

Now the calculations for the surrogate reaction ^{238}U (d,pf) at 15 MeV and 18 MeV are presented and compared with the data from Refs.[43,15]. The EBU component was calculated with the CDCC framework. For the $p-n$ interaction, the simple Gaussian form of Ref.[4] was considered. The $n-p$ states were included for $\ell = 0-7$ partial waves to achieve convergence of the calculated cross sections. The proton-target and neutron-target interactions were adopted from the global parametrization of Ref.[58], omitting the spin-orbit term, and evaluated at half of the deuteron incident energy. The NEB component was calculated with the IAV formalism. The $d-$target potential was taken from Ref.[2].

Figure 5.6 shows the calculated contributions to the inclusive total deuteron breakup process (TBU) for a deuteron beam energy of 15 MeV and the outgoing proton angle of 140 degrees (a) and for a deuteron beam energy of 18 MeV and the outgoing proton angle of 150 degrees (b), as a function of the excitation energy of the residual nucleus ^{239}U, $E^* = E_n + S_n$, where $S_n = 4.806$ MeV is the neutron separation energy of ^{239}U. The dotted, dashed and dash-dotted lines are, respectively, the elastic breakup (EBU),

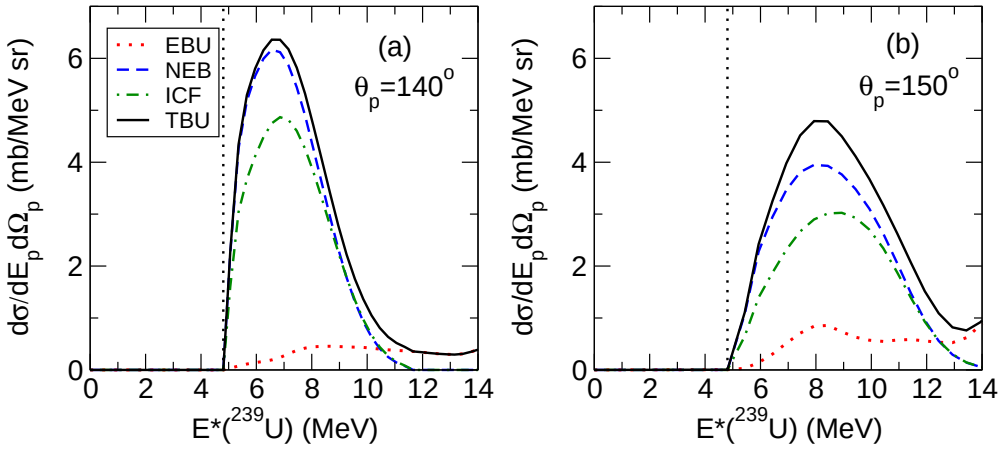

Figure 5.6: Calculated contributions to the inclusive total deuteron breakup process (TBU) as a function of the excitation energy of ^{239}U for deuteron beam energy of 15 MeV with outgoing proton angle of 140 degrees (a) and for deuteron beam energy of 18 MeV with outgoing proton angle of 150 degrees (b). The dotted, dashed and dash-dotted lines are, respectively, the elastic breakup (EBU), nonelastic breakup (NEB) and incomplete fusion (ICF) contributions. The solid line is the sum of EBU and NEB. The vertical dotted lines indicate the neutron separation energy of ^{239}U.

nonelastic breakup (NEB) and incomplete fusion (ICF) contributions. The solid line is the sum of EBU and NEB. The vertical dotted lines indicate the neutron separation energy of ^{239}U. It can be seen that the relative contribution of the different processes to the total cross section for both incident energies and outgoing angles is rather similar. For the energy range $E^* < (S_n + 1.5)$ MeV, the elastic breakup is less than 5% of the total breakup, whereas the ICF represents nearly 80%. The computed ICF cross sections are used to correct the measured decay probabilities for the (d, pf) channel, where f is a fission product. The corrected probabilities are compared with the direct measurements for the (n, f) reaction obtained from the Japanese Evaluated Nuclear Data Library (JENDL) 4.0 database [120].

The corrected decay probability of ^{238}U(d, pf) at the incident energy of 15 MeV with $\theta_p = 126°$ and 18 MeV with $\theta_p = 140°$ are presented in Fig. 5.7. In this figure, the solid line is the data from the JENDL. The solid circles and solid triangles are the uncorrected values extracted from the (d, pf) surrogate reactions at 15 MeV and 18 MeV, respectively. The open circles and open triangles are the corrected probabilities, obtained from Eq. (5.6). It can be seen that the corrected probability of ^{238}U (d, pf) at the incident energy of 15 MeV [43] is in better agreement with the neutron-induced data. However, this corrected decay probability is still lower by about 15% than the neutron-induced data evaluated by JENDL 4.0 [120]. As discussed in more detail in Ref. [42], this difference may be attributed to the contribution from protons coming from fusion-evaporation on oxygen in the target. When the decay probability of

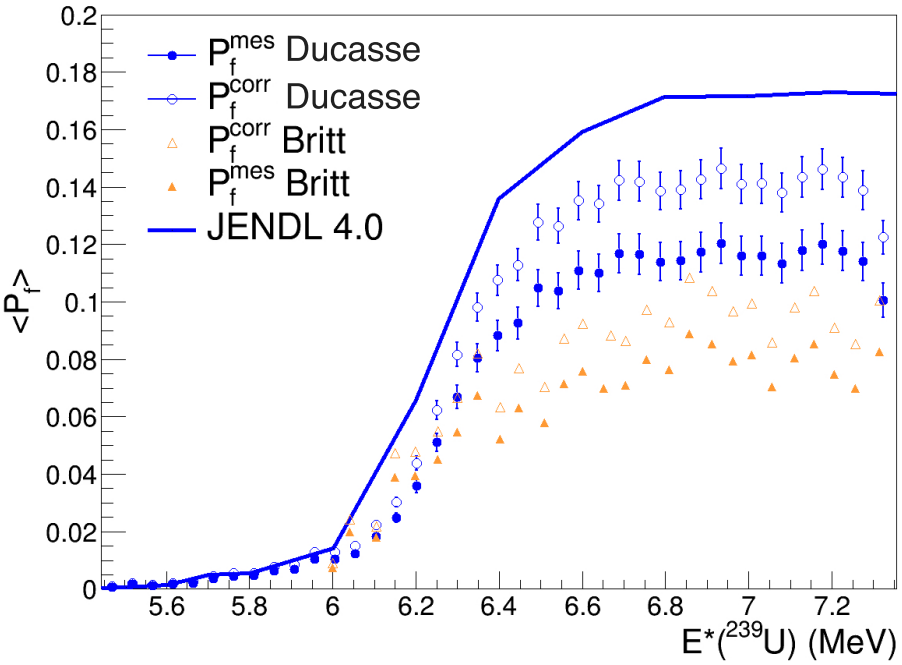

Figure 5.7: Measured P_f^{meas} and corrected P_f^{corr} decay probabilities as a function of excitation energy. The solid line are the values for the direct neutron-induced measurement, taken from the JENDL database [120]. The circles and up triangles are respectively the decay probabilities of ^{238}U (d,pf) at incident energy of 15 MeV with $\theta_p = 126^o$ and 18 MeV with $\theta_p = 140^o$.

^{238}U (d, pf) at the incident energy of 18 MeV [15] is corrected, the resulting probability is still significantly lower than the neutron-induced data. The difference might also come from fusion-evaporation on oxygen, which can be very significant due to the complete oxidation of the target used in Ref. [15].

Despite these differences with the data, we believe that the calculations presented in this section have served to illustrate the potential usefulness of the method as a tool to correct surrogate reaction cross sections.

To explain all nature is too difficult a task for any one man
or even for any one age.

Isaac Newton

6

Conclusions and perspectives

In this dissertation, we have addressed the problem of the calculation of inclusive breakup cross sections in reactions induced by weakly-bound projectiles, within the framework of the theory proposed by Ichimura, Austern and Vincent in the 1980s [71,4]. We have presented the post and prior formulas of this model, and discussed their formal and numerical equivalence. We have also provided an alternative derivation of the IAV formula, which combines the original derivation of Austern and Vincent [5] and the coupled-channels optical theorem [30]. This provides in a very straightforward way the formulas for the elastic and non-elastic breakup parts of the total inclusive cross section. We have applied the model to several reactions induced by weakly bound projectiles, comparing with experimental data when available.

We have applied the IAV formulas to deuteron induced reactions on light and medium-mass targets. For the EBU part, we have compared the results employing the distorted-wave Born approximation (DWBA) method and the Continuum Discretized Coupled Channels (CDCC) method. The latter is expected to be more accurate since it treats the breakup to all orders. Nevertheless, in the cases studied in this work, the DWBA method has been found to be a good approximation to the CDCC method. For the NEB part, we have investigated the convergence problem of the post form DWBA, comparing the

damping factor and binning methods. We have also tested the validity of zero-range (ZR) approximation and the effect of the remnant term in the NEB calculation by comparing zero-range with finite-range DWBA calculations. For the deuteron induced reaction the effect of the remnant term has been found to be very small and the ZR calculation gives a result very close to the full FR calculation. Interestingly, the proton inclusive cross section is largely dominated by the NEB mechanism. The EBU mechanism becomes competitive only at very small angles.

We have applied the IAV formulas to ^{6}Li induced reactions on different targets and energies around the Coulomb barrier. We have found that the sum EBU (calculated with CDCC) + NEB (DWBA) provides a good agreement with the experimental angular distributions of α particles. As in the (d,pX) case, the inclusive cross section is largely dominated by the NEB mechanism, and the EBU becomes only dominant at very small angles, where the breakup is nevertheless small. The systematic behaviour of the α-particle production has been also studied. We have found that the calculated total breakup cross sections (TBU = EBU + NEB) show some universal trend for the heavy targets, but significant deviations have been found for the light targets.

We have extended our study to the case of halo nuclei, taking the ^{11}Be system as an example. We have performed calculations for the ^{11}Be+^{64}Zn reaction, comparing our calculations with the experimental data from Ref.[36] In this case, we found that the EBU part is the dominant contribution of the ^{10}Be inclusive cross section, whereas the NEB part becomes only relevant and comparable to the EBU part at large angles. For the EBU part, we have used the recent results obtained with an extended version of the CDCC method (XCDCC), which includes the effect of core excitations in the structure of ^{11}Be as well as in the reaction dynamics. The summed EBU (calculated with XCDCC) + NEB (DWBA) agrees well with the experimental data and evidences the importance of the NEB mechanism.

In order to test the validity of IAV model for non $s-$wave projectiles, we have investigated reactions induced by ^{7}Li and ^{7}Be, for which the g.s. consists of a $p-$ wave. These nuclei are treated within the two-cluster model ^{4}He+$t/^{3}$He. For the ^{7}Li + ^{208}Pb reaction, there are two sets of the experimental data available for the angular distribution of inclusive alpha particles[98,83], which agree well at forward angles, but differ significantly at backward angles. Our calculations reproduce well the forward-angle data of Mazzocco *et. al.*[98] at $E_{\rm lab} = 33$ and 39 MeV, but they overestimate the data at larger angles. At $E_{\rm lab} = 29$ MeV, the overestimation is observed in the full angular range. The explanation of this disagreement not clear to us.

We have analysed the α and ^{3}He yields resulting from the ^{7}Be + ^{58}Ni reaction at the near-barrier energy of 21.5 MeV. The experimental data of Ref.[99] show that the alpha yield is about $4 \sim 5$ times larger than the ^{3}He one, suggesting that the elastic breakup mechanism is small in this reaction. In this case, our calculations reproduces fairly well the (^{7}Be,αX) data, but overestimate the (^{7}Be,^{3}HeX) cross section by $\sim 60\%$ at large angles. However, we should emphasize that the cross section of (^{7}Be,αX) is much larger than the cross section of (^{7}Be,^{3}HeX). Our calculations corroborate the dominance of the NEB. Additional calculations for the ^{4}He+^{58}Ni and ^{3}He+^{58}Ni reactions suggest that this result is a consequence of the larger reaction cross section for the latter case.

We also considered the case of the ^{7}Be production in the scattering of the proton halo nucleus ^{8}B on a ^{58}Ni target. This is another example of non $s-$wave projectile, since the proton halo has a dominant $p_{3/2}$ configuration. In this case, we found that the inclusive ^{7}Be production is dominated by the EBU part and the influence of NEB is very small.

We have studied the dependence of the EBU and NEB contributions with the incident energy and the separation energy of the projectile taking the ^{6}Li+^{209}Bi reaction as an example, and varying artificially the separation energy of ^{6}Li. In most situations, we find a clear dominance of NEB. The EBU becomes only dominant for very small separation energies ($S_{\alpha d} \approx 0.5$ MeV), at near- and sub-Coulomb energies.

We have verified that the sum of the calculated EBU+NEB cross section and the experimental CF cross section is very close to the reaction cross section for the ^{6}Li+^{209}Bi reaction, at the energies around Coulomb barrier. Since the reaction cross section imposes an strict upper limit for non-elastic processes, this result constitutes a robust consistency test of the theories considered here.

We have investigated the problem of the post-prior equivalence for inclusive breakup cross sections. We have reexamined the post and prior formulas of this model, and discussed their formal and numerical equivalence. We have seen that the prior-form formula consists of three terms. One of these terms coincides with NEB formula proposed by Udagawa and Tamura (UT). The remaining terms, which arise from the non-orthogonality of the initial and final partitions, ensure the post-prior equivalence of the NEB cross sections. We have applied these formulas to the ^{6}Li+^{209}Bi and d+^{62}Ni reactions, finding that the post and prior expresssions give identical NEB results, thus confirming the post-prior equivalence at a numerical level. We have also verified that the prior formula proposed by Udagawa and Tamura, which omits the non-orthogonality terms appearing in the IAV formula, tends to underestimate the experimenta data for the analyzed reactions.

We also discussed the possibility of applying the IAV theory to the calculation of incomplete fusion (ICF). As noted in the Introduction, ICF is part of the NEB cross section and, as such, is included in the IAV formula. However, it is not straightforward how to isolate the ICF contribution from other sources of NEB associated with direct reactions (DR) of x with the target, such as $x + A$ inelastic scattering. Assuming that one can split the imaginary part of U_x as the sum of CN and DR contributions, i.e., $W_x = W_x^{\rm DR} + W_x^{\rm CN}$, we have proposed that that the ICF cross section can be approximately calculated with a formula analogous to that of IAV, but using the $W_x^{\rm CN}$ instead of W_x in the expectation value [see Eq. (5.2)]. As an application of this formula we have considered the reactions ^{6}Li+^{209}Bi and ^{6}Li+^{208}Pb. Although the ICF is expected to be similar for both systems, the data is considerably larger for the second case. Our calculated ICF cross sections lie between the two experimental data sets. We have also applied our ICF model to the surrogate reaction ^{238}U(d,pf), comparing also with recent data.

The results presented in this work, along with those presented in related works[27,92,91,112], indicate that the IAV model provides a reliable framework to calculate NEB cross sections in reactions induced by weakly bound projectiles.

Several possible extensions and improvements are planned for the future. We enumerate some of them:

(i) As mentioned in the dissertation, all the inclusive breakup calculations performed so far rely on the DWBA approximation, i.e., they represent the exact scattering wave function by the product of a elastic scattering distorted wave ($\chi_a^{(+)}$) times the projectile and target ground-state wave functions, i.e.,

$$\Psi^{(+)}(\xi,\vec{r}_x,\vec{r}_b) \approx \varphi_A^0(\xi)\varphi_a(\vec{r}_{bx})\chi_a^{(+)}(\vec{k}_a,\vec{r}_a). \tag{6.1}$$

The distorted wave $\chi_a^{(+)}$ is meant to include, in an effective way, all possible couplings affecting the elastic scattering of $a + A$. This includes, for instance, the excitation of the projectile and/or target. As occurs in other coupled-channels (CC) problems, it may happen that these intermediate states, which may also lead to NEB, need to be incorporated explicitly.

(ii) For simplicity, our implementation of the IAV model ignores the internal spins of the participant and spectator fragments. In particular, this means that the spin-orbit part of the $x-$target interaction is omitted, and this may lead to an unrealistic descripion of the $x-$target spectrum (for example, the position of bound states and resonances). Consequently, the inclusion of the spin is planned for a

future implementation of the model.

(iii) Our numerical implementation of IAV model relies on the DWBA approximation. For very weakly-bound projectiles, the effect of breakup in the incident channel is important. In this case, $\Psi^{(+)}$ can be approximated by a CDCC wave function. This corresponds in fact to the three-body model proposed by Austern *et al.*[4]. Although the CDCC method is widely used nowadays, its implementation in the IAV formalism is not straightforward. Nevertheless, with the present computational capabilities, this should be feasible at least for specific cases.

(iv) In some cases, the simple two-cluster model with inert clusters may be too simplistic. For example, in the ^{11}Be+^{64}Zn reaction, we pointed out that the effect of the ^{10}Be deformation is very important in the structure of the ^{11}Be projectile, leading to noticeable effects in the EBU cross sections. It would be interesting to study the effect of deformation on the NEB cross sections.

(v) If collective excitations to some states of the projectile or target are strong, one may include them explicitly using a CC approximation for $\Psi^{(+)}$. Notice that, in this case, this wave function becomes formally analogous to that appearing in the standard CCBA method.

(vi) The CDCC wave function contains in general many terms so the evaluation of the source term of the inhomogeneous equation (2.12) will be cumbersome. For incident energies of several tens of MeV per nucleon, one may invoke as an alternative the adiabatic approximation of Johnson and Soper[77]. This approximation will be valid when the average excitation energies of the projectile are small with respect the beam energy. Under this situation, the adiabatic wave function is known to reproduce well the full three-body wave function for small *b*-*x* separations, which dominates the source term.

(vii) A more complete three-body description of the incident channel is given by the Faddeev wave function. This is the choice made in the formal works of Hussein and co-workers[66]. In practice, the solution of the Faddeev equations is too complicated for many practical applications and, even if this solution is available, its implementation in Eq. (2.12) will be very challenging.

A

Cross section in Lab Frame

The double differential cross calculated with the IAV model is in c.m. frame, so in order to compare with the experimental observables, the calculated results need to be transformed from c.m. frame to lab frame. For the nonelastic breakup process of the form

$$a(b+x)+A \rightarrow b+B(A+x), \tag{A.1}$$

the initial center of mass energy is

$$E^{i}_{cm} = E_{lab}\frac{m_A}{m_A+m_a}. \tag{A.2}$$

If $\vec{v}^{cm}_{\mathfrak{b}}$ is the velocity of b in the c.m. system pointing in the direction (θ_C, φ_C) and $\vec{v}^{lab}_{\mathfrak{b}}$ its velocity in the laboratory system corresponding to a direction (θ_L, φ_L), one has

$$\vec{v}^{lab}_{\mathfrak{b}} = \vec{v}^{cm}_{\mathfrak{b}} + \vec{V}_{lab}, \tag{A.3}$$

where $\vec{V}_{lab}$ is the velocity of the center of mass in the laboratory system. Thus

$$v_{\mathfrak{b}}^{lab}\cos\theta_{\mathfrak{b}}^{L} = v_{\mathfrak{b}}^{cm}\cos\theta_{\mathfrak{b}}^{C} + V_{lab}, \tag{A.4}$$

$$v_{\mathfrak{b}}^{lab}\sin\theta_{\mathfrak{b}}^{L} = v_{\mathfrak{b}}^{cm}\sin\theta_{\mathfrak{b}}^{C}. \tag{A.5}$$

Combining the two equations above we get the following expression for the transformation of the center of mass to the laboratory frame angles:

$$\cos\theta_{\mathfrak{b}}^{L} = \frac{\cos\theta_{\mathfrak{b}}^{C} + \tau}{(1 + 2\tau\cos\theta_{\mathfrak{b}}^{C} + \tau^2)^{1/2}}, \tag{A.6}$$

where

$$\tau = \frac{V_{lab}}{v_{\mathfrak{b}}^{cm}} = \Big[\frac{m_a m_b}{m_A m_B}\frac{E_{cm}^{i}}{E_{cm}^{f}}\Big]^{1/2}, \tag{A.7}$$

where E_{cm}^{f} is the c.m. energy in the final channel $b + B$. The relation between center of mass energy and lab energy of particle b is

$$E_{\mathfrak{b}}^{lab} = \beta^2 E_{\mathfrak{b}}^{cm}, \tag{A.8}$$

with

$$\beta = \frac{v_{\mathfrak{b}}^{lab}}{v_{\mathfrak{b}}^{cm}} = [1 + 2\tau\cos\theta_{\mathfrak{b}}^{C} + \tau^2]^{1/2}. \tag{A.9}$$

$E_{\mathfrak{b}}^{c}m$ is the energy of the particle C in the c.m. frame, which is related to the total c.m. energy as by:

$$E_{\mathfrak{b}}^{cm} = \frac{m_B}{m_b + m_B}E_{cm}^{f}. \tag{A.10}$$

Analogously, using again Eqs. (A.4) and (A.5) we may derive the following relations for the transformation of the scattering angle and the energy of the b particle from the laboratory frame to the c.m. frame:

$$\tan\theta_{\mathfrak{b}}^{C} = \frac{\sin\theta_{\mathfrak{b}}^{L}}{\cos\theta_{\mathfrak{b}}^{L} - \gamma}, \tag{A.11}$$

with

$$\gamma = \frac{V_{lab}}{v_{\mathfrak{b}}^{lab}} = \tau/\beta, \tag{A.12}$$

$$E_{\mathfrak{b}}^{cm} = \frac{1}{\beta^2}E_{\mathfrak{b}}^{lab}. \tag{A.13}$$

A.0.1 Relations Between Cross Sections

The relation between the differential cross sections in the two frames can be obtained from

$$\frac{\mathrm{d}\sigma^{cm}}{\mathrm{d}E_{\mathfrak{b}}^{cm}\mathrm{d}\Omega_{\mathfrak{b}}^{cm}}\mathrm{d}E_{\mathfrak{b}}^{cm}\mathrm{d}\Omega_{\mathfrak{b}}^{cm} = \frac{\mathrm{d}\sigma^{lab}}{\mathrm{d}E_{\mathfrak{b}}^{lab}\mathrm{d}\Omega_{\mathfrak{b}}^{lab}}\mathrm{d}E_{\mathfrak{b}}^{lab}\mathrm{d}\Omega_{\mathfrak{b}}^{lab}, \tag{A.14}$$

$$\frac{\mathrm{d}\sigma^{lab}}{\mathrm{d}E_{\mathfrak{b}}^{lab}\mathrm{d}\Omega_{\mathfrak{b}}^{lab}} = \frac{\mathrm{d}\sigma^{cm}}{\mathrm{d}E_{\mathfrak{b}}^{cm}\mathrm{d}\Omega_{\mathfrak{b}}^{cm}}\frac{\sin\theta_{\mathfrak{b}}^{cm}}{\sin\theta_{\mathfrak{b}}^{lab}}. \tag{A.15}$$

The differential cross section provided by the DWBA calculations is a funciton of the total kinetic energy $E_c m^f$. Using the relation Eq. (A.10) we may rewrite it in terms of the energy of the b particle as :

$$\frac{\mathrm{d}\sigma^{cm}}{\mathrm{d}E_{\mathfrak{b}}^{cm}\mathrm{d}\Omega_{\mathfrak{b}}^{cm}} = \frac{\mathrm{d}\sigma^{cm}}{\mathrm{d}E_{cm}^{b}\mathrm{d}\Omega_{\mathfrak{b}}^{cm}}\frac{\mathrm{d}E_{cm}^{f}}{\mathrm{d}E_{\mathfrak{b}}^{cm}} = \frac{\mathrm{d}\sigma^{cm}}{\mathrm{d}E_{cm}^{f}\mathrm{d}\Omega_{\mathfrak{b}}^{cm}}\frac{m_b + m_B}{m_B}. \tag{A.16}$$

B

The partial wave expansion of EBU formula in DWBA

We recall the differential cross section of elastic breakup of Eq. (2.21)

$$\left.\frac{d^2\sigma}{d\Omega_b dE_b d\Omega_x}\right|_{\text{EBU}} = \frac{2\pi}{\hbar v_a}\rho_b(E_b)\rho_x(E_x)|T_{fi}|^2. \tag{B.1}$$

where $\rho_b(E_b)$ and $\rho_x(E_x)$ are the phase-space factors given by $\rho(E) = \mu k/8\pi^3\hbar^2$. It should be noted that the transition amplitude T_{fi} contains the three-body wave function Ψ^{3b}, which is a complicated object by itself. For that reason, we apply the DWBA approximation to the incident channel, then transition amplitude can be written as

$$T_{fi} = \langle \chi_x^{(-)}(\vec{r}_x,\vec{k}_x)\,\chi_b^{(-)}(\vec{r}_b,\vec{k}_b)|V_{\text{post}}|\chi_a^{(+)}(\vec{r}_a,\vec{k_a})\varphi_a(r_{bx})\Big\rangle. \tag{B.2}$$

By using the relation of Eq. (2.29) and Eq. (2.27), the transition amplitude can be partial wave expanded as

$$T_{fi} = \sum_{l_x m_x} \int \frac{4\pi}{k_x} i^{l_x} R_{l_x}(r_x) \rho_{l_x m_x; m_{bx}}(r_x, \vec{k}_a, \vec{k}_b) Y_{l_x}^{m_x *}(\hat{k}_x) \mathrm{d}r_x, \tag{B.3}$$

where $\rho_{l_x m_x; m_{bx}}(r_x, \vec{k}_a, \vec{k}_b)$ is again the source term already introduced in Chapter 2 [see Eq. (2.27)]. As we did for the NEB contribution, this source term can be evaluated exactly, or using some of the approximations discussed in Chapter 2. The finite-range and zero-range expansions are given in Eqs. (2.38) and (2.52). By inserting this transition amplitude into the triple differential cross section and integrating on $d\Omega_x$, we get the double differential cross section with respect the energy and the scattering angle of b,

$$\left.\frac{d^2\sigma}{d\Omega_b dE_b}\right|_{\mathrm{EBU}} = \frac{2\pi}{\hbar v_a} \rho_b(E_b) \rho_x(E_x) \sum_{l_x m_x} \left| \int \frac{4\pi}{k_x} i^{l_x} R_{l_x}(r_x) \rho_{l_x m_x; m_{bx}}(r_x, \vec{k}_a, \vec{k}_b) \mathrm{d}r_x \right|^2 . \tag{B.4}$$

C

Finite Range Correction

As in transfer reactions leading to bound states, one may include part of the finite-range effects introducing the so-called finite-range correction[119]. In the present formulation, a similar procedure can be used. This is done as follows. The source term can be written as

$$\begin{aligned}\rho_b(\vec{r}_x) &= \int \mathrm{d}\vec{r}_{bx}\chi_b^{(-)*}(\vec{r}_b)V_{bx}(\vec{r}_{bx})\varphi_a(\vec{r}_{bx})\chi_a^{(+)}(\vec{r}_a) \\ &= \int \mathrm{d}\vec{r}_{bx}\chi_b^{(-)*}(q\vec{r}_x-\vec{r}_{bx})V_{bx}(\vec{r}_{bx})\varphi_a(\vec{r}_{bx})\chi_a^{(+)}(\vec{r}_x-p\vec{r}_{bx}).\end{aligned} \tag{C.1}$$

Then, by use of the translation operator, the distorted waves can be written as

$$\chi_b^{(-)*}(q\vec{r}_x-\vec{r}_{bx}) = e^{-\frac{1}{q}\vec{r}_{bx}\nabla_b}\chi_b^{(-)*}(q\vec{r}_x), \tag{C.2}$$

$$\chi_a^{(+)}(\vec{r}_x-p\vec{r}_{bx}) = e^{-p\vec{r}_{bx}\nabla_a}\chi_a^{(+)}(\vec{r}_x), \tag{C.3}$$

then

$$\rho_b(\vec{r}_x) = \int \mathrm{d}\vec{r}_{bx}e^{\vec{r}_{bx}\cdot\mathcal{O}}\chi_b^{(-)*}(q\vec{r}_x)V_{bx}(\vec{r}_{bx})\varphi_a(\vec{r}_{bx})\chi_a^{(+)}(\vec{r}_x), \tag{C.4}$$

with

$$\mathcal{O} = -\frac{1}{q}\nabla_b - p\nabla_a. \tag{C.5}$$

The operator $\exp(\vec{r}_{bx}\cdot\mathcal{O})$ can be expressed as an expansion in powers and multipoles (solid harmonics) of its arguments:

$$e^{(\vec{r}_{bx}\cdot\mathcal{O})} = 4\pi\sum_{n\lambda\mu} C_{n\lambda} r_{bx}^{2n+\lambda} Y_\lambda^{\mu *}(\hat{r_{bx}})\mathcal{O}^{2n+\lambda} Y_\lambda^\mu(\hat{\mathcal{O}}), \tag{C.6}$$

where

$$C_{n\lambda} = \frac{(n+\lambda)!2^\lambda}{n!(2n+2\lambda+1)!}. \tag{C.7}$$

Let us introduce the integral

$$\begin{aligned} I_{bx}(\mathcal{O}) &= \int \mathrm{d}\vec{r}_{bx} e^{\vec{r}_{bx}\cdot\mathcal{O}} V_{bx}(\vec{r}_{bx})\varphi_a(\vec{r}_{bx}) \\ &= \int \mathrm{d}\vec{r}_{bx} 4\pi \sum_{n\lambda\mu} C_{n\lambda} r_{bx}^{2n+\lambda} Y_\lambda^{\mu *}(\hat{r_{bx}})\mathcal{O}^{2n+\lambda} Y_\lambda^\mu(\hat{\mathcal{O}}) V_{bx}(\vec{r}_{bx})\varphi_a(\vec{r}_{bx}), \end{aligned} \tag{C.8}$$

with

$$\varphi_a(\vec{r}_{bx}) = \sum_{m_{bx}} \frac{R_{l_{bx}}(r_{bx})}{r_{bx}} Y_{l_{bx}}^{m_{bx}}(\hat{r_{bx}}), \tag{C.9}$$

The integral over $\hat{r}_{bx}$ selects out the $\lambda = l_{bx}, \mu = m_{bx}$ term from the Taylor expansion, so

$$I_{bx}(\mathcal{O}) = \sum_{m_{bx}} I_{l_{bx}m_{bx}}(\mathcal{O}), \tag{C.10}$$

where

$$I_{l_{bx}m_{bx}}(\mathcal{O}) = 4\pi\sum_n C_{nl_{bx}} d_{nl_{bx}} \mathcal{O}^{2n+l_{bx}} Y_{l_{bx}}^{m_{bx}}(\hat{\mathcal{O}}), \tag{C.11}$$

$$d_{nl_{bx}} = \int \mathrm{d}r_{bx} V_{bx}(r_{bx}) R_{l_{bx}}(r_{bx}) r_{bx}^{2n+l_{bx}+1}. \tag{C.12}$$

For the case $l_{bx} = 0$ (common for light ions) one has

$$\begin{aligned} I_{00}(\mathcal{O}) &= (4\pi)^{1/2} \sum_n \frac{d_{n0}}{(2n+1)!} \mathcal{O}^{2n} \\ &= (4\pi)^{1/2} d_{00} + (4\pi)^{1/2} \frac{1}{6} d_{10} \mathcal{O}^2 + \cdots \\ &= D_0 [1 + \frac{1}{6} \rho^2 \mathcal{O}^2 + \cdots] \\ &\approx D_0 \Lambda(r_x), \end{aligned} \tag{C.13}$$

where

$$D_0 = (4\pi)^{1/2} d_{00} \qquad \rho^2 = \frac{d_{10}}{d_{00}}. \tag{C.14}$$

Let us introduce the operator ∇_x which operates only on $\chi_x^{(-)*}(\vec{r}_x)$. By means of the Green's theorem:

$$\oint_S (\varphi \nabla \psi - \psi \nabla \varphi) \mathrm{d}S = \int_V (\varphi \nabla^2 \psi - \psi \nabla^2 \varphi) \mathrm{d}V. \tag{C.15}$$

Then

$$\begin{aligned} &\int \mathrm{d}\vec{r}_x \nabla_x^2 \chi_b^{(-)*}(\vec{r}_x) \chi_x^{(-)*}(\vec{r}_x) \chi_a^{(+)}(\vec{r}_x) = \int \mathrm{d}\vec{r}_x \chi_x^{(-)*}(\vec{r}_x) \nabla^2 \{\chi_b^{(-)*}(\vec{r}_x) \chi_a^{(+)}(\vec{r}_x)\} \\ &= \int \mathrm{d}\vec{r}_x (\nabla_a^2 + 2\nabla_a \nabla_b + \nabla_b^2) \chi_b^{(-)*}(\vec{r}_x) \chi_x^{(-)*}(\vec{r}_x) \chi_a^{(+)}(\vec{r}_x), \end{aligned} \tag{C.16}$$

so

$$\nabla_x^2 = \nabla_a^2 + 2\nabla_a \nabla_b + \nabla_b^2. \tag{C.17}$$

Then

$$\mathcal{O}^2 = (\frac{1}{q^2} - \frac{p}{q}) \nabla_b^2 + (p^2 - \frac{p}{q}) \nabla_a^2 + \frac{p}{q} \nabla_x^2. \tag{C.18}$$

Since $\mathcal{O}^2$ involves only ∇^2 operators, we may replace these by using the Schrodinger equations obeyed by the corresponding functions on which they act:

$$\nabla_a^2 \chi_a^{(+)}(\vec{k_a}, \vec{r}_x) = \frac{2\mu_a}{\hbar^2} (U_a - E_a) \chi_a^{(+)}(\vec{k_a}, \vec{r}_x), \tag{C.19}$$

$$\nabla_b^2 \chi_b^{(-)*}(\vec{k_b}, \vec{r}_x) = \frac{2\mu_b}{\hbar^2} (U_b - E_b) \chi_b^{(-)*}(\vec{k_b}, \vec{r}_x), \tag{C.20}$$

$$\nabla_x^2 \chi_x^{(-)*}(\vec{k_x}, \vec{r}_x) = \frac{2\mu_x}{\hbar^2} (U_x - E_x) \chi_x^{(-)*}(\vec{k_x}, \vec{r}_x). \tag{C.21}$$

Then

$$\mathcal{O}^2 = (\frac{1}{q^2} - \frac{p}{q})\frac{2\mu_b}{\hbar^2}(U_b - E_b) + (p^2 - \frac{p}{q})\frac{2\mu_a}{\hbar^2}(U_a - E_a) + \frac{p}{q}\frac{2\mu_x}{\hbar^2}(U_x - E_x). \tag{C.22}$$

Finally, we get

$$\Lambda(r_x) = 1 + \frac{d_{10}}{d_{00}}\left\{(\frac{1}{q^2} - \frac{p}{q})\frac{2\mu_b}{\hbar^2}(U_b - E_b) + (p^2 - \frac{p}{q})\frac{2\mu_a}{\hbar^2}(U_a - E_a) + \frac{p}{q}\frac{2\mu_x}{\hbar^2}(U_x - E_x)\right\}. \tag{C.23}$$

References

[1] Aguilera, E. F., Martinez-Quiroz, E., Lizcano, D., Gómez-Camacho, A., Kolata, J. J., Lamm, L. O., Guimarães, V., Lichtenthäler, R., Camargo, O., Becchetti, F. D., Jiang, H., DeYoung, P. A., Mears, P. J., & Belyaeva, T. L. (2009). Reaction cross sections for ^{8}B, ^{7}Be, and ^{6}Li $+^{58}$ Ni near the Coulomb barrier: Proton-halo effects. *Phys. Rev. C*, 79, 021601.

[2] An, H. & Cai, C. (2006). Global deuteron optical model potential for the energy range up to 183 MeV. *Phys. Rev. C*, 73, 054605.

[3] Ascuitto, R. J. & Glendenning, N. K. (1969). Inelastic processes in particle transfer reactions. *Phys. Rev.*, 181, 1396–1403.

[4] Austern, N., Iseri, Y., Kamimura, M., Kawai, M., Rawitscher, G., & Yahiro, M. (1987). Continuum-discretized coupled-channels calculations for three-body models of deuteron-nucleus reactions. *Phys. Rep.*, 154, 125.

[5] Austern, N. & Vincent, C. M. (1981). Inclusive breakup reactions. *Phys. Rev. C*, 23, 1847.

[6] Barnett, A. R. & Lilley, J. S. (1974). Interaction of alpha particles in the lead region near the Coulomb barrier. *Phys. Rev. C*, 9, 2010.

[7] Baur, G., Pauli, M., Rösel, F., & Trautmann, D. (1979). The break-up mechanism for heavy ion reactions in the case of (^{9}Be, ^{8}Be). *Nucl. Phys. A*, 315, 241.

[8] Baur, G., Rösel, F., & Trautmann, D. (1976). Investigations of the deuteron break-up on heavy nuclei above the Coulomb barrier. *Nucl. Phys. A*, 265, 101.

[9] Baur, G., Shyam, R., Rosel, F., & Trautmann, D. (1980). Importance of the breakup mechanism for composite particle scattering. *Phys. Rev. C*, 21, 2668.

[10] Baur, G., Shyam, R., Rösel, F., & Trautmann, D. (1983). Calculation of proton-neutron coincidence cross sections in 56 MeV deuteron-induced breakup reactions by post form distorted-wave Born approximation. *Phys. Rev. C*, 28, 946.

[11] Beck, C., Keeley, N., & Diaz-Torres, A. (2007). Coupled-channel effects in elastic scattering and near-barrier fusion induced by weakly bound nuclei and exotic halo nuclei. *Phys. Rev. C*, 75, 054605.

[12] Bohr, N. (1936). Neutron capture and nuclear constitution. *Nature*, 137, 344.

[13] Boselli, M. & Diaz-Torres, A. (2014). Unambiguous separation of low-energy fusion processes of weakly bound nuclei. *J. Phys. G: Nuclear and Particle Physics*, 41, 094001.

[14] Boselli, M. & Diaz-Torres, A. (2015). Quantifying low-energy fusion dynamics of weakly bound nuclei from a time-dependent quantum perspective. *Phys. Rev. C*, 92, 044610.

[15] Britt, H. C. & Cramer, J. D. (1970). Fission of odd-α uranium and plutonium isotopes excited by (d,p), (t,d), and (t,p) reactions. *Phys. Rev. C*, 2, 1758.

[16] Buck, B. & Merchant, A. C. (1988). Cluster model of A=7 nuclei revisited, and the astrophysical S factors for ^{3}He(α,γ) ^{7}Be and ^{3}H$(\alpha,\gamma)^7$Li at zero energy. *J. Phys. G: Nuclear and Particle Physics*, 14, L211.

[17] Budzanowski, A., Baur, G., Alderliesten, C., Bojowald, J., Mayer-Boricke, C., Oelert, W., Turek, P., Rosel, F., & Trautmann, D. (1978). Observation of the α-Particle Breakup Process at $E_\alpha^{\rm lab}$ = 172.5 MeV. *Phys. Rev. Lett.*, 41, 635.

[18] Buttle, P. & Goldfarb, L. B. (1964). Finite range effects in deuteron stripping processes. *Proceedings of the Physical Society*, 83, 701.

[19] C. Signorini, C. et al. (2003). Exclusive breakup of ^{6}Li by ^{208}Pb at Coulomb barrier energies. *Phys. Rev. C*, 67, 044607.

[20] Camacho, J. G. & Moro, A. M. (2014). A pedestrian approach to the theory of transfer reactions: Application to weakly-bound and unbound exotic nuclei. In *The Euroschool on Exotic Beams, Vol. IV* (pp. 39–66). Springer.

[21] Canto, L., Gomes, P., Donangelo, R., & Hussein, M. (2006). Fusion and breakup of weakly bound nuclei. *Phys. Rep.*, 424, 1.

[22] Canto, L., Gomes, P., Donangelo, R., Lubian, J., & Hussein, M. (2015a). Recent developments in fusion and direct reactions with weakly bound nuclei. *Phys. Rep.*, 596, 1. Recent developments in fusion and direct reactions with weakly bound nuclei.

[23] Canto, L. F., Donangelo, R., de Matos, L. M., Hussein, M. S., & Lotti, P. (1998). Complete and incomplete fusion in heavy ion collisions. *Phys. Rev. C*, 58, 1107.

[24] Canto, L. F., Junior, D. R. M., Gomes, P. R. S., & Lubian, J. (2015b). Reduction of fusion and reaction cross sections at near-barrier energies. *Phys. Rev. C*, 92, 014626.

[25] Capel, P., Goldstein, G., & Baye, D. (2004). Time-dependent analysis of the breakup of ^{11}Be on ^{12}C at 67 MeV/nucleon . *Phys. Rev. C*, 70, 064605.

[26] Capote, R. (2016). *private communication*.

[27] Carlson, B. V., Capote, R., & Sin, M. (2016). Inclusive proton emission spectra from deuteron breakup reactions. *Few-Body Systems*, 57, 307–314.

[28] Castaneda, C. M., Smith, H. A., Singh, P. P., & Karwowski, H. (1980). Mechanisms of production of fast particles with $Z = 1, 2$ in ^{6}Li-induced reactions far above the Coulomb barrier. *Phys. Rev. C*, 21, 179.

[29] Cook, J. (1982). Global optical-model potentials for the elastic scattering of 6, 7Li projectiles. *Nucl. Phys. A*, 388, 153.

[30] Cotanch, S. R. (2010). Coupled channels optical theorem and non-elastic cross section sum rule. *Nucl. Phys. A*, 842, 48.

[31] Dasgupta, M. et al. (2002). Fusion and breakup in the reactions of ^{6}Li and ^{7}Li nuclei with ^{209}Bi. *Phys. Rev. C*, 66, 041602.

[32] Dasgupta, M. et al. (2004). Effect of breakup on the fusion of ^{6}Li, ^{7}Li, and ^{9}Be with heavy nuclei. *Phys. Rev. C*, 70, 024606.

[33] de Diego, R., Arias, J. M., Lay, J. A., & Moro, A. M. (2014). Continuum-discretized coupled-channels calculations with core excitation. *Phys. Rev. C*, 89, 064609.

[34] de Faria, P. N., Lichtenthäler, R., Pires, K. C. C., Moro, A. M., Lépine-Szily, A., Guimarães, V., Mendes, D. R., Arazi, A., Barioni, A., Morcelle, V., & Morais, M. C. (2010). α-particle production in ^{6}He+^{120}Sn collisions. *Phys. Rev. C*, 82, 034602.

[35] Di Pietro, A. et al. (2012). Experimental study of the collision ^{11}Be + ^{64}Zn around the Coulomb barrier. *Phys.Rev. C*, 85, 054607.

[36] Di Pietro, A., Randisi, G., Scuderi, V., Acosta, L., Amorini, F., Borge, M. J. G., Figuera, P., Fisichella, M., Fraile, L. M., Gomez-Camacho, J., Jeppesen, H., Lattuada, M., Martel, I., Milin, M., Musumarra, A., Papa, M., Pellegriti, M. G., Perez-Bernal, F., Raabe, R., Rizzo, F., Santonocito, D., Scalia, G., Tengblad, O., Torresi, D., Vidal, A. M., Voulot, D., Wenander, F., & Zadro, M. (2010). Elastic Scattering and Reaction Mechanisms of the Halo Nucleus ^{11}Be around the Coulomb Barrier. *Phys. Rev. Lett.*, 105, 022701.

[37] Diaz-Torres, A. (2010). Modelling incomplete fusion dynamics of weakly bound nuclei at near-barrier energies. *J. Phys. G: Nuclear and Particle Physics*, 37, 075109.

[38] Diaz-Torres, A. (2011). Platypus: A code for reaction dynamics of weakly-bound nuclei at near-barrier energies within a classical dynamical model. *Comput. Phys. Commun.*, 182, 1100.

[39] Diaz-Torres, A., Hinde, D., Tostevin, J., Dasgupta, M., & Gasques, L. (2007). Relating breakup and incomplete fusion of weakly bound nuclei through a classical trajectory model with stochastic breakup. *Phys. Rev. Lett.*, 98, 152701.

[40] Diaz-Torres, A. & Thompson, I. J. (2002). Effect of continuum couplings in fusion of halo ^{11}Be on ^{208}Pb around the Coulomb barrier. *Phys. Rev. C*, 65, 024606.

[41] Diaz-Torres, A., Thompson, I. J., & Beck, C. (2003). How does breakup influence the total fusion of ^{6,7}Li at the Coulomb barrier? *Phys. Rev. C*, 68, 044607.

[42] Ducasse, Q. (2015). *Etude de la méthode de substitution à partir de la mesure simultanée des probabilités de fission et d'émission gamma des actinides ^{236}U, ^{238}U, ^{237}Np et ^{238}Np*. PhD thesis. Thèse de doctorat dirigée par Jurado, Beatriz et Sérot, Olivier Astrophysique, plasmas, nucléaire Bordeaux 2015.

[43] Ducasse, Q., Jurado, B., Aïche, M., Marini, P., Mathieu, L., Görgen, A., Guttormsen, M., Larsen, A., Tornyi, T., Wilson, J., et al. (2015). Study of the ^{238}U (d,p) surrogate reaction via the simultaneous measurement of gamma-decay and fission probabilities. *arXiv preprint arXiv:1512.06334*.

[44] Esbensen, H. & Bertsch, G. (1996). Effects of $E2$ transitions in the Coulomb dissociation of ^{8}B . *Nucl. Phys. A*, 600, 37.

[45] Esbensen, H. & Bertsch, G. F. (1996). Effects of $E2$ Transitions in the Coulomb Dissociation of ^{8}B. *Nucl. Phys. A*, 600, 37.

[46] Escher, J. E., Burke, J. T., Dietrich, F. S., Scielzo, N. D., Thompson, I. J., & Younes, W. (2012). Compound-nuclear reaction cross sections from surrogate measurements. *Rev. Mod. Phys.*, 84, 353.

[47] Escrig, D. et al. (2007). α-particle production in the scattering of ^{6}He by ^{208}Pb at energies around the Coulomb barrier. *Nucl. Phys. A*, 792, 2.

[48] Faddeev, L. D. (1960). *Zh. Eksp. Teor. Fiz.*, 39, 1459. [Sov. Phys. JETP **12**, 1014 (1961)].

[49] Feshbach, H. (1962). A unified theory of nuclear reactions. II. *Annals of Physics*, 19, 287.

[50] Fick, D., Brown, R. E., Grüebler, W., Hardekopf, R. A., & Hanspal, J. S. (1984). Elastic scattering of polarized tritons from ^{12}C, ^{15}V, and ^{58}Ni at 9 and 11 MeV. *Phys. Rev. C*, 29, 324.

[51] Figueira, J. M., Niello, J. O. F., Arazi, A., Capurro, O. A., Carnelli, P., Fimiani, L., Martí, G. V., Heimann, D. M., Negri, A. E., Pacheco, A. J., Lubian, J., Monteiro, D. S., & Gomes, P. R. S. (2010). Energy dependence of the optical potential of weakly and tightly bound nuclei as projectiles on a medium-mass target. *Phys. Rev. C*, 81, 024613.

[52] Fukuda, N. et al. (2004). Coulomb and nuclear breakup of a halo nucleus ^{11}Be. *Phys. Rev. C*, 70, 054606.

[53] Glöckle, W. (1983). *The Quantum Mechanical Few-Body Problem*. Springer-Verlag, Berlin/Heidelberg.

[54] Goldberger, M. L. & Watson, K. M. (2004). *Collision theory*. Courier Dover Publications.

[55] Hagino, K., Dasgupta, M., & Hinde, D. (2004). Fusion and breakup in the reactions of ^{6,7}Li and ^{9}Be. *Nucl. Phys. A*, 738, 475.

[56] Hagino, K., Vitturi, A., Dasso, C. H., & Lenzi, S. M. (2000). Role of breakup processes in fusion enhancement of drip-line nuclei at energies below the Coulomb barrier. *Phys. Rev. C*, 61, 037602.

[57] Han, Y., Shi, Y., & Shen, Q. (2006). Deuteron global optical model potential for energies up to 200 MeV. *Phys. Rev. C*, 74, 044615.

[58] Han, Y., Xu, Y., Liang, H., Guo, H., & Shen, Q. (2010). Global phenomenological optical model potential for nucleon-actinide reactions at energies up to 300 MeV. *Phys. Rev. C*, 81, 024616.

[59] Hansen, P. G. & Tostevin, J. A. (2003). Direct reactions with exotic nuclei. *Ann. Rev. Nucl. Part. Sci.*, 53, 219.

[60] Hashimoto, S., Ogata, K., Chiba, S., & Yahiro, M. (2009). New approach for evaluating incomplete and complete fusion cross sections with continuum-discretized coupled-channels method. *Prog. Theor. Phys.*, 122, 1291.

[61] Hassan, A. A., Luk'yanov, S. M., & Kalpakchieva, R. (2004). Technical report, Joint Institute for Nuclear Research (JINR).

[62] Herman, M., Capote, R., Carlson, B., Obložinský, P., Sin, M., Trkov, A., Wienke, H., & Zerkin, V. (2007). Empire: Nuclear reaction model code system for data evaluation. *Nuclear Data Sheets*, 108, 2655. Special Issue on Evaluations of Neutron Cross Sections.

[63] Hirabayashi, Y. & Sakuragi, Y. (1991). Anomalous renormalization of cluster-folding interactions for 6 li-nucleus scattering at low energies. *Phys. Lett. B*, 258, 11–16.

[64] Huby, R. & Mines, J. R. (1965). Distorted-wave born approximation for stripping to virtual levels. *Rev. Mod. Phys.*, 37, 406.

[65] Huizenga, J. R. & Igo, G. (1962). Theoretical reaction cross sections for alpha particles with an optical model. *Nucl. Phys.*, 29, 462.

[66] Hussein, M., Frederico, T., & Mastroleo, R. (1990). Faddeev and DWBA description of inclusive break-up and incomplete fusion reactions. *Nuc. Phys. A*, 511, 269.

[67] Hussein, M. & McVoy, K. (1985). Inclusive projectile fragmentation in the spectator model. *Nucl. Phys. A*, 445, 124 – 139.

[68] Hussein, M. S., Carlson, B. V., Frederico, T., & Tarutina, T. (2004). Three-body model for the complete fusion of a two-cluster composite projectile with a heavy target. *Nucl. Phys. A*, 738, 367.

[69] Hussein, M. S. & Mastroleo, R. C. (1989). Glauber calculation of heavy-ion and light-ion inclusive break-up cross sections. *Nucl. Phys. A*, 491, 468.

[70] Ichimura, M. (1990). Relation among theories of inclusive breakup reactions. *Phys. Rev. C*, 41, 834.

[71] Ichimura, M., Austern, N., & Vincent, C. M. (1985). Equivalence of post and prior sum rules for inclusive breakup reactions. *Phys. Rev. C*, 32, 431.

[72] Ichimura, M., Austern, N., & Vincent, C. M. (1986). Comparison of approximate formalisms for inclusive breakup reactions. *Phys. Rev. C*, 34, 2326.

[73] Ichimura, M., Austern, N., & Vincent, C. M. (1988). Approximate sum rules for inclusive breakup reactions. *Phys. Rev. C*, 37, 2264.

[74] Iwamoto, O., Nohtomi, A., Uozumi, Y., Sakae, T., Matoba, M., Nakano, M., Maki, T., & Koori, N. (1994). Single-particle states in ^{59}Ni with $^{58}(d,p)^{59}$Ni reaction at 56 MeV and neutron-bound-state complex potentials. *Nucl. Phys. A*, 576, 387.

[75] Jia, W., Tao, Y., Wei-Li, S., Watanabe, Y., & Ogata, K. (2011). Inclusive proton energy spectra of the deuteron induced reaction. *Chin. Phys. Lett.*, 28, 112401.

[76] Johnson, R. & Tandy, P. (1974). An approximate three-body theory of deuteron stripping. *Nucl. Phys. A*, 235, 56.

[77] Johnson, R. C. & Soper, P. J. R. (1970). Contribution of deuteron breakup channels to deuteron stripping and elastic scattering. *Phys. Rev. C*, 1, 976.

[78] Jr., F. B. & G.W.Greenlees (1969). *Ann. Rept. J.H.Williams Lab., Univ. Minnesota*.

[79] Kasano, A. & Ichimura, M. (1982). A new formalism of inclusive breakup reactions and validity of the surface approximation. *Phys. Lett. B*, 115, 81.

[80] Kawai, M., Kerman, A. K., & McVoy, K. W. (1973). Modification of Hauser-Feshbach calculations by direct-reaction channel coupling. *Annals of Physics*, 75, 156.

[81] Keeley, N., Bennett, S., Clarke, N., Fulton, B., Tungate, G., Drumm, P., Nagarajan, M., & Lilley, J. (1994). Optical model analyses of ^{6,7}Li + ^{208}Pb elastic scattering near the Coulomb barrier. *Nucl. Phys. A*, 571, 326.

[82] Keeley, N., Kemper, K., & Rusek, K. (2001). Fusion calculations for the ^{6,7}Li+^{16}O systems. *Phys. Rev. C*, 65, 014601.

[83] Kelly, G. R., Davis, N. J., Ward, R. P., Fulton, B. R., Tungate, G., Keeley, N., Rusek, K., Bartosz, E. E., Cathers, P. D., Caussyn, D. D., Drummer, T. L., & Kemper, K. W. (2000). α breakup of ^{6}Li and ^{7}Li near the coulomb barrier. *Phys. Rev. C*, 63, 024601.

[84] Kerman, A. K. & McVoy, K. W. (1979). Fluctuations in two-step reactions through doorways. *Annals of Physics*, 122, 197.

[85] Kido, T., Yabana, K., & Suzuki, Y. (1994). Coulomb breakup mechanism of neutron drip-line nuclei. *Phys. Rev. C*, 50, R1276(R).

[86] Kleinfeller, J., Bisplinghoff, J., Ernst, J., Mayer-Kuckuk, T., Baur, G., Hoffmann, B., Shyam, R., Rosel, F., & Trautmann, D. (1981). Study of inclusive proton spectra from low energy deuteron reactions in terms of spectator break-up and coulomb dissociation of the projectile. *Nucl. Phys. A*, 370, 205.

[87] Kolata, J. J., Guimarães, V., Peterson, D., Santi, P., White-Stevens, R. H., Vincent, S. M., Becchetti, F. D., Lee, M. Y., O'Donnell, T. W., Roberts, D. A., & Zimmerman, J. A. (2001). Breakup of ^{8}B at sub-Coulomb energies. *Phys. Rev. C*, 63, 024616.

[88] Koning, A. & Delaroche, J. (2003). Local and global nucleon optical models from 1 KeV to 200 MeV . *Nucl. Phys. A*, 713, 231.

[89] Kumawat, H., Jha, V., Parkar, V. V., Roy, B. J., Santra, S., Kumar, V., Dutta, D., Shukla, P., Pant, L. M., Mohanty, A. K., Choudhury, R. K., & Kailas, S. (2010). Inclusive α-production cross section for the ^{6}Li +^{90} Zr system at energies near the fusion barrier. *Phys. Rev. C*, 81, 054601.

[90] Lee, L. L. & Schiffer, J. P. (1964). Studies of Elastic Scattering of Protons, Deuterons, and Alpha Particles from Isotopes of Cu, Ni, and Fe. *Phys. Rev.*, 134, B765.

[91] Lei, J. & Moro, A. M. (2015a). Numerical assessment of post-prior equivalence for inclusive breakup reactions. *Phys. Rev. C*, 92, 061602(R).

[92] Lei, J. & Moro, A. M. (2015b). Reexamining closed-form formulae for inclusive breakup: Application to deuteron- and ^{6}Li-induced reactions. *Phys. Rev. C*, 92, 044616.

[93] Li, X.-H., Udagawa, T., & Tamura, T. (1984). Assessment of approximations made in breakup-fusion descriptions. *Phys. Rev. C*, 30, 1895.

[94] Liu, Z. H., Signorini, C., Mazzocco, M., Ruan, M., Zhang, H. Q., Glodariu, T., Wu, Y. W., Soramel, F., Lin, C. J., & Yang, F. (2005). Partial fusion of a weakly bound projectile with heavy target at energies above the Coulomb barrier. *Eur. Phys. J. A*, 26, 73.

[95] Mahaux, C., Bortignon, P., Broglia, R., & Dasso, C. (1985). Dynamics of the shell model. *Physics Reports*, 120, 1 – 274.

[96] Marta, H. D., Canto, L. F., & Donangelo, R. (2014). Complete and incomplete fusion of weakly bound nuclei. *Phys. Rev. C*, 89, 034625.

[97] Mastroleo, R. C., Udagawa, T., & Tamura, T. (1989). Exact finite range evaluation of breakup-fusion cross section in the post form. *J. Phys. G: Nuclear and Particle Physics*, 15, 473.

[98] Mazzocco, M. (2016). *private communication*.

[99] Mazzocco, M., Torresi, D., Pierroutsakou, D., Keeley, N., Acosta, L., Boiano, A., Boiano, C., Glodariu, T., Guglielmetti, A., La Commara, M., Lay, J. A., Martel, I., Mazzocchi, C., Molini, P., Parascandolo, C., Pakou, A., Parkar, V. V., Romoli, M., Rusek, K., Sánchez-Benítez, A. M., Sandoli, M., Sgouros, O., Signorini, C., Silvestri, R., Soramel, F., Soukeras, V., Stiliaris, E., Strano, E., Stroe, L., & Zerva, K. (2015). Direct and compound-nucleus reaction mechanisms in the ^{7}Be + ^{58}Ni system at near-barrier energies. *Phys. Rev. C*, 92, 024615.

[100] Moro, A. M., Crespo, R., Garcia-Martinez, H., Aguilera, E. F., Martinez-Quiroz, E., Gomez-Camacho, J., & Nunes, F. M. (2003). Reaction mechanisms in the scattering of ^{8}Li on ^{208}Pb around the Coulomb barrier. *Phys. Rev. C*, 68, 034614.

[101] Moroz, Z., Zupranski, P., Böttger, R., Egelhof, P., Möbius, K.-H., Tungate, G., Steffens, E., Dreves, W., Koenig, I., & Fick, D. (1982). The interaction of aligned ^{7}Li with ^{58}Ni. *Nucl. Phys. A*, 381, 294.

[102] Moshinsky, M. (1959). Transformation brackets for harmonic oscillator functions. *Nucl. Phys.*, 13, 104.

[103] Nakamura, T. et al. (2009). Halo structure of the island of inversion nucleus ^{31}Ne. *Phys. Rev. Lett.*, 103, 262501.

[104] Nakamura, T. & Kondo, Y. (2012). Clusters in nuclei. In C. Beck (Ed.), *Lecture Notes in Physics 848 Vol 2.* (pp.õ7). Springer Berlin.

[105] Nakayama, S., Araki, S., Watanabe, Y., Iwamoto, O., Ye, T., & Ogata, K. (2014). Cross Section Calculations of Deuteron-induced Reactions Using the Extended CCONE Code. *Nuclear Data Sheets*, 118, 305.

[106] Nishioka, H., Tostevin, J., Johnson, R., & Kubo, K.-I. (1984). Projectile excitation and structure effects in ^{6}Li and ^{7}Li scattering. *Nucl. Phys. A*, 415, 230.

[107] Pakou, A., Alamanos, N., Gillibert, A., Kokkoris, M., Kossionides, S., Lagoyannis, A., Nicolis, N. G., Papachristodoulou, C., Patiris, D., Pierroutsakou, D., Pollacco, E. C., & Rusek, K. (2003). α-Particle Production in the Reaction^{6}Li + ^{28}Si at Near-Barrier Energies. *Phys. Rev. Lett.*, 90, 202701.

[108] Pampus, J., Bisplinghoff, J., Ernst, J., Mayer-Kuckuk, T., Rama Rao, J., Baur, G., Rosel, F., & Trautmann, D. (1978). Inclusive proton spectra from deuteron break-up: Theory and experiment. *Nucl. Phys. A*, 311, 141.

[109] Pesudo Fortes, V. (2015). *Analysis of the reaction of a one-neutron halo nucleus on a heavy target at energies around the Coulomb barrier: The case of ^{11}Be on ^{197}Au*. PhD thesis, Universidad Complutense de Madrid.

[110] Pfeiffer, K., Speth, E., & Bethge, K. (1973). Break-up of ^{6}Li and ^{7}Li on tin and nickel nuclei. *Nucl. Phys. A*, 206, 545.

[111] Pietro, D. (2016). *private communication*.

[112] Potel, G., Nunes, F. M., & Thompson, I. J. (2015). Establishing a theory for deuteron-induced surrogate reactions. *Phys. Rev. C*, 92, 034611.

[113] Pradhan, M. K., Mukherjee, A., Roy, S., Basu, P., Goswami, A., Kshetri, R., Palit, R., Parkar, V. V., Ray, M., Saha Sarkar, M., & Santra, S. (2013). Importance of the 1n-stripping process in the ^{6}Li + ^{159}Tb reaction. *Phys. Rev. C*, 88, 064603.

[114] Ramler, W. J., Wing, J., Henderson, D. J., & Huizenga, J. R. (1959). Excitation functions of bismuth and lead. *Phys. Rev.*, 114, 154.

[115] Ridikas, D., Mittig, W., Savajols, H., Roussel-Chomaz, P., Förtsch, S. V., Lawrie, J. J., & Steyn, G. F. (2000). Inclusive proton production cross sections in (d, xp) reactions induced by 100 MeV deuterons. *Phys. Rev. C*, 63, 014610.

[116] Santra, S. et al. (2009). Resonant breakup of ^{6}Li by ^{209}Bi. *Phys.Lett. B*, 677, 139.

[117] Santra, S., Kailas, S., Parkar, V. V., Ramachandran, K., Jha, V., Chatterjee, A., Rath, P. K., & Parihari, A. (2012). Disentangling reaction mechanisms for α production in the ^{6}li + ^{209}bi reaction. *Phys. Rev. C*, 85, 014612.

[118] Santra, S., Kailas, S., Ramachandran, K., Parkar, V. V., Jha, V., Roy, B. J., & Shukla, P. (2011). Reaction mechanisms involving weakly bound ^{6}Li and ^{209}Bi at energies near the Coulomb barrier. *Phys. Rev. C*, 83, 034616.

[119] Satchler, G. (1983). *Direct nuclear reactions*. International series of monographs on physics. Clarendon Press.

[120] Shibata, K. et al. (2011). JENDL-4.0: A New Library for Nuclear Science and Engineering. *Journal of Nuclear Science and Technology*, 48, 1–30.

[121] Shyam, R., Baur, G., Rosel, F., & Trautmann, D. (1980). Elastic and Inelastic Breakup of the ^{3}He Particle. *Phys. Rev. C*, 22, 1401.

[122] Signorini, C., Mazzocco, M., Prete, G. F., Soramel, F., Stroe, L., Andrighetto, A., Thompson, I. J., Vitturi, A., Brondi, A., Cinausero, M., Fabris, D., Fioretto, E., Gelli, N., Guo, J. Y., La Rana, G., Liu, Z. H., Lucarelli, F., Moro, R., Nebbia, G., Trotta, M., Vardaci, E., & Viesti, G. (2001). Strong reaction channels at barrier energies in the system ^{6}Li + ^{208}Pb. *Eur. Phys. J. A*, 10, 249.

[123] Sokhotskli, Y. V. (1873). *On definite integrals and functions employed in expansions into series*. Ob opredelennykh i funtsiakh uprotrebljayemykh pri razlozhenii v ryady), St Petersburg.

[124] Souza, F. et al. (2009). Reaction mechanisms in the ^{6}Li+^{59}Co system . *Nucl. Phys. A*, 821, 36.

[125] Souza, F. A., Leal, L. A. S., Carlin, N., Munhoz, M. G., Neto, R. L., Moura, M. M. d., Suaide, A. A. P., Szanto, E. M., Toledo, A. S. d., & Takahashi, J. (2007). Effect of breakup on elastic scattering for the ^{6,7}Li +^{59} Co systems. *Phys. Rev. C*, 75, 044601.

[126] Summers, N. C., Nunes, F. M., & Thompson, I. J. (2006). Extended continuum discretized coupled channels method: Core excitation in the breakup of exotic nuclei. *Phys. Rev. C*, 74, 014606.

[127] Thompson, I. & Diaz-Torres, A. (2004). Modelling effects of halo breakup on fusion. *Progress of Theoretical Physics Supplement*, 154, 69–76.

[128] Thompson, I. J. (1988). Coupled reaction channels calculations in nuclear physics. *Comp. Phys. Rep.*, 7, 167 – 212.

[129] Thompson, I. J. & Nunes, F. M. (2009). Nuclear reactions for astrophysics. *Nuclear Reactions for Astrophysics, Cambridge, UK: Cambridge University Press, 2009*, 1.

[130] Tostevin, J. A. (2001). Single-nucleon knockout reactions at fragmentation beam energies. *Nucl. Phys. A*, 682, 320.

[131] Tostevin, J. A., Nunes, F. M., & Thompson, I. J. (2001). Calculations of three-body observables in ^{8}B breakup. *Phys. Rev. C*, 63, 024617.

[132] Typel, S. & Baur, G. (1994). Coulomb Dissociation of ^{8}B into ^{7}Be + p: Effects of multiphoton exchange. *Phys. Rev. C*, 50, 2104.

[133] Udagawa, T., Lee, Y. J., & Tamura, T. (1987). Extension of the breakup-fusion description to stripping reactions to negative energy states. *Phys.Lett. B*, 196, 291.

[134] Udagawa, T., Lee, Y. J., & Tamura, T. (1989). Breakup-fusion analyses of single-nucleon stripping to bound and unbound orbits. *Phys. Rev. C*, 39, 47.

[135] Udagawa, T., Li, X. H., & Tamura, T. (1984). Breakup-fusion description of nonequilibrium protons from (α, p) reactions. *Phys. Lett. B*, 135, 333.

[136] Udagawa, T. & Tamura, T. (1980). Breakup-fusion description of massive transfer reactions with emission of fast light particles. *Phys. Rev. Lett.*, 45, 1311.

[137] Udagawa, T. & Tamura, T. (1981). Derivation of breakup-fusion cross sections from the optical theorem. *Phys. Rev. C*, 24, 1348.

[138] Udagawa, T., Tamura, T., & Mastroleo, R. C. (1988). Exact and approximate sum rules for inclusive breakup reactions. *Phys. Rev. C*, 37, 2261.

[139] Vincent, C. M. (1968). Gell-mann-goldberger relation for reactions of the form (d, pn). *Phys. Rev.*, 175, 1309.

[140] Vincent, C. M. & Fortune, H. T. (1970). New method for distorted-wave analysis of stripping to unbound states. *Phys. Rev. C*, 2, 782.

[141] Watanabe, S., Matsumoto, T., Minomo, K., Ogata, K., & Yahiro, M. (2012). Effects of four-body breakup on ^{6}li elastic scattering near the coulomb barrier. *Phys. Rev. C*, 86, 031601.

[142] Wu, J. R., Chang, C. C., & Holmgren, H. D. (1979). Charged-particle spectra: 80 MeV deuterons on ^{27}Al and ^{58}Ni and 70 MeV deuterons on ^{90}Zr, ^{208}Pb, and ^{232}Th. *Phys. Rev. C*, 19, 370.

[143] Yahiro, M., Iseri, Y., Kameyama, H., Kamimura, M., & Kawai, M. (1986). Chapter III. Effects of Deuteron Virtual Breakup on Deuteron Elastic and Inelastic Scattering. *Prog. Theor. Phys. Suppl.*, 89, 32.

[144] Ye, T., Hashimoto, S., Watanabe, Y., Ogata, K., & Yahiro, M. (2011). Analysis of inclusive (d,xp) reactions on nuclei from ^{9}Be to ^{238}U at 100 MeV. *Phys. Rev. C*, 84, 054606.